UNIVERSITY OF CALIFORNIA

Los Angeles

STELLAR BINARIES AT THE GALACTIC CENTER

A dissertation submitted in partial satisfaction

of the requirements for the degree

Doctor of Philosophy in Astronomy and Astrophysics

by

Devin Satoru Chu

2020

ABSTRACT OF THE DISSERTATION

STELLAR BINARIES AT THE GALACTIC CENTER

by

Devin Satoru Chu
Doctor of Philosophy in Astronomy and Astrophysics
University of California, Los Angeles, 2020
Professor Andrea Ghez, Chair

This thesis performs unprecedented investigations for spectroscopic binaries at the Galactic center and utilizes the development and extended observing baseline of integral field spectroscopy behind adaptive optics. The second chapter of this thesis describes the first direct search for binarity of its kind for the star S0-2, the most well-studied star of the S-star cluster. Almost two decades of spectroscopic with adaptive optics has led to the capability to look for a binary signal in S0-2's spectroscopic data. We introduce a methodology for investigating periodicity and placing limits on binary parameters with radial velocity data. We do not detect any signs of binarity for S0-2 and place limits on a hypothetical companion mass for S0-2 to be 1.6 $M_{\odot}$, which is below current detection limits. We also investigate and find that a feasible spectroscopic binary system would not bias the detection of relativistic redshift, a post-Newtonian spectroscopic measurement.

The third chapter of this thesis explains the improvements in spectral analysis that lead to greater sensitivity to spectroscopic binary systems. We use a new method for measuring radial velocity measurements of stars at the Galactic center. This new method utilizes spectral fitting software and a new infrared spectral grid that finally covers effective temperatures of 30,000 K, putting the young, massive S-stars at the Galactic center within reach. We improve the precision of our radial velocities by a

factor of 1.7. We also test our methodology on radial velocity standard stars and find that the new method eliminates the slight bias of our previous method. These characteristics of this method make us more sensitive to detecting the radial velocity variations of spectroscopic binary stars.

The fourth chapter presents a systematic search for spectroscopic binaries at the Galactic Center. With over two decades of integral field spectroscopy data, advanced tools for fitting mid-infrared stellar spectra, and 1000 radial velocity data points, we conduct a spectroscopic binary search of 29 stars at the Galactic center. After subtracting a star's motion around the supermassive black hole, we search for a periodic signal using a Lomb-Scargle analysis and fitting the residual radial velocity curve to a binary system radial velocity curve. We find no significant periodic detections in our sample, suggesting there are no binaries among the S-stars. We also place limits on the hypothetical companion masses of these S-stars. We also place a limit on the intrinsic binary fraction of these stars at 42%, which disagrees with the binary fraction for massive field stars. These results favor S-star formation mechanisms that result in a low binary fraction.

The final chapter presents new integral field spectroscopic observations of stars in the nuclear star cluster. We present data taken over 6 years and add the spectral types of 169 stars: 47 of which are Wolf-Rayet and O/B stars, and the remaining 122 are K and M giants. This addition to the rich Galactic center integral field spectroscopy data set provides opportunities to further study stellar demographics and dynamics of the nuclear star cluster.

The dissertation of Devin Satoru Chu is approved.

Tuan Do

James Larkin

Smadar Naoz

Mark Morris

Andrea Ghez, Committee Chair

University of California, Los Angeles

2020

To my family

TABLE OF CONTENTS

LIST OF FIGURES

LIST OF TABLES

ACKNOWLEDGMENTS

I am so grateful for the support I have received throughout my time at UCLA. Without these people, I would not be in position to complete this thesis. I would like to thank my advisors Andrea Ghez and Tuan Do for molding me into a better scientist. I am so grateful to the scientific and support staff at the W.M. Keck Observatory, for helping me take the data that goes into my thesis and for the long observing nights. I want to thank the staff at ISEE, especially Lisa Hunter, for helping me think about equity and inclusion in my academic pursuits. I am grateful for my classmates Michael Topping and Abhimat Gautam, and fellow UCLA astronomy and astrophysics graduate students, for supporting me throughout my years at grad school. Finally, I am eternally grateful for my family for being my foundation and support. I am especially thankful for my loving fiancée, for lifting me up when I really needed help.

I acknowledge that results presented in this thesis are based on published works with additional coauthors. Support for this work at UCLA was provided by NSF award number 1909554. I wish to recognize that the summit of Maunakea has always held a very significant cultural role for the indigenous Hawaiian community. I am most fortunate to have the opportunity to observe from this mountain.

Chapter 2 of this dissertation is a version of Chu et al. (2018) and is reproduced by permission of the AAS. We are grateful for the helpful and constructive comments from the referee. We thank M.R. Morris and E.E. Becklin for their comments and long-term efforts on the Galactic Center Orbits Initiative. We also thank the staff of the Keck Observatory, especially Jim Lyke, Randy Campbell, Gary Puniwai, Heather Hershey, Hien Tran, Scott Dahm, Jason McIlroy, Joel Hicock, and Terry Stickel, for all their help in obtaining the new observations. Support for this work at UCLA was provided by NSF grant AST-1412615, the W. M. Keck Foundation for support of the NStarsOrbits Project, the Levine- Leichtman Family Foundation, Ken and Eileen Kaplan Student Support Fund, the Preston Family Graduate Fellowship (held by D.C. and A.G.), the

Galactic Center Board of Advisors, and the Janet Marott Student Travel Awards. The W. M. Keck Observatory is operated as a scientific partnership among the California Institute of Technology, the University of California, and the National Aeronautics and Space Administration. The authors wish to recognize that the summit of Maunakea has always held a very significant cultural role for the indigenous Hawaiian community. We are most fortunate to have the opportunity to observe from this mountain. The Observatory was made possible by the generous financial support of the W. M. Keck Foundation.

Chapter 3 of dissertation is work that contributed to the article Do et al. (2019). Reprinted with permission from AAAS. We thank the staff and astronomers at Keck Observatory and Gemini Observatory, especially Gary Puniwai, Jason McIlroy, Sherry Yeh, John Pelletier, Joel Hicock, Greg Doppmann, Julie Renaud-Kim, Tony Ridenour, Alan Hatakeyama, Josh Walawender, Carolyn Jordan, Cynthia Wilburn, Terry Stickel, Heather Hershey, Jason Macilroy, John Pelletierm, Julie Renauld-Kim, Alessandro Rettura, Luca Rizzi, Carlos Alvarez, Marie Lemoine-Busserolle, Matthew Taylor, Trent Dupuy, Meg Schwamb, for all their help in obtaining the new data. The W.M. Keck Observatory is operated as a scientific partnership among the California Institute of Technology, the University of California, and the National Aeronautics and Space Administration. The authors wish to recognize that the summit of Maunakea has always held a very significant cultural role for the indigenous Hawaiian community. We are most fortunate to have the opportunity to observe from this mountain. We thank the Subaru telescope staff, especially Y. Minowa, T.-S. Pyo, J.-H. Kim, and E. Mieda, for their support for the Subaru observations. The Subaru Telescope is operated by the National Astronomical Observatory of Japan. Funding: Support for this work was provided by NSF AAG grant AST- 1412615, the W. M. Keck Foundation, the Heising-Simons Foundation, and the Gordon and Betty Moore Foundation. S.J. and J.R.L. acknowledge support from NSF AAG (AST-1518273). The W. M. Keck Observatory was made possible by the generous financial support of the W. M. Keck Foundation. S.N. acknowledges financial support by JSPS KAKENHI, Grant Number JP25707012,

JP15K13463, JP18K18760, and JP19H00695. H.S. was supported by JSPS KAKENHI Grant Number JP26610050 and JP19H01900. Y.T. was supported by JSPS KAKENHI Grant Number JP26800150. M.T. was supported by JSPS KAKENHI Grant Number JP17K05439, and DAIKO FOUNDATION. W.E.K. was supported by an ESO Fellowship and the Excellence Cluster Universe, Technische Universitat München. R.S. and E.G. have received funding from the European Research Council under the European Union's Seventh Framework Programme (FP7/2007-2013)/ERC grant agreement no. [614922]. R.S. acknowledges financial support from the State Agency for Research of the Spanish MCIU through the "Center of Excellence Severo Ochoa" award for the Instituto de Astrofìsica de Andalucìa (SEV-2017-0709).

VITA

2014	Graduated Dartmouth College
	Bachelor of Arts, Astronomy
	Bachelor of Arts, Physics
2015	Teaching Assistant
	Stars & Nebulae, Nature of the Universe
2016	Masters of Science, Astronomy
	University of California, Los Angeles.
2015-2019	Astronomy Live! Educational Outreach
	University of California, Los Angeles
2017-2019	Journey Through the Universe Educational Outreach
	Gemini Observatory
2018-2019	Professional Development Program
	Institute for Science and Engineering Education
2014- 2020	Graduate Student Researcher
	Department of Physics and Astronomy
	University of California, Los Angeles
2018 - 2020	PhD Candidate
	Astronomy and Astrophysics
	University of California, Los Angeles

PUBLICATIONS AND PRESENTATIONS

Chu, D. S., Do T., Hees A., Ghez A., Naoz S., Witzel G., Sakai S., Chappell S., Gautam

A. K., Lu J. R., Matthews K. “Investigating the Binarity of S0-2: Implications for its Origins and Robustness as a Probe of the Laws of Gravity around a Supermassive Black Hole”, 2018, ApJ, 854, 12

Ciurlo, A., Campbell R. N., Morris M. R., Do T., Ghez A. M., Hees A., Sitarski B., O’neil K. K., **Chu, D. S.**, Martinez G., Naoz S., Stephen A., “A population of dust-enshrouded objects orbiting the Galactic black hole”, 2020, Nature, 577, 337-–340

Do T., Hees A., Ghez A., Martinez G., **Chu, D. S.**, Jia S., Sakai S., Lu J. R., Gautam A. K., Kosmo O’niel K., Becklin E. E., Morris M. R., Matthews K., Nishiyama S., Campbell R., Chappell S., Chen Z., Ciurlo A., Dehghanfar A., Gallego-Cano E., Kerzendorf W., Lyke J., Naoz S., Saida H., Schödel R., Takahashi M., Takamori Y., Witzel G., Wizinowich P., “Relativistic redshift of the star S0-2 orbiting the Galactic center supermassive black hole”, 2019, Science, 365, 6454

American Astronomical Society 235th Meeting, Honolulu, HI, 1/2020, Constraining the binarity of the young stars around the central supermassive black hole of the Milky Way

Galactic Center Workshop, Yokohama, Japan, 10/2019, Constraining the binarity of the S-stars orbiting the central supermassive black hole using radial velocities

Keck Science Meeting, Los Angeles, CA, 9/2019, Investigating the Origin of the Stars Closest to the Supermassive Black Hole Using Binaries

American Astronomical Society 231st Meeting, Washington, DC, 1/2018, Investigating the Binarity of S0-2: Implications for its Origins and Robustness as a Probe of the Laws of Gravity around a Supermassive Black Hole

CHAPTER 1

Introduction

The center of the Milky Way provides a unique laboratory to study astrophysics in an extreme environment. Motions of stars provided some of the strongest and most convincing evidence that a supermassive black hole (SMBH) exists at the center of the galaxy, with a mass of $\sim 4 \times 10^6$ $M_\odot$ (e.g. Ghez et al. 2008; Gillessen et al. 2009a). The development of spectroscopy behind adaptive optics has revolutionized our understanding of Galactic center region. Through this technology, we have learned that a surprising population of young, massive stars exist within ~ 0.04 pc of the black hole. These stars cannot have formed via traditional star formation because of the black hole's strong tidal forces (Morris 1993). From our understanding of nearby field stars, the majority of massive stars are formed in binary systems (Sana et al. 2012; de Mink et al. 2013; Duchêne & Kraus 2013). It remains an open question whether this binary frequency also applies to young stars at the Galactic center, and if stellar binarity can help explain the existence of these young stars so close to the SMBH.

In this dissertation, I present an unprecedented search for spectroscopic binaries at the Galactic center in the immediate vicinity of the SMBH. Sensitivity to spectroscopic binaries depends heavily on the amount, precision, and temporal coverage of data. I utilize nearly two decades of spectroscopic measurements and advanced tools for analyzing spectroscopic data. With these elements, it is feasible to conduct a thorough, systematic search for spectroscopic binaries. I establish a methodology for finding them and placing limits on the binary fraction of young stars. I discuss how this work can be used to place constraints on the formation mechanism of the S-stars and on models of dynamical evolution around a SMBH.

1.0.1 Why searching for spectroscopic binaries at the Galactic center is important

Our galaxy's central SMBH and the surrounding nuclear star cluster are located ~ 8 kpc away and are the closest examples of their kind. The nuclear star cluster's proximity enables us to continuously monitor individual stars, providing an unmatched view into the dynamical environments around a SMBH. While the nuclear star cluster's close location provides great benefits, its extreme density creates a difficult challenge with resolving individual sources.

Our capabilities to study the Galactic center has progressed hand in hand with the development of telescope technology. Specifically, the development of spectroscopy behind adaptive optics has revolutionized our understanding of Galactic center. With spectroscopy, we can definitively break the degeneracy of stellar ages and separate Wolf-Rayet and main-sequence stars from evolved red giants. Through this technology, we have learned that a surprising population of young, massive stars are located within 1 arcsec (~ 0.04 pc) from the black hole, creating what Ghez et al. (2003) described as a "paradox of youth." These stars are known as the "S-stars". Additional spectroscopic studies have revealed even more young stars within a parsec of the SMBH (e.g. Paumard et al. 2006; Lu et al. 2009). The existence of these young, massive stars that formed so recently (~ 6 Myr) so close to the black hole cannot be explained by traditional star formation (Morris 1993). Understanding the properties of these young stars may help answer the question of how they formed, and spectroscopy provides a vital tool for studying these stars.

Binary stars play an important role in the formation mechanisms of massive stars, and works have shown that the majority of massive stars are formed in binary systems (Sana et al. 2012; de Mink et al. 2013; Duchêne & Kraus 2013). It is reasonable to expect young stars at the Galactic Center may be part of binary systems (Naoz et al. 2018). The value of young binary systems includes how they are more likely to remain intact today, whereas binary stars formed over a Gyr ago have mostly likely evaporated

or merged (Stephan et al. 2016; Stephan et al. 2019). The importance of binaries in stellar formation and their prevalence amongst massive stars are motivating factors in observational searches for binaries (Ott et al. 1999; Martins et al. 2006; Rafelski et al. 2007; Pfuhl et al. 2014; Chu et al. 2018; Gautam et al. 2019). These searches have identified three binary systems. Finding binary systems and constraining the binary fraction of the Galactic center stars can attest to particular methods of star formation.

Binary stars also play an important role in the dynamics of the region. One formation mechanism for the S-stars is the tidal breakup of a binary star system, where one star remains bound to the SMBH while the other component is ejected as a hypervelocity star (Hills 1988; Yu & Tremaine 2003; Perets et al. 2009; Brown 2015). Works such as Sana et al. (2012); de Mink et al. (2013) predict that the evolution of two massive components in a binary system will lead to interactions, including rotational spin-up, mass transfer, and collisions. Interactions between the binary systems and the SMBH via the Kozai-Lidov mechanism may lead to mergers between the binary stars (Naoz 2016; Stephan et al. 2016). These mergers may explain the existence of the intriguing G-sources identified in works such as Ciurlo et al. (2020). Binary stars with two massive components are considered likely progenitors of gravitational wave events that come from merging black holes or neutron stars (Abbott et al. 2016). With the Galactic Center hosting numerous massive, young stars, this region serves as a rich location for the progenitors of gravitational wave sources (Antonini & Perets 2012; Hoang et al. 2018).

Most searches for binaries at the Galactic Center have focused on eclipsing binaries, while spectroscopic searches have been more limited. That said, spectroscopic binaries make up an important part of the identified binary star population. Of the three identified binaries, two are both spectroscopic and eclipsing binaries (Pfuhl et al. 2014). Spectroscopic binaries can provide important parameters such as stellar mass and eccentricity. These reasons provide sufficient motivation to search for spectroscopic binaries at the Galactic center.

This thesis performs unprecedented investigations for spectroscopic binaries at the Galactic center. In Chapter 2 of this thesis, we describe the first direct search for binarity of its kind for the star S0-2, one of the most well-studied stars of the S-star cluster. We introduce a methodology for investigating periodicity and placing limits on binary parameters with radial velocity data. In Chapter 3, we explain the improvements in spectral analysis that lead to greater sensitivities to spectroscopic binary systems. In Chapter 4, we expand the direct search for spectroscopic binaries amongst the S-stars that was first introduced in Chapter 2, using the improvements in methodology in Chapter 3. We use this larger sample size to place limits on the intrinsic binary fraction of the S-star cluster. In Chapter 5, we report the observations of a 6 year integral field spectroscopic survey of the Galactic center. We include the spectral types of these stars, which can be further monitored in future binary star searches.

CHAPTER 2

Investigating the Binarity of S0-2: Implications for Its Origins and Robustness as a Probe of the Laws of Gravity around a Supermassive Black Hole

Reproduced by permission of The Astrophysical Journal

Chu et al. (2018)

The star S0-2, which orbits the supermassive black hole in our Galaxy with a period of 16 years, provides the strongest constraint on both the mass of the black hole and the distance to the Galactic center. S0-2 will soon also provide the first measurement of relativistic effects near a supermassive black hole. In this work, we report the first limits on the binarity of S0-2 from radial velocity monitoring, which has implications for both understanding its origin as well as its robustness as a probe of the gravitational field around the black hole. With 87 radial velocity measurements, which include 12 new observations presented here and which span 16 years, we have the data set to look for radial velocity variations from S0-2's orbital model. Using a Lomb-Scargle analysis and orbit fitting for potential binaries, we detect no radial velocity variation beyond S0-2's orbital motion and do not find any significant periodic signal. The lack of a binary companion does not currently distinguish between different formation scenarios for S0-2. The upper limit on the mass of a companion star ($M_{\rm comp}$) still allowed by our results has a median upper limit of $M_{\rm comp} \sin i \leq 1.6$ M$_\odot$ for periods between 1 and 150 days, the longest period to avoid tidal break up of the binary. We also investigate the impact of the remaining allowed binary system on the measurement of the relativistic redshift at S0-2's closest approach in 2018. While binary star systems are important to consider

for this experiment, we find plausible binaries for S0-2 will not alter a 5σ detection of the relativistic redshift.

2.1 Introduction

The source S0-2 is one of the most well studied stars at the Galactic center. It is important for our understanding of the properties of the Galaxy's central potential. In particular, it has provided the proof of the existence of a supermassive black hole (SMBH), the characterization of the SMBH properties (mass and distance) and the laws of gravitation (Ghez et al. 2005, 2008; Gillessen et al. 2009b, 2017; Boehle et al. 2016; Hees et al. 2017). S0-2 is also notable because spectroscopic studies have revealed that it, along with most of the "S-stars" located within $1''$ of the black hole, is a young main-sequence B star (Ghez et al. 2003; Eisenhauer et al. 2005; Martins et al. 2008; Habibi et al. 2017). This discovery raised questions about their formation mechanism, since traditional star formation would be disrupted by the tidal forces of the black hole (Morris 1993).

Works have investigated ways the S-stars may have formed and how these stars relate to the rest of the nuclear star cluster. Many theories for the S-starsFL formation have been proposed (see Alexander 2005, for a review). Two general classifications of mechanisms are considered for the S-stars: (1) binary star systems scattered from outside the region and then tidally disrupted, leaving behind one component of the original binary while the other is ejected as a hypervelocity star (Hills 1988; Perets et al. 2007), and (2) S-stars formed in the clockwise disk and then migrated to the central arcsecond around the SMBH (Levin 2007; Löckmann et al. 2008; Merritt et al. 2009). Previous works have also investigated how these S-stars relate to the clockwise disk, Wolf-Rayet stars, G2-like sources and evolved giants in the region (Paumard et al. 2006; Lu et al. 2009; Bartko et al. 2009; Do et al. 2009, 2013; Madigan et al. 2014; Chen & Amaro-Seoane 2014; Witzel et al. 2014, 2017; Phifer et al. 2013).

With binary stars playing a leading role in many of the S-star formation and evolution scenarios as well as in scenarios of other Galactic center stars, observational

searches for binaries are important. Thus far, photometric variations has been the primary search method. Several binaries have been revealed (Ott et al. 1999; Martins et al. 2006; Rafelski et al. 2007; Pfuhl et al. 2014), although none among the S-stars. However, eclipsing binaries are expected to be only a small fraction of the true binary population. With radial velocity (RV) measurements that now span more than a decade, there is an opportunity to search for RV variations in the brightest S-star cluster members.

Furthermore, S0-2 will be at its closest approach to the SMBH in 2018, which provides the opportunity to measure the relativistic redshift in S0-2's RV (Zucker et al. 2006; Angélil & Saha 2010, 2011; Hees et al. 2017). This first direct observation of a relativistic effect on S-stars orbit will improve with time after 2018 and be followed by other relativistic measurement such as the advance of the periastron. If S0-2 is actually a spectroscopic binary, it will bias the relativistic redshift measurement if binarity is not considered.

In this work, we explore the possibility of S0-2 to be a spectroscopic binary. This paper is organized as follows: In Section 2.2 we describe the observations and data used in this work, including new RV measurements. Section 2.3 describes the search for a companion star and the characterization of allowed hidden companions. Section 2.4 describes the impact allowed spectroscopic binaries would have on the relativistic redshift measurement. Section 2.5 interprets the results of the analysis and implications for S0-2 being a single star and the robustness of gravitational redshift measurements and future relativity studies based on S0-2's orbital motion.

2.2 Observations and Data

This investigation includes previously reported astrometric and spectroscopic data, as well as new spectroscopic data taken with the W. M. Keck Observatory (WMKO). All the WMKO spectroscopic observations used for S0-2 RV measurements are summarized in Table 2.1.

2.2.1 S0-2 Radial Velocities

2.2.1.1 Previously Reported Data

Over the past 16 years, S0-2 has been closely monitored spectroscopically. In the published literature, 24 RV measurements beginning in the year 2000 have been reported from WMKO (Ghez et al. 2003, 2005, 2008; Boehle et al. 2016) and 40 measurements beginning in 2003 from the VLT (Eisenhauer et al. 2005; Gillessen et al. 2009a, 2017; Habibi et al. 2017). Many of the RV measurements are based on multiple nights of observations. For this analysis, we are interested in the presence of binaries, which for S0-2 can have periods as short as $\sim$1 day. We therefore reextract S0-2's spectra from the previously calibrated WMKO data on a nightly basis for the following nights which were previously combined: 2009 May 5 and 6 to 2009.334, 2010 May 5 and 8 to 2010.349, 2012 June 8-11 to 2012.441, 2012 July 21 and 22 to 2012.556, 2012 August 12 and 13 to 2012.616, 2013 May 14 and 16 to 2013.369, 2013 July 25-27 to 2013.566, and 2013 August 10-13 to 2013.612 (see Table 2.1). This increases the Keck data set to 38 points for this time period. For the VLT, 7 out of 41 epochs are reported to be derived from multiple nights of data.

2.2.1.2 New Spectroscopic Data

We report new spectroscopic observations for S0-2 obtained using the integral field spectrograph OSIRIS (Larkin et al. 2006) on the W. M. Keck I telescope with the laser guide star AO system. These data were observed between 2014 to 2016. Details about the filters and integration time relate to these observations are given in Table 2.1. The RV observations and data analysis follow the same procedures used for earlier WMKO S0-2 RV measurements (Ghez et al. 2008; Do et al. 2013). The 8 new RV measurements, along with the RV measurements from Section 2.2.1.1 (38 Keck and 41 VLT) result in 87 total RV measurements used in this work (see Table 2.2).

Table 2.1. Summary of Keck Spectroscopic Observations

Date			$N_{\text{frames}} \times t_{\text{int}}$	FWHM [a]	Filter	Scale
(UT)	(MJD)	(Epoch)	(s)	(mas)		(mas)
2000-06-23	51718.50	2000.476	36×300		K [b]	18
2002-06-02	52427.50	2002.418	7×1200		K [c]	20
2002-06-03	52428.50	2002.420	4×1200		K' [c]	20
2003-06-08	52798.50	2003.433	2×1200		K' [c]	20
2004-06-23	53179.50	2004.476	16×1200		K' [c]	20
2005-05-30	53520.50	2005.410	7×1200		K' [c]	20
2005-07-03	53554.50	2005.503	7×900	58	Kbb	20
2006-05-23	53878.50	2006.390	4×900	74	Kbb	35
2006-06-18	53904.50	2006.461	9×900	65	Kn3	35
2006-06-30	53916.50	2006.494	9×900	59	Kn3	35
2006-07-01	53917.50	2006.497	9×900	64	Kn3	35
2007-05-21	54241.50	2007.384	2×900	86	Kn3	35
2007-07-19	54300.29	2007.545	2×900	56	Kn3	35
2008-05-16	54602.50	2008.372	11×900	57	Kn3	35
2008-07-25	54672.28	2008.563	9×900	60	Kn3	35
2009-05-05	54956.50	2009.342	7×900	60	Kn3	35
2009-05-06	54957.50	2009.344	12×900	69	Kn3	35
2010-05-05	55321.50	2010.341	6×900	67	Kn3	35
2010-05-08	55324.50	2010.349	11×900	69	Kn3	35
2011-07-10	55752.33	2011.520	6×900	71	Kn3	35

Table 2.1 (cont'd)

Date			$N_{\text{frames}} \times t_{\text{int}}$	FWHM [a]	Filter	Scale
(UT)	(MJD)	(Epoch)	(s)	(mas)		(mas)
2012-06-08	56086.50	2012.435	4×900	87	Kn3	35
2012-06-09	56087.50	2012.438	3×900	66	Kn3	35
2012-06-11	56089.50	2012.444	7×900	64	Kn3	20
2012-07-21	56129.31	2012.553	3×900	77	Kn3	35
2012-07-22	56130.31	2012.555	7×900	81	Kn3	35
2012-08-12	56151.33	2012.613	6×900	56	Kn3	35
2012-08-13	56152.27	2012.615	7×900	99	Kn3	35
2013-05-11	56423.50	2013.358	11×900	73	Kbb	35
2013-05-12	56424.50	2013.361	11×900	62	Kbb	35
2013-05-13	56425.50	2013.363	12×900	61	Kbb	35
2013-05-14	56426.50	2013.366	11×900	61	Kn3	35
2013-05-16	56428.50	2013.372	7×900	98	Kn3	20
2013-05-17	56429.50	2013.374	7×900	64	Kn3	20
2013-07-25	56498.33	2013.563	11×900	79	Kn3	35
2013-07-26	56499.34	2013.566	6×900	73	Kn3	35
2013-07-27	56500.33	2013.568	11×900	66	Kn3	35
2013-08-10	56514.29	2013.607	7×900	62	Kn3	35
2013-08-11	56515.31	2013.609	9×900	69	Kn3	35
2013-08-13	56517.29	2013.615	12×900	67	Kn3	35
2014-05-18	56795.50	2014.376	13×900	66	Kn3	35

Table 2.1 (cont'd)

Date			$N_{\text{frames}} \times t_{\text{int}}$	FWHM [a]	Filter	Scale
(UT)	(MJD)	(Epoch)	(s)	(mas)		(mas)
2014-05-23	56800.50	2014.390	10×900	76	Kn3	35
2014-07-03	56841.36	2014.502	8×900	66	Kn3	35
2015-05-04	57146.50	2015.337	5×900	68	Kn3	35
2015-07-21	57224.35	2015.551	5×900	56	Kn3	35
2016-05-14	57522.50	2016.367	8×900	78	Kbb	35
2016-05-15	57523.50	2016.370	4×900	80	Kbb	35
2016-05-16	57524.50	2016.372	8×900	84	Kbb	35

[a]Average FWHM of S0-2 in the mosaic made of all frames, measured by fitting a two-dimensional Gaussian to the source.

[b]Taken with NIRSPEC slit spectrograph

[c]Taken with NIRC2 slit spectrograph

2.2.2 Characteristics of the Two Datasets

The Keck and VLT data sets are analyzed in a similar manner and appear to be consistent with one another. The two datasets are analyzed with the same standard spectroscopic calibration procedures and the absolute wavelength solutions are both determined from the OH sky emission lines. The radial velocity of S0-2 is measured from both data sets by fitting a Gaussian to the Brγ absorption line. The reported average RV uncertainties are very similar, 33 km s^{-1}and 45 km s^{-1}for Keck and VLT, respectively. Furthermore, for the 4 Keck and VLT points taken within 10 days of each other, 3 of the points were within 1σ of each other. The one exception is the Keck 2003.433 point, which differs from a nearby VLT point by 2σ. We conclude there is no significant systematic difference.

2.2.3 Removing S0-2's Long-term RV Variations

Before searching for short-term RV variations, we remove the long-term RV variations from S0-2's orbital motion around the SMBH. To create the long-term RV model, a simultaneous orbital fit of S0-2 and S0-38 was performed using the same S0-2 and S0-38 astrometry and process as Boehle et al. (2016), but with the S0-2 RVs in Table 2.2 and S0-38 RVs from Boehle et al. (2016); Gillessen et al. (2017). One additional change is the format of time used. In this work, we use Modified Julian Date (MJD). The reported time is the approximate average time of the observations taken during the night. For convenience, we also report the Universal Time (UT) and epoch time reported in Julian years of 365.25 days since J2000. Previously, Boehle et al. (2016) defined the epoch year as 365.24 days. The orbital parameters resulting from the fit are consistent with Boehle et al. (2016) within 1σ and are presented in the Appendix A.1. The RV data, model and residual are shown in Figure 2.1 and given in Table 2.2. The average scatter around the orbit residual is 20 km s^{-1} with a standard deviation of 26 km s^{-1}. The Keck and VLT datasets are individually consistent with these values.

Table 2.2. S0-2 Radial Velocity Measurements

UT	MJD	Epoch [a]	$RV_{\rm obs}$ (km s^{-1})	RV σ (km s^{-1})	$V_{\rm LSR}$ [b] (km s^{-1})	$RV_{\rm LSR}$ [c] (km s^{-1})	RV [d] Source	Model (km s^{-1})	Model σ (km s^{-1})	Residual [e] (km s^{-1})
2000-06-23	51718.50	2000.476	1192	100	7	1199	(2)	1152	15	47
2002-06-02	52427.50	2002.418	-513	36	18	-495	(2)	-486	28	-9
2002-06-03	52428.50	2002.420	-550	44	18	-532	(2)	-554	27	22
2003-04-10	52739.23	2003.271		59		-1571	(3)	-1592	12	21
2003-05-10	52769.18	2003.353		40		-1512	(3)	-1547	11	35
2003-06-08	52798.50	2003.433	-1556	22	15	-1541	(2)	-1507	10	-34
2003-06-13	52803.15	2003.446		51		-1428	(3)	-1500	10	72
2004-06-23	53179.50	2004.476	-1151	57	8	-1143	(2)	-1121	7	-22
2004-07-14	53200.91	2004.535		46		-1055	(3)	-1104	7	49
2004-07-15	53201.64	2004.537		37		-1056	(3)	-1104	7	48
2004-08-19	53236.34	2004.632 [f]		39		-1039	(3)	-1078	7	39
2005-02-27	53428.46	2005.158		77		-1001	(3)	-948	6	-53

Table 2.2 (cont'd)

UT	MJD	Epoch [a]	$RV_{\rm obs}$ (km s^{-1})	RV σ (km s^{-1})	$V_{\rm LSR}$ [b] (km s^{-1})	$RV_{\rm LSR}$ [c] (km s^{-1})	RV [d] Source	Model (km s^{-1})	Model σ (km s^{-1})	Residual [e] (km s^{-1})
2005-03-19	53448.18	2005.212		37		-960	(3)	-936	6	-24
2005-03-20	53449.28	2005.215		54		-910	(3)	-935	6	25
2005-05-30	53520.50	2005.410	-945	23	19	-926	(2)	-893	6	-33
2005-06-15	53536.94	2005.455		60		-839	(3)	-884	6	45
2005-06-18	53539.13	2005.461		43		-907	(3)	-882	6	-25
2005-07-03	53554.50	2005.503	-845	34	3	-842	(2)	-874	6	32
2005-09-05	53618.02	2005.677 [f]		77		-774	(3)	-838	6	64
2005-10-08	53651.63	2005.769 [f]		58		-860	(3)	-820	6	-40
2006-03-16	53810.51	2006.204		42		-702	(3)	-739	5	37
2006-04-22	53847.40	2006.305		77		-718	(3)	-721	5	3
2006-05-23	53878.50	2006.390	-715	21	23	-692	(2)	-707	5	14
2006-06-18	53904.50	2006.461	-728	17	10	-718	(2)	-694	5	-24

Table 2.2 (cont'd)

UT	MJD	Epoch [a]	$RV_{\rm obs}$ (km s^{-1})	RV σ (km s^{-1})	$V_{\rm LSR}$ [b] (km s^{-1})	$RV_{\rm LSR}$ [c] (km s^{-1})	RV [d] Source	Model (km s^{-1})	Model σ (km s^{-1})	Residual [e] (km s^{-1})
2006-06-30	53916.50	2006.494	-699	36	4	-695	(2)	-689	5	-6
2006-07-01	53917.50	2006.497	-717	37	4	-713	(2)	-688	5	-25
2006-08-16	53963.92	2006.624 [f]		57		-658	(3)	-667	5	9
2007-03-26	54185.26	2007.230		57		-586	(3)	-570	5	-16
2007-04-22	54212.29	2007.304		57		-537	(3)	-558	5	21
2007-05-21	54241.50	2007.384	-507	50	24	-483	(2)	-546	5	63
2007-07-19	54300.29	2007.545	-502	50	-4	-506	(2)	-522	5	16
2007-07-21	54302.14	2007.550 [f]		57		-505	(3)	-521	5	16
2007-09-04	54347.06	2007.673 [f]		57		-482	(3)	-503	4	21
2008-04-06	54562.20	2008.262 [f]		27		-394	(3)	-418	4	24
2008-05-16	54602.50	2008.372	-443	32	26	-417	(2)	-402	4	-15
2008-06-06	54623.92	2008.431		62		-425	(3)	-394	4	-31

Table 2.2 (cont'd)

UT	MJD	Epoch [a]	$RV_{\rm obs}$ (km s^{-1})	RV σ (km s^{-1})	$V_{\rm LSR}$ [b] (km s^{-1})	$RV_{\rm LSR}$ [c] (km s^{-1})	RV [d] Source	Model (km s^{-1})	Model σ (km s^{-1})	Residual [e] (km s^{-1})
2008-07-25	54672.28	2008.563	-373	43	-7	-380	(2)	-375	4	-5
2009-05-05	54956.50	2009.342	-282	30	30	-252	(2)	-268	4	17
2009-05-06	54957.50	2009.344	-315	32	30	-285	(2)	-268	4	-17
2009-05-21	54972.37	2009.385		45		-241	(3)	-262	4	21
2010-05-08	55324.50	2010.349	-152	22	29	-123	(2)	-131	4	9
2010-05-10	55326.30	2010.354		27		-134	(3)	-131	4	-3
2011-04-27	55678.03	2011.317		34		-3	(3)	3	3	-6
2011-07-10	55752.33	2011.520	14	23	0	14	(2)	32	3	-19
2011-07-27	55769.35	2011.567		57		35	(3)	39	3	-4
2012-03-18	56004.20	2012.210		34		185	(3)	135	3	50
2012-05-05	56052.42	2012.342		34		167	(3)	155	3	12
2012-06-08	56086.50	2012.435	128	25	15	143	(2)	169	3	-26

Table 2.2 (cont'd)

UT	MJD	Epoch [a]	$RV_{\rm obs}$ (km s^{-1})	RV σ (km s^{-1})	$V_{\rm LSR}$ [b] (km s^{-1})	$RV_{\rm LSR}$ [c] (km s^{-1})	RV [d] Source	Model (km s^{-1})	Model σ (km s^{-1})	Residual [e] (km s^{-1})
2012-06-09	56087.46	2012.438	141	34	14	155	(2)	170	3	-15
2012-06-11	56089.50	2012.444	151	50	13	164	(2)	171	3	-6
2012-06-29	56107.93	2012.494		34		195	(3)	179	3	16
2012-07-06	56114.87	2012.513		34		186	(3)	182	3	4
2012-07-21	56129.31	2012.553	178	56	-6	172	(2)	188	3	-16
2012-07-22	56130.31	2012.555	200	8	-6	194	(2)	188	3	6
2012-08-12	56151.33	2012.613	213	25	-13	200	(2)	197	3	2
2012-08-13	56152.27	2012.615	199	24	-14	186	(2)	198	3	-12
2012-09-15	56185.00	2012.705		45		190	(3)	212	3	-22
2013-04-06	56388.45	2013.262		23		313	(3)	306	3	7
2013-05-11	56423.50	2013.358	295	38	28	323	(1)	323	3	-0
2013-05-12	56424.50	2013.361	298	22	27	325	(1)	323	3	2

Table 2.2 (cont'd)

UT	MJD	Epoch [a]	$RV_{\rm obs}$ (km s^{-1})	RV σ (km s^{-1})	$V_{\rm LSR}$ [b] (km s^{-1})	$RV_{\rm LSR}$ [c] (km s^{-1})	RV [d] Source	Model (km s^{-1})	Model σ (km s^{-1})	Residual [e] (km s^{-1})
2013-05-13	56425.50	2013.363	251	39	27	278	(1)	324	3	-46
2013-05-14	56426.50	2013.366	272	16	27	298	(2)	324	3	-26
2013-05-16	56428.50	2013.372	286	24	26	311	(2)	325	3	-14
2013-05-17	56429.50	2013.374	287	30	25	312	(1)	326	3	-13
2013-07-25	56498.33	2013.563	367	15	-7	360	(2)	360	4	1
2013-07-26	56499.34	2013.566	366	39	-7	359	(2)	360	4	-2
2013-07-27	56500.33	2013.568	367	39	-8	360	(2)	361	4	-1
2013-08-10	56514.29	2013.607	393	32	-13	380	(2)	368	4	12
2013-08-11	56515.31	2013.609	354	40	-13	341	(2)	368	4	-27
2013-08-13	56517.29	2013.615	353	44	-14	340	(2)	369	4	-30
2013-08-27	56531.99	2013.655		45		361	(3)	377	4	-16
2013-09-22	56557.92	2013.726		34		384	(3)	390	4	-6

Table 2.2 (cont'd)

UT	MJD	Epoch [a]	$RV_{\rm obs}$ (km s^{-1})	RV σ (km s^{-1})	$V_{\rm LSR}$ [b] (km s^{-1})	$RV_{\rm LSR}$ [c] (km s^{-1})	RV [d] Source	Model (km s^{-1})	Model σ (km s^{-1})	Residual [e] (km s^{-1})
2014-03-09	56725.57	2014.185		28		490	(3)	481	4	9
2014-04-07	56754.06	2014.263		34		515	(3)	497	4	18
2014-05-18	56795.50	2014.376	481	32	25	506	(1)	522	4	-16
2014-05-23	56800.50	2014.390	500	33	23	523	(1)	525	4	-2
2014-07-03	56841.36	2014.502	553	15	3	556	(1)	550	4	6
2014-07-10	56848.30	2014.521		17		568	(3)	554	4	14
2015-04-20	57132.46	2015.299		23		765	(3)	751	5	14
2015-05-04	57146.50	2015.337	743	28	31	774	(1)	762	5	12
2015-07-21	57224.35	2015.551	829	41	-5	823	(1)	826	5	-3
2015-09-16	57281.12	2015.706		45		869	(3)	877	5	-8
2016-04-14	57492.23	2016.284		45		1081	(3)	1100	8	-19
2016-05-14	57522.50	2016.367	1081	36	26	1107	(1)	1138	8	-31

Table 2.2 (cont'd)

UT	MJD	Epoch [a]	$RV_{\rm obs}$ (km s^{-1})	RV σ (km s^{-1})	$V_{\rm LSR}$ [b] (km s^{-1})	$RV_{\rm LSR}$ [c] (km s^{-1})	RV [d] Source	Model (km s^{-1})	Model σ (km s^{-1})	Residual [e] (km s^{-1})
2016-05-15	57523.50	2016.370	1139	33	26	1165	(1)	1140	8	26
2016-05-16	57524.50	2016.372	1117	16	26	1142	(1)	1141	8	1
2016-07-09	57578.06	2016.519		34		1198	(3)	1214	9	-16

[a]The epoch time is reported in Julian years 365.25 days since J2000.

[b]The values came from $rvcorrect$ task in IRAF, with an error less than 1 km s^{-1}(Kerr & Lynden-Bell 1986). For ease of viewing, values have been rounded.

[c]Velocity after applying the $V_{\rm LSR}$ correction. For ease of viewing, values have been rounded.

[d]Measurement reported in (1) this work, (2) Boehle et al. (2016) and (3) Gillessen et al. (2017).

[e]$RV_{\rm LSR}$ $-$ model. For ease of viewing, values have been rounded.

[f]VLT combined nights data.

2.3 Is S0-2 a Binary?

In this section, we use two different methods to to search for periodic signals in the RV residuals: (i) the Lomb-Scargle periodogram (Lomb 1976; Scargle 1982; Astropy Collaboration et al. 2013) and (ii) a Bayesian fit for potential binaries. The former method provides quick overview of the data; we note that while it may not be as effective at detecting highly eccentric binaries (e.g. phase dispersion measure (Stellingwerf 1972), minimum string length (Dworetsky 1983)), it is an computationally efficient method for detecting periodic signals in unevenly spaced data (see Appendix A.2). The latter method provides a more complete and robust, albeit more computationally expensive approach and allows us to derive upper limits on the orbital parameters of an hypothetical binary companion to S0-2.

We can place an upper limit on the orbital period of any possible companion around S0-2 of 119.2 days based on a binary disruption criteria. A binary would be tidally disrupted at closest approach to the SMBH if it has a separation greater than the Hill radius ($r_{\rm H}$). The Hill radius is given by

$$r_{\rm H} = a_{\text{S0-2}}(1 - e_{\text{S0-2}}) \sqrt[3]{\frac{M_{\text{Primary}}}{3M_{BH}}}\,, \tag{2.1}$$

where M_{Primary} is the primary mass, $a_{\text{S0-2}}$ and $e_{\text{S0-2}}$ are the semimajor axis and eccentricity for the binary-black hole system (the corresponding values have been derived from the orbital fit presented in Section 2.2.3 whose result is presented in Appendix A.1). This Hill Radius limit is a conservative limit since any eccentricity of the inner binary system would decrease the stability of the system. We take the condition $a(1+e) < r_{\rm H}$, where e is the eccentricity and a the semi-major axis of the inner binary, to allow for long term stability (Naoz 2016), which leads to the following constraint on the binary period P

$$P^2 < \frac{4\pi^2}{3GM_{BH}} a_{\text{S0-2}}^3 \frac{(1 - e_{\text{S0-2}})^3}{(1+e)^3} \frac{M_{\text{Primary}}}{M_{tot}}\,. \tag{2.2}$$

This condition needs to be fulfilled to avoid a disruption of the binary. We therefore

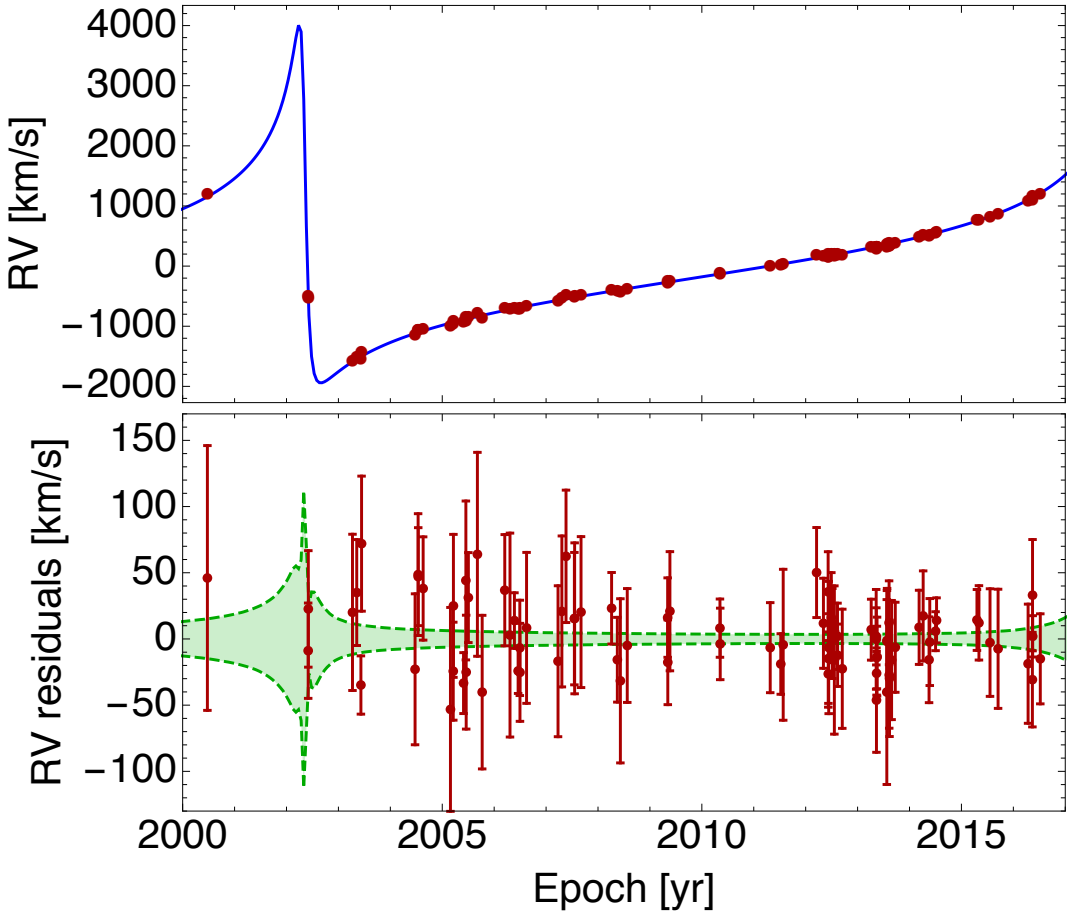

Figure 2.1: Top: S0-2's radial velocity measurements over time and best fit model. Bottom: Residual radial velocity curve. Dashed lines are the 1σ model uncertainties.

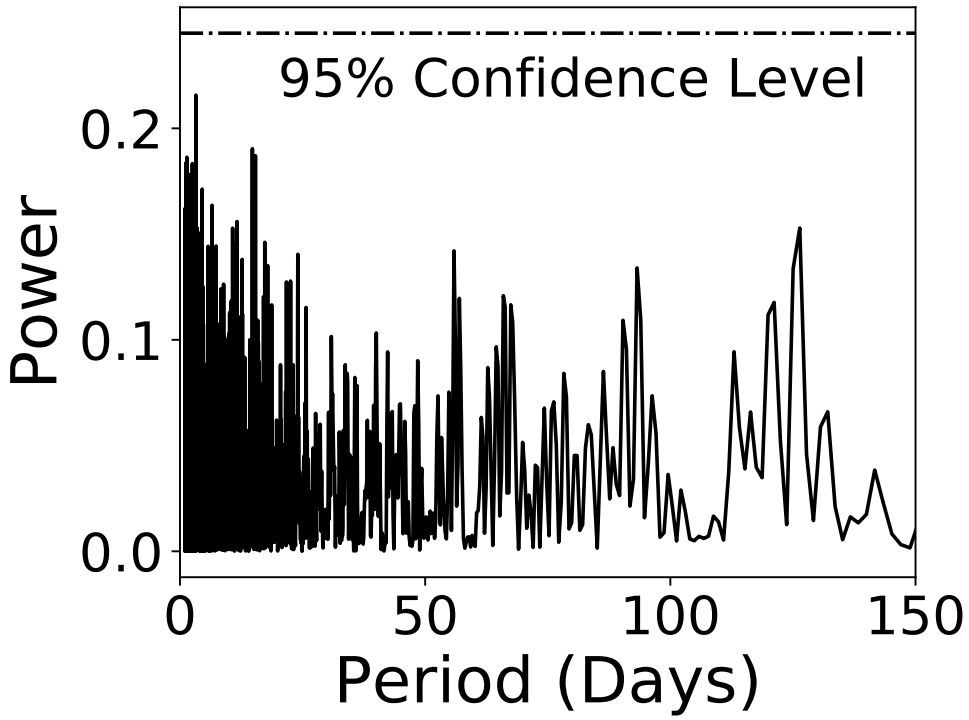

Figure 2.2: Lomb-Scargle periodogram of S0-2's residual radial velocity curve. The black dash-dotted line is the 95% confidence level detection value. No power reaches the 95% confidence level detection value implying that no significant periodic signal is found in the observations.

sampled periods between 1 and 150 days to search for a significant periodic signal.

The Lomb-Scargle analysis on S0-2's RV does not reveal any statistically significant peak (see Figure 2.2). We note that the structure of this periodogram is unaffected by the model uncertainties over the period range searched. In order to determine the relationship between periodogram power and statistical significance, we ran a series of Monte Carlo simulations. We first generated 100,000 simulated residual RV curves with no periodic signal. The simulated points had the same observation times and uncertainties as the data and were drawn from a Gaussian centered around 0 km s^{-1}. We produced a periodogram for each simulated RV curve and found the maximum peak power value. We then looked at the distribution of these maximum power values and made a cumulative distribution function (CDF). We used this CDF to determine the significance for periodic detections. These simulations set the 95% confidence level detection limit to

be 0.25, shown in a dotted line in Figure 2.2. The periodogram corresponding to S0-2's observations never reaches this value, which implies that no significant periodic signal is found in the current data and that observations are consistent with a single star model.

Since no evidence of a binary for S0-2 is found, we can place an upper limit on the amplitude of the RV variations induced by a binary system. In order to infer such a limit, we fit the S0-2 RV residuals with a binary star RV model plus a constant. The following equation was used to model the RV curve of an eccentric binary system (Hilditch 2001)

$$RV = K \frac{\sqrt{1-e^2}\cos E \cos\omega - \sin E \sin\omega}{1 - e\cos E}\,, \tag{2.3}$$

with

$$K = \frac{2\pi a \sin i}{P}\,, \tag{2.4}$$

and where e is the binary eccentricity, ω the argument of periastron, E the eccentric anomaly determined by solving the Kepler equation, i the inclination, P the period and a the semimajor axis. This model is parametrized using the following 5 variables: the offset O, the RV amplitude K, the eccentricity e, the argument of periastron ω and the mean longitude at J2000 (noted L_0). The use of the mean longitude at J2000 is preferred to the usual time of closest approach which is not bounded and not defined in case of circular orbits (Hilditch 2001). For different fixed binary orbital periods P, we fitted this model to the RV residuals using a MultiNest sampler (Feroz & Hobson 2008; Feroz et al. 2009, 2013). The resulting 95% upper confidence limit on K for $\sim$3000 orbital periods ranging from 1 to 150 days is shown in Figure 2.3.

Like the Lomb-Scargle analysis, this method is also sensitive to periodic signals in the data. A periodic signal would yield a significant non-zero peak in the value of K in the posterior, as opposed to a power law decreasing posterior. This method also takes inherently into account the other orbital parameters of the binary system that can affect the shape of the curve (e.g. eccentricity).

With one further assumption, this analysis also allows us to constrain the mass of a

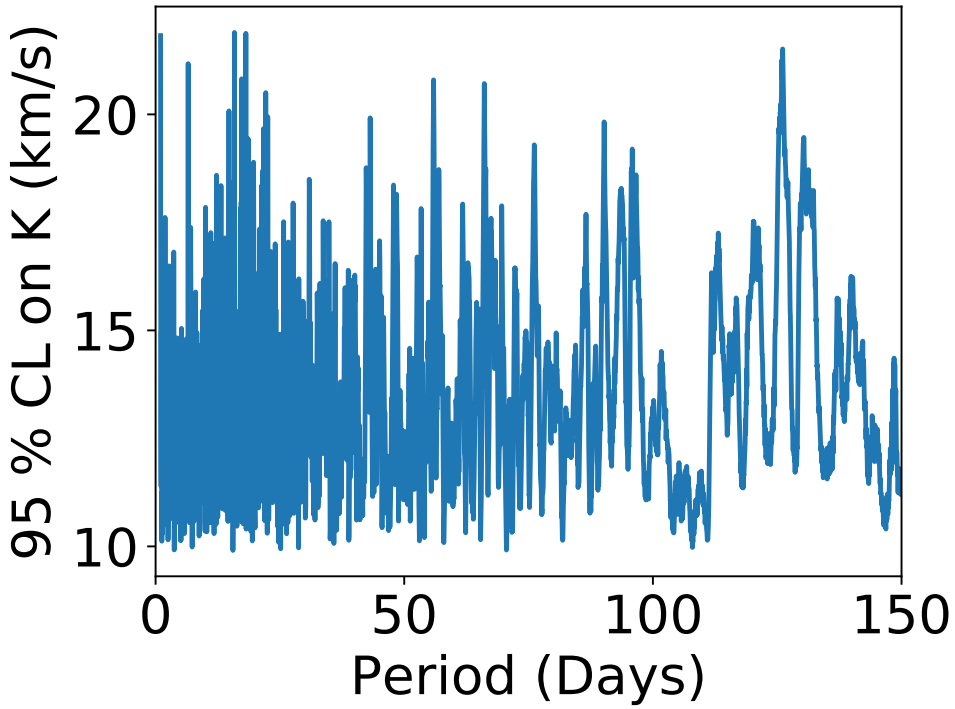

Figure 2.3: 95% upper confidence limit on the amplitude of RV variations induced by a binary system (K) as a function of the binary orbital period.

hypothetical companion. Assuming a total mass of the system ($M_{\rm tot}$), we transform the sampling (i.e. the chain) resulting from the MultiNest run into a companion mass limit by using

$$M_{\rm comp} \sin i = \left(\frac{P M_{tot}^2}{2\pi G} \right)^{1/3} K \,, \tag{2.5}$$

where $M_{\rm comp}$ is the companion mass and i the inclination of the binary system. From this transformed chain, we can derive an upper 95% confidence limit on $M_{\rm comp} \sin i$. This limit depends on the total mass $M_{\rm tot}$ used in Equation 2.5. In this work, two extreme values for $M_{\rm tot}$ are considered: (i) a low value of $M_{\rm tot}$= 10 $M_\odot$(Habibi et al. (2017) reported the mass of S0-2 as $13.6^{+2.2}_{-1.8}$ $M_\odot$), and (ii) a high value of $M_{\rm tot}$= 20 $M_\odot$. The upper limit on $M_{\rm comp} \sin i$ is shown in Figure 2.4 as well as the excluded region inferred by theoretical arguments based on the on the binary disruption criteria[1] and characterized by equation 2.2. The median upper 95% confidence limit for $M_{\rm comp} \sin i$ for all periods is 1.6 $M_\odot$assuming a total mass of 20 $M_\odot$while its maximal value is 3.1 $M_\odot$at 90.2 days period. These values decrease by 36 % for a total mass $M_{\rm tot}$of 10.0 $M_\odot$.

2.4 Impact of Hidden Allowed Companions On Measurement of S0-2's Relativistic Redshift

As anticipated by many theorists, observations of short-period stars orbiting the SMBH in our Galactic center are currently opening a new window to test the gravitational theory and to measure relativistic effects (see e.g. Rubilar & Eckart (2001); Zucker et al. (2006); Will (2008); Borka et al. (2013); Zakharov et al. (2016); Johannsen (2016a,b); Psaltis et al. (2016); Hees et al. (2017) and references therein). The relativistic redshift on S0-2's RV is the first relativistic effect expected to be detected with S0-2's closest approach in 2018 (Zucker et al. 2006; Angélil & Saha 2010, 2011; Hees et al. 2017). This measurement of the relativistic redshift will improve with time in the future and

[1]Interactions from background stars (Hopman 2009) and the eccentric Kozai-Lidov mechanism (Li et al. 2017) can also disrupt or merge binaries. We do not consider these scenarios because these effects depend on many variables, such as the age of the binary.

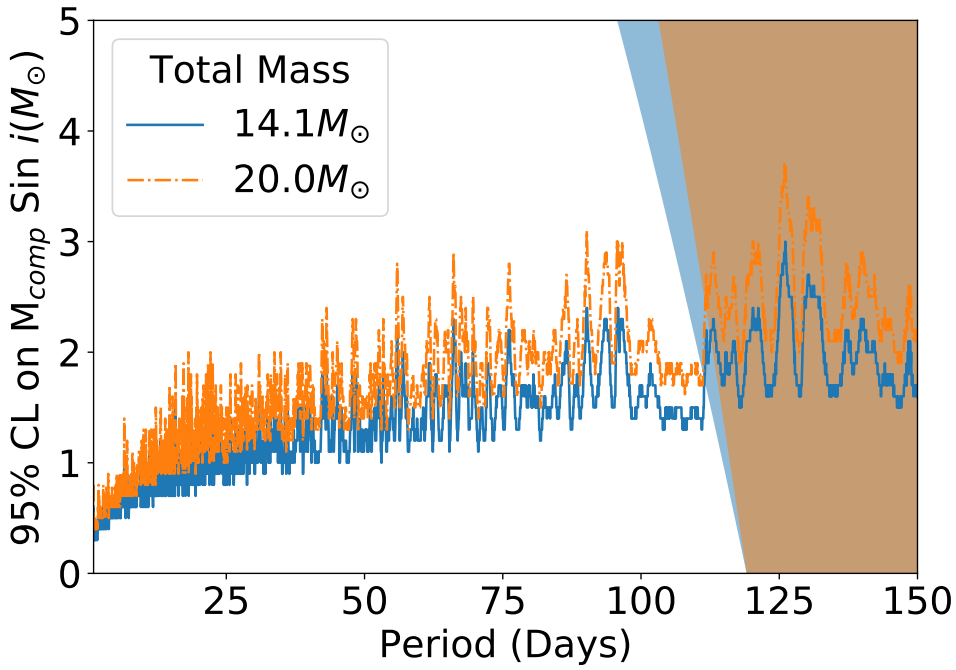

Figure 2.4: The 95% confidence level of the $M_{\rm comp} \sin i$ upper limit for a given period. This comes from the transformation of MultiNest chain using the binary mass equation 2.5. The shaded regions represent periods and companion masses excluded by the Hill radius limits from equation 2.2 while adopting a circular orbit.

will also be followed by measurements of more relativistic effects such as the advance of S0-2's periastron. In the case where S0-2 is a binary system, the measurement of the relativistic effects like the redshift would be altered. The goal of this section is to quantify the impact of a binarity of S0-2 on the measurement of its relativistic redshift.

One way to measure the relativistic redshift is to model the total radial velocity as $RV = [RV]_{\text{Newton}} + \Upsilon\,[RV]_{\text{rel}}$, where $[RV]_{\text{Newton}}$ is the standard Newtonian radial velocity, Υ a dimensionless parameter whose value is equal to 1 in GR and $[RV]_{\text{rel}}$ is the first order relativistic contribution to the RV given by

$$[RV]_{\text{rel}} = \frac{v^2}{2c} + \frac{GM_{BH}}{rc}\,, \tag{2.6}$$

with c the speed of light in a vacuum and r the norm of the star's position with respect to the SMBH and v the norm of its velocity. The first term is a contribution due to special relativity while the second term corresponds to the gravitational redshift. For a Keplerian orbit, the two contributions are exactly the same (up to a constant factor), meaning that only their combination can be measured. The relativistic redshift contribution to S0-2's RV reaches 200 km/s at closest approach in 2018 while the Newtonian part is ranging from -2000 km/s to 4000 km/s (see Figure 2.1). The idea is to fit Υ simultaneously with the other parameters in the orbital fit: a value significantly different from 0 but compatible with 1 would be a successful detection of the relativistic redshift while a value significantly different from 1 would indicate a deviation from GR. The goal of this section is to quantify the impact of a plausible binary for S0-2 on the determination of Υ.

The methodology consists in simulating data assuming S0-2 is a binary star using a relativistic modeling (in particular we use $\Upsilon = 1$) and analyze these data using a modeling where S0-2 is a single star and where Υ is a free parameter. The deviation $\Upsilon - 1$ obtained in this analysis is therefore entirely due to the fact that S0-2 has been simulated as a binary star.

More precisely, we simulate astrometric and RV data for S0-2 using a relativis-

tic modeling that includes the Römer time delay and the redshift (see e.g. Alexander (2005)). The simulated epochs correspond to epochs where we actually have data (see Table 2.2) and for each simulated data, we assign an uncertainty that corresponds to the actual measurement. In addition to existing data, we included simulated data for 2018: 10 spectroscopic observations which were assigned an uncertainty of 25 km/s and 4 astrometric observations which were assigned an uncertainty of 0.3 mas. The epochs for these additional observations have been chosen to optimize a redshift measurement within the 2018 observation window. At this step, the simulated data corresponds to perfect measurements in the case where S0-2 is a single star. Therefore, an orbital fit using these simulated data recovers the input value, i.e. gives an estimate of $\Upsilon = 1$ as expected.

To these simulated data, we then add the signature produced by a binary star given by Eq. (4.1). The obtained data now corresponds to a binary system. This dataset is then used in a one star orbital fit that includes the GM_{BH}, the distance to our Galactic center R_0, the position and velocity of the BH, the 6 orbital parameters for the star and the relativistic redshift parameter Υ. The impact of the binarity of S0-2 on the redshift measurement will be given by the estimated value[2] of $\Upsilon - 1$.

This procedure has been performed for 6 different binary orbital periods: 2, 5, 10, 25, 50 and 100 days. For each of these periods, we draw 2000 samples for the other binary orbital parameters (eccentricity e, RV amplitude K, argument of periastron ω and longitude at J2000 L_0) from the posterior probability distribution function of the fit described in Section 2.3. The resulting distributions for the bias in the redshift measurement $\Upsilon - 1$ are presented in Fig. 2.5 and 2.6. Furthermore, the values of the half of the 68% upper limit on the absolute value of the redshift bias are given in Tab. 2.3.

Although a plausible binary for S0-2 can bias the measurement of the relativistic redshift, this bias is always smaller than the uncertainty corresponding to a 5σ detection of the redshift (a 5σ detection is characterized by $\sigma_\Upsilon = 0.2$).

[2]We use the median as the estimated value from the MultiNest fit.

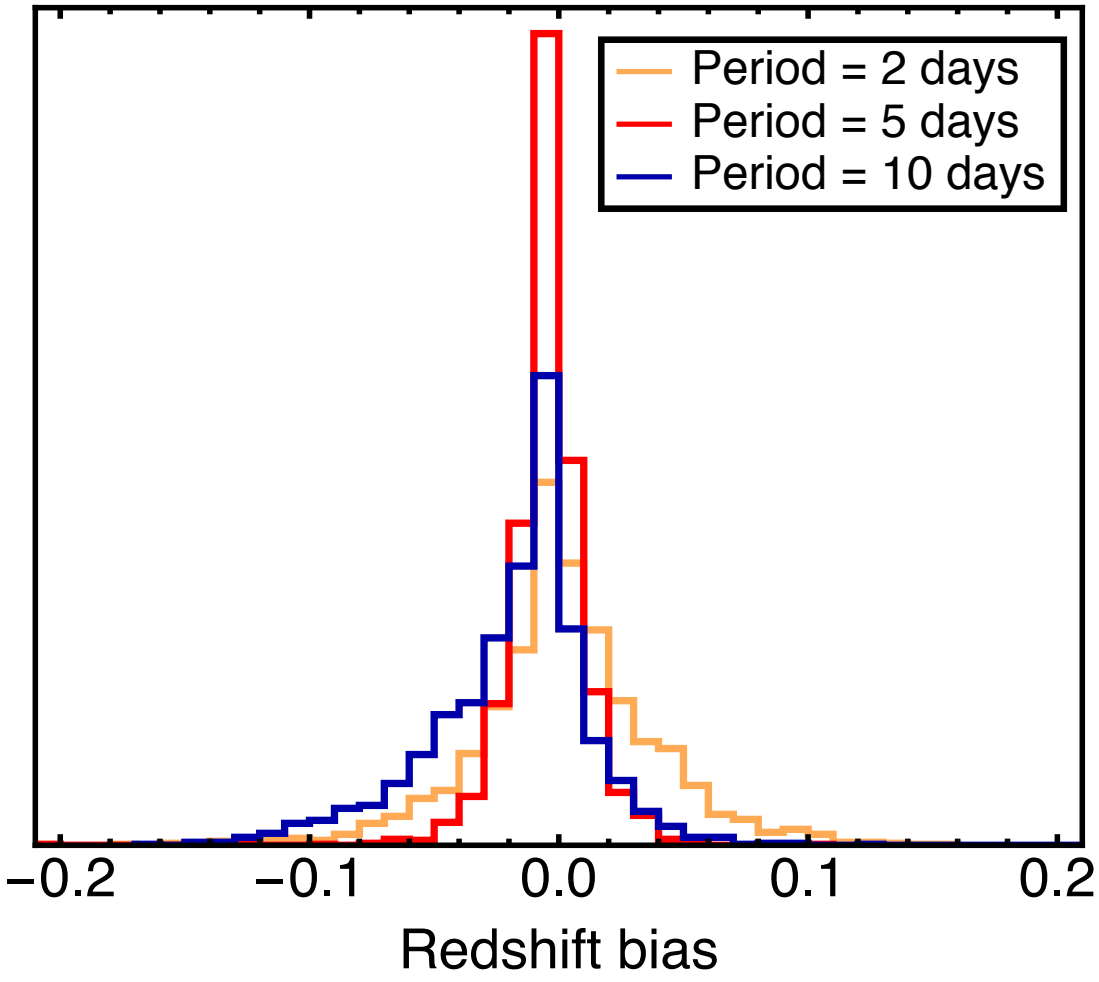

Figure 2.5: Bias on the estimation of relativistic redshift ($\Upsilon - 1$) using S0-2's observations up to 2018 produced if S0-2 is a binary system whose orbital parameters are allowed from the analysis presented in Section 2.3. The different curves corresponds to different binary periods.

Table 2.3. Impact of a binarity of S0-2 on a measurement of the relativistic redshift.

Binary period	95 % upper C.L. on K [km/s]	Uncertainty on the redshift due to the binarity (σ_Υ)
2 days	16.0	0.031
5 days	10.4	0.011
10 days	12.2	0.026
25 days	12.6	0.051
50 days	11.0	0.036
100 days	12.9	0.039

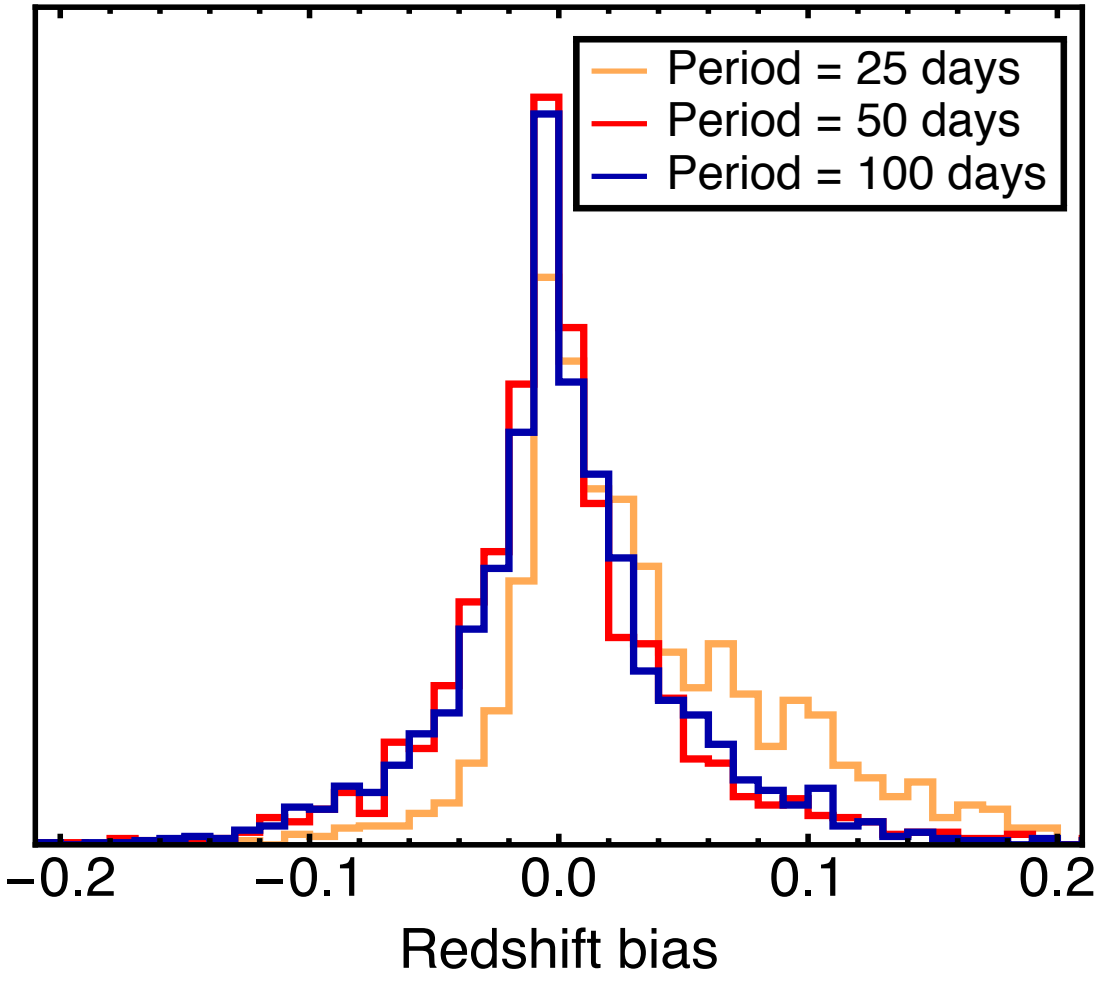

Figure 2.6: Bias on the estimation of relativistic redshift ($\Upsilon - 1$) using S0-2's observations up to 2018 produced if S0-2 is a binary system whose orbital parameters are allowed from the analysis presented in Section 2.3. The different curves corresponds to different binary periods.

2.5 Discussion and Conclusion

2.5.1 S0-2 in its astrophysical context

This is the first work that investigates S0-2 as a spectroscopic binary. Previous searches have concentrated on brighter sources such as IRS16SW and E60 (Pfuhl et al. 2014), located beyond the S-star cluster region (outside of $\sim$0.04 pc). This work has pushed the RV searches to 2 magnitudes fainter from K = 12.0 (E60) down to K = 14.0; physically, this magnitude difference corresponds to the difference between evolved Wolf-Rayet stars and main-sequence B stars. The improvements here are driven by the large number of radial velocity measurements available for S0-2 from the long-baseline monitoring programs for this source (e.g., Boehle et al. 2016; Gillessen et al. 2017).

While we detect no significant binary signal in the radial velocity variations, we have been able to place stringent limits on the companion mass. Our limits of 1.8 $M_\odot$ are consistent with other observations of the star. For example, given our 95% confidence limit of 1.8 $M_\odot$, a star would have an observed brightness of K $\sim$ 18 mag at the Galactic center, corresponding to a factor of 40 times less flux than S0-2. This brightness ratio is consistent with the fact that S0-2's spectrum shows no sign of another set of spectral features, even with 10 years of spectra combined (Habibi et al. 2017). While our mass limits has a $\sin i$ degeneracy, the lack of detection of a double-lined source also shows that a face-on binary system is also very unlikely.

The lack of a binary companion does not distinguish between different formation scenarios for S0-2 at this time. No companion is expected if S0-2 is the remaining companion of a hypervelocity star (e.g. Hills 1988; Yu & Tremaine 2003; Perets et al. 2009), or if it is the product of a merger (e.g. Sana et al. 2012; Phifer et al. 2013; Witzel et al. 2014; Stephan et al. 2016). Scattering from the young star cluster (at 0.1 to 0.5 pc) could also bring S0-2 in without a companion (Perets et al. 2007; Madigan et al. 2014). While the current observations of S0-2 are unable to distinguish these scenarios, companion searches of the other S-stars should be able to provide a much more com-

prehensive test of the formation scenarios for the S-stars. We have concentrated on S0-2 because the other S-stars are all fainter, which results in lower precision in their radial velocities compared to S0-2. Additional measurements should improve the sensitivity of companion searches.

2.5.2 S0-2 as a new probe of fundamental physics

The relativistic redshift at S0-2's closest approach in 2018 will be the first measurement of its kind, so understanding all sources of bias will be especially important for a significant detection. We have shown that a binary companion below our current detection limit for S0-2 can bias this measurement, as shown in Sec. 2.4. Nevertheless, this bias is always smaller than the uncertainty corresponding to a 5σ detection of the redshift. The values reported in Tab. 2.3 should be taken into account in the estimation of the uncertainty produced by all systematic effects in 2018. We would like to emphasize that the 2018 observations campaign is expected to reduce this possible bias.

Continued monitoring of S0-2 beyond 2018 provides further opportunities to observe other relativistic effects, such as the advance of the periastron. The impact that a plausible binary system would have on these relativistic measurements is left for further work.

CHAPTER 3

Systematic Investigations of Radial Velocity Measurements for Main-Sequence B-stars

Partially reproduced by permission of Science Magazine

Do et al. (2019)

Do et al. (2019) reported the relativistic redshift measurement of the star S0-2. A result of this scientific impact required immense investigation of our data methods. Given that relativistic redshift is primarily a spectroscopic result seen in S0-2's radial velocity, we focused heavily on improving our radial velocity measurement method. We employed a new method of measuring radial velocities using a Bayesian inference to fit synthetic spectral models to the data. With this new method, we improved the precision of our measurements by a factor of 1.7 compared to our previous method. Our resulting measurements were also a factor of 2.2 more precise than those reported by the VLT. Additionally, we observed radial velocity standard stars of similar spectral type to S0-2 to search for potential biases in our new radial velocity measurement method. We found that our new method retrieved the same radial velocity measurements reported in the literature, whereas our previous method resulted in measurements that were systematically higher. We conclude that our new method improves the precision and reduces the bias of our radial velocity measurements.

3.1 Introduction

When the young S-star S0-2 passed through closest approach to the supermassive black hole (SMBH) in the summer of 2018, its measured radial velocity (RV) was expected to show relativistic redshift (e.g. Hees et al. 2017). To improve the robustness of this detection, we carried out investigation of potential sources of bias. We found that a spectroscopic binary system would not significantly bias the detection of relativistic redshift measurement (Chu et al. 2018). We also worked to improve our RV measurement method. Previously, S0-2's RV was measured by fitting a Gaussian profile to the Brγ absorption line (see Chu et al. 2018, and references therein). We implemented a new method that fit a physical model (which includes properties of the star such as its effective temperature, surface gravity, and rotational velocity in addition to RV), to its observed spectrum. We wanted to see if this new method could: 1) improve the precision of our RV measurements and 2) reduce potential measurement biases by comparing measured values to reported literature values. Verifying these improvements would improve the robustness of our relativistic redshift detection.

3.2 New and Re-derived RV Measurements Using Spectral Fitting

We presented new radial velocity measurements from spectra with NIRC2, OSIRIS, NIFS, and IRCS instruments. While the RV measurements from NIRC2, OSIRIS, and IRCS taken before 2017 were presented previously in Ghez et al. (2008); Boehle et al. (2016); Nishiyama et al. (2018), here we re-derived all NIRC2, OSIRIS, and IRCS RVs using an improved method. We used a synthetic spectral grid and Bayesian inference to model the spectra using a physical model that includes the physical properties of the star (e.g. effective temperature) along with its rotational velocity and radial velocity. We used the BOSZ spectral grid (Bohlin et al. 2017) which has synthetic spectra calculated over the range of wavelength of the observations as well as the reported physical properties of S0-2. This grid reaches high effective temperatures (up to 35,000 K),

which covers previously reported temperatures for S0-2 and other stars within 0.04 pc of the SMBH (Habibi et al. 2017). We used the StarKit spectral fitting software package to perform the parameter estimation (Kerzendorf & Do 2015). StarKit simultaneously models the physical properties of the star (effective temperature, surface gravity, metallicity, alpha-elemental abundance), the continuum (modeled as a second-order polynomial), rotational velocity, radial velocity, instrumental broadening, and wavelength sampling in order to compare the model with the data directly. An example fit for the star main-sequence B-star HD172488 is shown in Figure 3.1. We used a Gaussian likelihood to compare the model to the observed spectrum and the uncertainty on the flux. The flux uncertainty was estimated using the standard deviation of the flux in the continuum of the star. To account for potential mis-estimation of the flux uncertainties, we also included an additive flux uncertainties term in the spectroscopic fit. We find that this additive term is smaller than the flux uncertainties. Parameter estimation is done via Bayesian inference with sampling of the posterior using the nested-sampling algorithm MultiNest (Feroz et al. 2009, 2013). More details on StarKit and its application to Galactic center data are given in Do et al. (2015, 2018); Feldmeier-Krause et al. (2017). We find that our new method of measuring the RV of S0-2 is more precise than the method used previously to extract S0-2's RV (Ghez et al. 2008; Gillessen et al. 2017; Chu et al. 2018, Figure 3.2).

Previously, a Gaussian profile was fitted to the hydrogen Brγ absorption line at 2.1661 micron, the strongest spectral feature in the K-band. While a Gaussian fit can determine the centroid of the line, at high SNR ratio, the intrinsic line shape becomes more important, thus limiting the precision of a Gaussian fit. In addition, there is a weak helium line at 2.1617 micron, which is not well resolved from the hydrogen line, resulting in an asymmetric line profile, potentially biasing the Gaussian fit. By modeling the spectrum with a physically motivated model with the appropriate atomic line data, we use more information than with a Gaussian fit alone resulting in more precise measurements, as seen in Figure 3.1. The radial velocity measurements using StarKit have an average uncertainty of 17 km s^{-1} compared to about 30 km s^{-1} with the Gaussian fit,

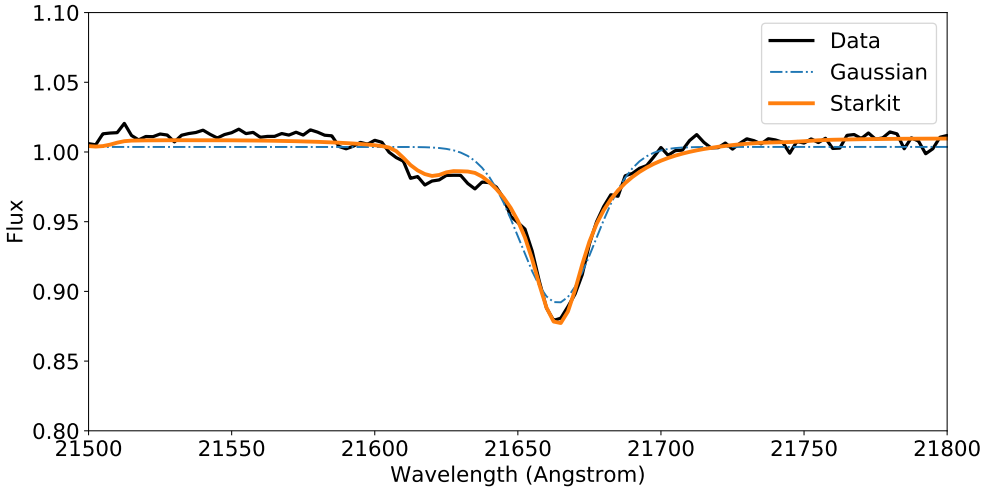

Figure 3.1: A comparison between fitting the star HD172488's Brγ absorption line using StarKit (orange) and with a Gaussian profile (blue). StarKit does a better job fitting the true shape of the absorption line and accounts for the nearby He absorption lines near Brγ .

an improvement of a factor of 1.7 (Figure 3.2).

3.3 Observing RV Standard Stars for Evaluating StarKit Method

Using observations of stars that are RV standards on the same night as observations of S0-2, we can also evaluate the accuracy of the radial velocity measurements. We selected radial velocity standards to be stars that have spectral type similar to that of S0-2 and which have been previously observed as radial velocity standards. We extract these stars using the Set of Identifications, Measurements and Bibliography for Astronomical Data (SIMBAD) database, selecting ones that do not have significant variations in radial velocities between multiple previous measurements. Measurements of these stars are included in Table 3.1.

When the Gaussian fitting method was used, the weighted average difference from the reported SIMBAD values was 8.3 $\pm$ 1.2 km s^{-1}, but when using StarKit, radial velocity measurements of the standard stars had a weighted average difference from the reported SIMBAD velocities of only 1.3 $\pm$ 1.2 km s^{-1} (Fig. 3.3). We attribute this

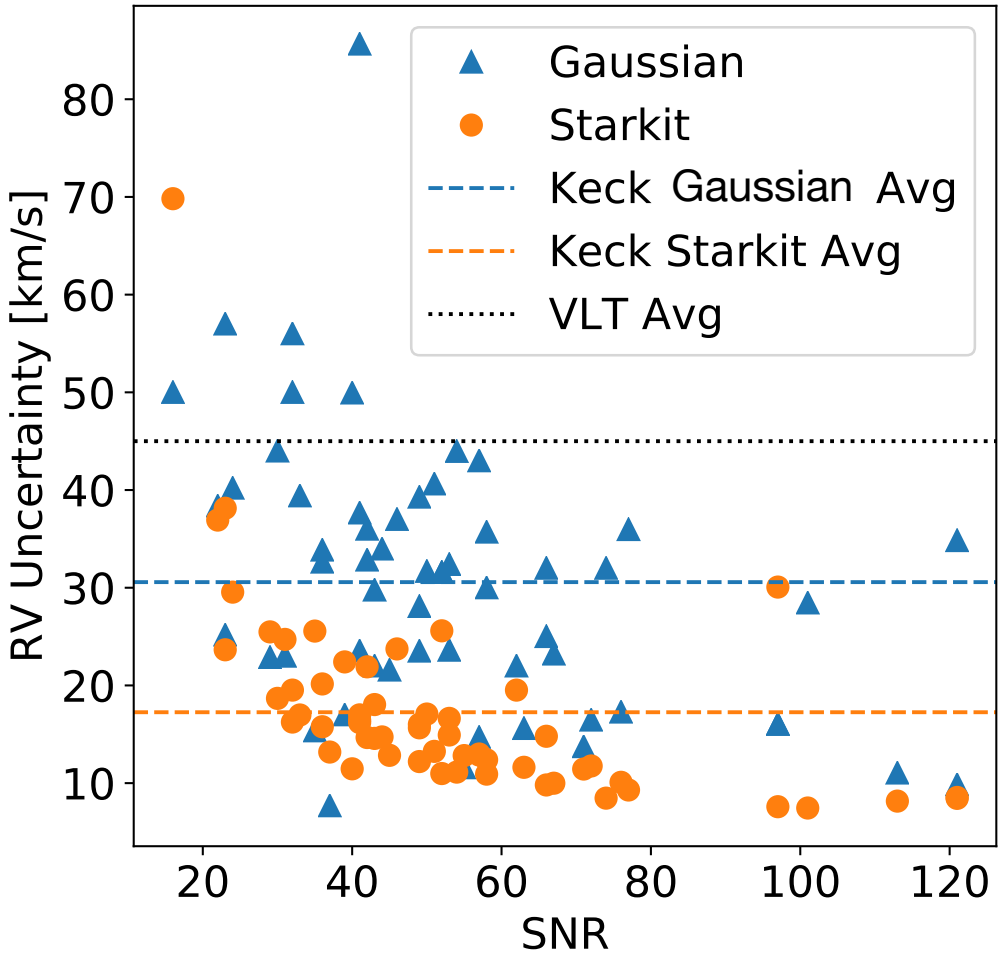

Figure 3.2: Comparisons of the RV uncertainty for S0-2 RV measured using a Gaussian fit to the Bracket Gamma line (blue triangles) and using the full-spectrum fitter StarKit (orange circles). RV uncertainties are shown as a function of SNR. On average, StarKit uncertainty estimates are about 1.7 times more precise than using a Gaussian. These measurements are also on average about 2.2 times more precise than average RV values reported by Gillessen et al. (2017) using SINFONI on VLT.

improvement to StarKit's ability to fit the non-Gaussian absorption lines. This result shows the robustness of the StarKit method and a reduction in systematic uncertainty.

Table 3.1. RV Standard Star Measurements

Date	Star	Filter	Gaussian RV (km s^{-1})	StarKit RV (km s^{-1})	SIMBAD RV (km s^{-1})	Gaussian Offset (km s^{-1})	Starkit Offset (km s^{-1})	SIMBAD Reference [a]
2015-08-07	HD 217811	Kn3	-30.7±8.4	-19.8±6.7	-11.3±2.7	-19.4	-8.5	1
2016-05-15	HD 172488	Kbb	43.1±6.4	42.8±5.2	29.1±3.6	14.0	13.7	1,2
2016-05-16	HD 172488	Kbb	41.3±7.3	36.8±5.3	29.1±3.6	12.2	7.7	1,2
2016-07-11	HD 172488	Kbb	37.1±4.3	31.2±4.6	29.1±3.6	8.0	2.1	1,2
2016-07-12	HD 172488	Kbb	34.0±4.3	32.5±4.4	29.1±3.6	4.9	3.4	1,2
2017-05-17	HD 172488	Kn3	36.0±3.6	27.7±5.1	29.1±3.6	6.9	-1.4	1,2
2017-08-14	HD 217811	Kn3	-0.2±6.8	-8.0±4.5	-11.3±2.7	11.1	3.3	1
2017-08-14	HD 215191	Kbb	1.0±6.5	-17.5±6.8	-14.3±2.5	15.3	-3.2	1,3
2017-08-14	HD 215191	Kn3	7.3±13.1	-14.8±6.9	-14.3±2.5	21.6	-0.5	1,3
2017-08-14	HD 191639	Kbb	-0.8±9.4	-11.2±6.4	-7.0±4.3	6.2	-4.2	1
2017-08-14	HD 191639	Kn3	0.1±6.3	-15.8±8.0	-7.0±4.3	7.1	-8.8	1

Table 3.1 (cont'd)

Date	Star	Filter	Gaussian RV (km s^{-1})	StarKit RV (km s^{-1})	SIMBAD RV (km s^{-1})	Gaussian Offset (km s^{-1})	Starkit Offset (km s^{-1})	SIMBAD Reference [a]
2017-08-14	HD 217811	Kbb	4.4±5.0	-6.5±4.3	-11.3±2.7	15.7	4.8	1
2017-09-02	HD 217811	Kn3	6.0±10.6	-2.1±6.1	-11.3±2.7	17.3	9.2	1
2017-09-02	HD 214652	Kbb	-5.3±4.7	-15.4±6.1	-11.9±4.4	6.6	-3.5	1
2017-09-02	HD 214652	Kn3	8.0±14.8	-8.6±8.4	-11.9±4.4	20.0	3.3	1
2017-09-02	HD 186568	Kbb	-6.0±2.8	-7.0±3.6	-9.2±1.0	3.2	2.2	1,5
2017-09-02	HD 186568	Kn3	1.9±3.6	-7.0±4.3	-9.2±1.0	11.1	2.2	1,5
2017-09-02	HD 217811	Kbb	-2.2±7.7	-6.2±5.2	-11.3±2.7	9.1	5.1	1
2018-04-27	HD 172488	Kn3	35.0±5.1	25.6±6.3	29.1±3.6	5.9	-3.5	1,2
2018-04-27	HD 170783	Kn3	-3.4±3.0	-7.7±5.1	-4.4±0.3	1.0	-3.3	1
2018-04-27	HD 146416	Kbb	27.8±7.3	-10.5±10.9	-9.0±4.9	36.8	-1.5	1
2018-04-27	HD 146416	Kn3	36.5±4.7	0.8±9.4	-9.0±4.9	45.5	9.8	1

Table 3.1 (cont'd)

Date	Star	Filter	Gaussian RV (km s^{-1})	StarKit RV (km s^{-1})	SIMBAD RV (km s^{-1})	Gaussian Offset (km s^{-1})	Starkit Offset (km s^{-1})	SIMBAD Reference [a]
2018-05-23	HD 172488	Kn3	39.5±6.4	29.7±5.7	29.1±3.6	10.4	0.6	1,2
2018-06-05	HD 172488	Kn3	29.2±9.9	31.9±5.6	29.1±3.6	0.0	2.8	1,2
2018-06-05	HD 164900	Kbb	16.2±7.4	-11.7±8.5	-36.0±3.7	52.2	24.3	4
2018-06-05	HD 164900	Kn3	23.2±10.9	-8.0±7.0	-36.0±3.7	59.2	28.0	4
2018-07-22	HD 172488	Kn3	36.2±5.9	29.5±5.1	29.1±3.6	7.1	0.4	1,2
2018-07-31	HD 172488	Kn3	31.4±10.2	24.7±5.4	29.1±3.6	2.3	-4.4	1,2
2018-08-11	HD 172488	Kn3	27.8±10.8	25.5±5.7	29.1±3.6	-1.3	-3.6	1,2
2018-08-11	HD 217811	Kn3	2.1±6.7	-11.7±4.9	-11.3±2.7	13.4	-0.4	1

[a]Measurement reported in (1) Gontcharov (2006), (2) Bobylev (2008), (3) Huang et al. (2010), (4) Kharchenko et al. (2007), (5) Khalack & LeBlanc (2015).

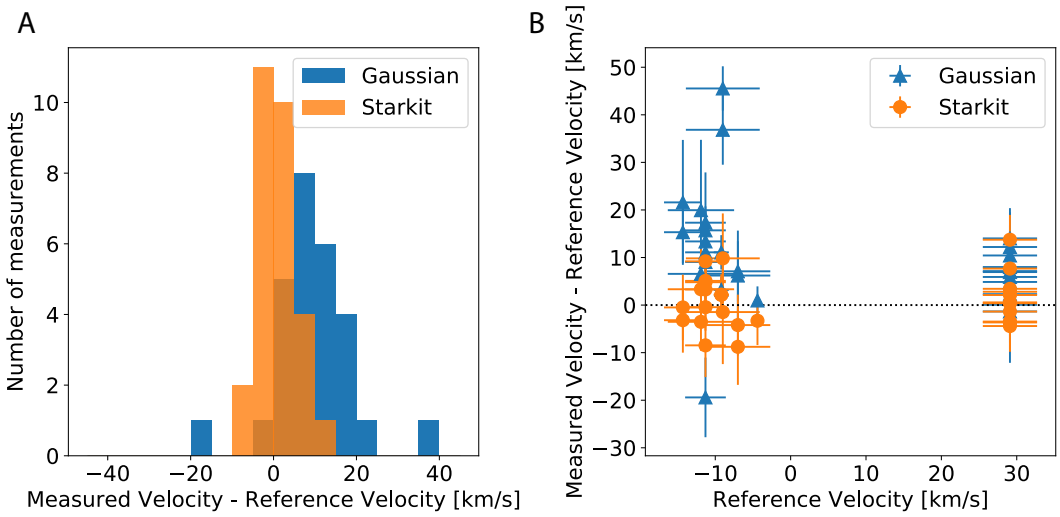

Figure 3.3: Left: Histogram of the differences between radial velocity measurements and reference values of standard stars given in Table 3.1. Right: Differences between radial velocity measurements and reference values compared to their reference velocity for each individual measurement.

3.4 Conclusion

Our improved radial velocity measurement method met our objectives of improving our precision of our measurements and reduced measurement bias. We improved our measurement uncertainties by a factor of 1.7 for S0-2. Additionally, our RV measurements of RV standard stars are completely consistent with their literature values. These improvements lead to greater confidence and robustness in our detection of the relativistic redshift of Do et al. (2019).

While this work was primarily motivated by S0-2's relativistic redshift, it also has great implications in searching for spectroscopic binaries. Our improvements in RV precision makes us more sensitive to spectroscopic binaries, since we are interested in RV changes over time. Our reduced bias also gives us greater confidence trusting our RV curves, since these RV standard stars match the spectral types of the young stars at the Galactic center. Searching for binaries beyond S0-2 will benefit greatly from these RV improvements.

CHAPTER 4

Search for Spectroscopic Binaries at the Galactic Center

To be submitted to the Astrophysical Journal

The formation mechanism of the young S-stars located within an arcsecond of the central supermassive black hole remains a mystery. While binaries are important for understanding the young star cluster at the Galactic center, there have been limited surveys for binaries in the region. We present a systematic search for spectroscopic binaries at the Galactic Center. With over two decades of integral field spectroscopy data, advanced tools for fitting mid-infrared stellar spectra, and 1000 radial velocity data points, we conduct a spectroscopic binary search of 29 stars at the Galactic center. After subtracting a star's motion around the supermassive black hole, we search for a periodic signal using a Lomb-Scargle analysis and fitting the residual radial velocity curve to a binary system radial velocity curve. We find no significant periodic detections in our sample, suggesting there are no binaries among the S-stars. We also place limits on the hypothetical companion masses of these S-stars. We also place a limit on the intrinsic fraction of these stars at 42%, which disagrees with the binary fraction for massive field stars. These results favor formation mechanisms that result in the young S-stars being single stars.

4.1 Introduction

The 'S-stars" are one of the most intriguing star populations at the Galactic center. Their orbits have proved the existence of a supermassive black hole (SMBH) with a mass of 4×10^6 $M_\odot$ (Ghez et al. 2008; Gillessen et al. 2009a, 2017) and their motions

have exhibited post-Newtonian effects (e.g. Gravity Collaboration et al. 2018; Do et al. 2019, and references therein). Spectroscopic observations have also revealed that most of these stars are main-sequence B stars (Ghez et al. 2003; Eisenhauer et al. 2005; Habibi et al. 2017). This property suggests that they have formed about 6 Myr ago. This property raises questions about their formation mechanism, since traditional star formation would be disrupted by the tidal forces of the black hole (Morris 1993).

Numerous investigations have been done to postulate the formation of these S-stars. General mechanisms include: (1) binary star systems scattered from outside the region and then tidally disrupted, leaving behind one component of the original binary while the other is ejected as a hypervelocity star (Hills 1988; Perets et al. 2007), (2) S-stars formed in the clockwise disk located just outside 1 arcsec of the SMBH and then migrated to the SMBH (Levin 2007; Löckmann et al. 2008; Merritt et al. 2009), and (3) merger of binary stars at the Galactic centers caused by the Kozai-Lidov mechanism, with the product appearing as a main-sequence B-star (Witzel et al. 2014; Stephan et al. 2016; Ciurlo et al. 2020).

Binary stars provide crucial roles in these formation mechanisms, and the discovery of binary stars amongst the S-stars may attest to particular formation mechanisms. Additionally, massive stars in the field have high multiplicity fractions (Sana et al. 2012; Duchêne & Kraus 2013), so it is reasonable to expect these main-sequence B-stars at least started out in multiple systems. Previous studies have identified 3 binary systems (Ott et al. 1999; Martins et al. 2006; Rafelski et al. 2007; Pfuhl et al. 2014; Gautam et al. 2019), but none amongst the S-stars. Chu et al. (2018) performed the first spectroscopic search for binaries amongst the S-stars and focused on the well-studied star S0-2 (also known as S2). Through radial velocity monitoring, Chu et al. (2018) did not find significant evidence for S0-2 being a binary and placed a hypothetical companion mass below current detection limits.

With nearly two decades of spectroscopic measurements, there is an opportunity to expand the search for spectroscopic binaries to the rest of the S-star cluster. Chu et al.

(2018) established a framework for searching for spectroscopic binaries of S-star in radial velocity data. Improvements to tools for fitting mid-infrared stellar spectra (1.9-2.3 μm, Kerzendorf & Do 2015; Bohlin et al. 2017) and better understanding of radial velocity measurement systematics (Do et al. 2019) have also improved our sensitivity to other spectroscopic binaries.

4.2 Observations and Data

4.2.1 Spectroscopy Data

Spectroscopic observations taken with the OSIRIS spectrograph (Larkin et al. 2006) on the W. M. Keck Telescope using the laser-guide-star adaptive optics system (LGS AO) (Wizinowich et al. 2006; van Dam et al. 2006) are reported in Do et al. (2019) and references therein. The data were taken using the Kn3 (2.121 – 2.229 μm) and Kbb (1.965 – 2.381 μm) filters, which cover the Brγ absorption line ($\lambda = 2.166$ μm) for the young stars. These data have been reduced with the latest version of the OSIRIS data reduction pipeline (Lyke et al. 2017; Lockhart et al. 2019) to make the data cubes. Blank skies and telluric standard stars were also observed during the night to correct for sky and atmospheric lines. Further details on these processes can be found in Do et al. (2013). A summary of the Keck observations is reported in Table 4.1. We also include data taken with the NIFS instrument on Gemini North and IRCS on the Subaru Telescope. These observations are also reported in Do et al. (2019) and references therein.

Table 4.1. Summary of Keck Spectroscopic Observations

Date			$N_{\text{frames}} \times t_{\text{int}}$	FWHM [a]	Filter	Scale
(UT)	(MJD)	(Epoch)	(s)	(mas)		(mas)
2000-06-23	51718.50	2000.476	36×300		K [b]	18
2002-06-02	52427.50	2002.418	7×1200		K [c]	20
2002-06-03	52428.50	2002.420	4×1200		K' [c]	20
2003-06-08	52798.50	2003.433	2×1200		K' [c]	20
2004-06-23	53179.50	2004.476	16×1200		K' [c]	20
2005-05-30	53520.50	2005.410	7×1200		K' [c]	20
2005-07-03	53554.50	2005.503	7×900	58	Kbb	20
2006-05-23	53878.50	2006.390	4×900	74	Kbb	35
2006-06-18	53904.50	2006.461	9×900	65	Kn3	35
2006-06-30	53916.50	2006.494	9×900	59	Kn3	35
2006-07-01	53917.50	2006.497	9×900	64	Kn3	35
2007-05-21	54241.50	2007.384	2×900	86	Kn3	35
2007-07-19	54300.29	2007.545	2×900	56	Kn3	35
2008-05-16	54602.50	2008.372	11×900	57	Kn3	35
2008-07-25	54672.28	2008.563	9×900	60	Kn3	35
2009-05-05	54956.50	2009.342	7×900	60	Kn3	35
2009-05-06	54957.50	2009.344	12×900	69	Kn3	35
2010-05-05	55321.50	2010.341	6×900	67	Kn3	35
2010-05-08	55324.50	2010.349	11×900	69	Kn3	35
2011-07-10	55752.33	2011.520	6×900	71	Kn3	35

Table 4.1 (cont'd)

Date			$N_{\text{frames}} \times t_{\text{int}}$	FWHM [a]	Filter	Scale
(UT)	(MJD)	(Epoch)	(s)	(mas)		(mas)
2012-06-08	56086.50	2012.435	4×900	87	Kn3	35
2012-06-09	56087.50	2012.438	3×900	66	Kn3	35
2012-06-11	56089.50	2012.444	7×900	64	Kn3	20
2012-07-21	56129.31	2012.553	3×900	77	Kn3	35
2012-07-22	56130.31	2012.555	7×900	81	Kn3	35
2012-08-12	56151.33	2012.613	6×900	56	Kn3	35
2012-08-13	56152.27	2012.615	7×900	99	Kn3	35
2013-05-11	56423.50	2013.358	11×900	73	Kbb	35
2013-05-12	56424.50	2013.361	11×900	62	Kbb	35
2013-05-13	56425.50	2013.363	12×900	61	Kbb	35
2013-05-14	56426.50	2013.366	11×900	61	Kn3	35
2013-05-16	56428.50	2013.372	7×900	98	Kn3	20
2013-05-17	56429.50	2013.374	7×900	64	Kn3	20
2013-07-25	56498.33	2013.563	11×900	79	Kn3	35
2013-07-26	56499.34	2013.566	6×900	73	Kn3	35
2013-07-27	56500.33	2013.568	11×900	66	Kn3	35
2013-08-10	56514.29	2013.607	7×900	62	Kn3	35
2013-08-11	56515.31	2013.609	9×900	69	Kn3	35
2013-08-13	56517.29	2013.615	12×900	67	Kn3	35
2014-05-18	56795.50	2014.376	13×900	66	Kn3	35

Table 4.1 (cont'd)

Date			$N_{\text{frames}} \times t_{\text{int}}$	FWHM [a]	Filter	Scale
(UT)	(MJD)	(Epoch)	(s)	(mas)		(mas)
2014-05-23	56800.50	2014.390	10×900	76	Kn3	35
2014-07-03	56841.36	2014.502	8×900	66	Kn3	35
2015-05-04	57146.50	2015.337	5×900	68	Kn3	35
2015-07-21	57224.35	2015.551	5×900	56	Kn3	35
2016-05-14	57522.50	2016.367	8×900	78	Kbb	35
2016-05-15	57523.50	2016.370	4×900	80	Kbb	35
2016-05-16	57524.50	2016.372	8×900	84	Kbb	35
2017-05-17	57890.52	2017.374	11×900	73	Kn3	35
2017-05-18	57891.51	2017.377	9×900	94	Kn3	35
2017-05-19	57892.50	2017.379	6×900	86	Kn3	35
2017-07-19	57953.33	2017.546	12×900	77	Kn3	35
2017-07-27	57961.32	2017.568	13×900	89	Kn3	35
2017-08-14	57979.28	2017.617	8×900	75	Kn3	35
2017-09-02	57998.25	2017.669	4×900	77	Kn3	35
2018-03-17	58194.64	2018.207	2×900	70	Kn3	35
2018-04-24	58232.57	2018.310	7×900	73	Kn3	35
2018-05-17	58255.56	2018.373	4×900	205	Kn3	50
2018-05-23	58261.50	2018.390	14×900	91	Kn3	35
2018-06-05	58274.47	2018.425	10×900	108	Kn3	35
2018-07-22	58321.33	2018.554	11×900	77	Kn3	35

Table 4.1 (cont'd)

Date			$N_{\text{frames}} \times t_{\text{int}}$	FWHM [a]	Filter	Scale
(UT)	(MJD)	(Epoch)	(s)	(mas)		(mas)
2018-07-31	58330.32	2018.578	11×900	73	Kn3	35
2018-08-11	58341.31	2018.608	9×900	79	Kn3	35
2018-08-31	58361.27	2018.663	3×900	88	Kn3	35

[a]Average FWHM of S0-2 in the mosaic made of all frames, measured by fitting a two-dimensional Gaussian to the source.

[b]Taken with NIRSPEC slit spectrograph

[c]Taken with NIRC2 slit spectrograph

4.2.2 Extracting Radial Velocities

Previous papers from the UCLA GCG reported the radial velocities of S0-2 and S0-38. In this work, we also extracted the radial velocities of other S-stars located in the central pointing. The methods and calibrations used to measure radial velocities are reported in Do et al. (2019).

To summarize, a star's spectrum is extracted from the individual data cubes from a given epoch using a circular aperture, with an annulus around the star to estimate the sky background. The spectra are then averaged into a combined spectrum. The star's combined spectrum is then modeled using the Bayesian inference tool *Starkit* (Kerzendorf & Do 2015) and compared to spectra in the BOSZ spectral grid (Bohlin et al. 2017). We derive the radial velocity and its uncertainty using the median and 1 sigma central credible interval of the marginalized posterior. This radial velocity is then corrected for the local standard of rest with respect to the Galactic center[1]. Do et al. (2019) showed that this technique of spectral fitting reduced uncertainties and

[1]We use the IRAF procedure *rvcorrect*. This correction uses a velocity of 20 km s^{-1} for the solar motion with respect to the local standard of rest in the direction $\alpha = 18^h, \delta = +30\,\text{deg}$ for epoch 1900 Kerr & Lynden-Bell (1986), corresponding to $(u, v, w) = (10, 15.4, 7.8)$ km s^{-1}.

systematic bias compared to fitting a Gaussian to the Brγ line for the star S0-2.

We apply this same technique to all the other stars in the OSIRIS data when a star's radial velocity can be measured. The number and quality of radial velocity measurements extracted for each epoch depends greatly on a number of factors, such as weather conditions, adaptive optics performance, and position in the OSIRIS dither pattern. Stellar crowding and confusion can also lead to difficulties when extracting a radial velocity measurement. Even though a star may be identified in an OSIRIS cube, its spectrum may not be of adequate quality to measure its radial velocity. We perform a quality inspection of the extracted spectra to ensure their radial velocities can be measured.

4.2.3 Imaging and Astrometric Data

Information about the imaging observations taken with the NIRC2 instrument (Matthews & Soifer 1994) on the Keck Telescope are described in depth in Do et al. (2019), and references therein. Jia et al. (2019) and Gautam et al. (2019) describe in depth the processes used to determine the stars' astrometric positions and photometric magnitudes. Jia et al. (2019) also detail the process of deriving the stellar positions for each epoch and aligning them to a common reference frame reported in Sakai et al. (2019).

4.2.4 Sample Selection

Chu et al. (2018) investigated the star S0-2 as a binary star due to its precise radial velocity measurements, well known orbit, and to quantify the potential bias a spectroscopic binary would have on the relativistic redshift measured by Do et al. (2019); Gravity Collaboration et al. (2018). This work expands this investigation to 29 stars in a systematic way. The investigation of S0-2's relativistic redshift required plentiful observations (Do et al. 2019; Hees et al. 2019) and add increased sensitivity to radial velocity variations for the other stars close to the SMBH.

The broadest criterion of the star sample is that the star must be located within the

OSIRIS Kn3 35 mas central pointing, which has been described in numerous works such as Boehle et al. (2016); Chu et al. (2018); Do et al. (2019). The primary objective of this configuration was to monitor the star S0-2, and it places S0-2 at the center of the dither pattern. The OSIRIS field of view contains additional stars around S0-2, and we include these additional stars in our search.

Because we are focused on adequately sampling the parameter space of periods on the order of a few days, we do not combine measurements taken over multiple nights. Stars with $K' > 16$ magnitude do not achieve adequate signal-to-noise to measure their radial velocities for a single night (usually a half-night). Therefore, we only consider stars with $K' < 16$ mag. This creates an intermediate sample of 64 stars. Additionally, we do not include the 2 Wolf-Rayet emission line sources that are located in the central pointing (IRS16C and IRS16SW). We omit them because measuring their radial velocities is complicated due to their stellar winds. We also do not include 7 stars that do not possess absorption lines in Kn3, since we cannot measure their radial velocities. These particular stars are consistent of main-sequence O stars. We also omit stars confused in image and/or spectral space, meaning we cannot distinguish their spectra and therefore their radial velocities.

In order to obtain meaningful results from a periodicity search, we needed to ensure that we had enough radial velocity points for a given star. The number of radial velocities for a given star may vary as described in Section 4.2.2. We make a final cut where stars must have at least 3 radial velocity points. This next cut leads to 30 stars, with 18 early-type stars and 12 late-type stars listed in Table 4.2. We note here that after further investigation into systematic effects, the young star S1-2's radial velocity measurements were negatively impacted by the background gas in the region, and we exclude it from further analysis. The final sample for our binary search consists of 29 stars. Figure 4.1 shows the sample of stars for the following analysis. It also shows examples of stars with $K' < 16$ that are omitted because they are emission line sources, featureless in Kn3, or confused with other sources. Stars are classified as early-type if they exhibit Brγ absorption, which is consistent of main-sequence B-stars. Stars are classified as

late-type if they possess absorption lines consistent with red giants, primarily Na I and CO (Do et al. 2013). We also include radial velocities from Gillessen et al. (2017) for stars that overlap with their sample.

We report the radial velocities for these stars in Section A.3.

Table 4.2. S-star Sample

Star	K' (mag)	Spectral Type	RAΔ [a] ($''$)	DecΔ [a] ($''$)	RV Points	[RV σ] (km s^{-1})	RV Baseline (Years)	Astrometry Accel.	RV Accel.	RV Fit Poly.	Orbit Fit
S0-1	14.7	Early	0.04	-0.26	51	54	15	Yes	Yes	2	Yes
S0-2	14.0	Early	-0.01	0.17	115	23	18	Yes	Yes	2+	Yes
S0-3	14.5	Early	0.34	0.12	59	37	14	Yes	Yes	1	Yes
S0-4	14.1	Early	0.45	-0.33	52	46	15	Yes	Yes	1	Yes
S0-5	15.0	Early	0.17	-0.36	42	61	14	Yes	Yes	2	Yes
S0-7	15.1	Early	0.51	0.10	23	30	12	No	No	0	No
S0-8	15.8	Early	-0.23	0.16	45	95	14	Yes	Yes	2	Yes
S0-9	14.2	Early	0.22	-0.60	33	36	13	No	No	0	No
S0-11	15.1	Early	0.49	-0.06	28	32	12	No	No	0	No
S0-14	13.5	Early	-0.76	-0.28	41	18	12	No	No	0	No
S0-15	13.5	Early	-0.97	0.18	31	32	12	No	No	0	No
S0-16	15.3	Early	0.23	0.17	24	76	14	No	No	2	Yes
S0-19	15.3	Early	-0.08	0.40	39	118	15	Yes	Yes	2	Yes
S0-20	15.8	Early	0.05	0.14	33	195	14	Yes	Yes	2	Yes
S0-31	14.9	Early	0.57	0.45	9	41	11	No	No	0	No
S1-2 [b]	14.6	Early	0.08	-1.02	17	39	12	No	Yes	1	No

Table 4.2 (cont'd)

Star	K' (mag)	Spectral Type	RAΔ [a] ($''$)	DecΔ [a] ($''$)	RV Points	[RV σ] (km s^{-1})	RV Baseline (Years)	Astrometry Accel.	RV Accel.	RV Fit Poly.	Orbit Fit
S1-8	14.0	Early	-0.58	-0.92	16	33	11	Yes	No	0	No
S1-33	14.9	Early	-1.25	-0.01	15	32	12	No	No	0	No
S0-6	14.0	Late	0.02	-0.36	47	3	13	No	Yes	1	No
S0-12	14.3	Late	-0.55	0.41	48	3	12	No	No	0	No
S0-13	13.2	Late	0.56	-0.41	48	3	12	No	No	0	No
S0-17	15.9	Late	0.05	0.008	44	90	15	Yes	Yes	1	Yes
S0-18	14.9	Late	-0.12	-0.42	18	4	12	No	No	0	No
S0-27	15.5	Late	0.15	0.55	19	7	12	No	No	0	No
S1-5	12.4	Late	0.32	-0.89	27	3	12	No	No	0	No
S1-6	15.4	Late	-0.96	0.74	19	8	10	No	No	0	No
S1-10	14.7	Late	-1.10	-0.02	22	5	12	No	No	0	No
S1-13	14.0	Late	-1.14	-0.97	7	5	12	No	No	0	No
S1-15	14.0	Late	-1.36	0.49	23	4	11	No	No	0	No
S1-31	15.6	Late	-0.99	0.54	16	8	11	No	No	0	No

[a]From Sgr A*.

[b]RV extraction is affected by background gas and is excluded from further analysis.

4.3 Periodicity Search

The following section describes the process for detecting periodic signals in the radial velocity data. First, we describe the methods used for fitting the stellar radial velocity curves to produce residual curves. These residual curves are then run through two types of periodicity searches: a Lomb-Scargle analysis (Lomb 1976; Scargle 1982; VanderPlas 2018) and a Bayesian fit for potential binary systems. A similar methodology was done for the star S0-2 in Chu et al. (2018). The Lomb-Scargle analysis provides a computationally efficient method for detecting periodic signals in unevenly spaced data. The Bayesian fitting method provides a more complete and robust approach and allows us to derive upper limits on the orbital parameters of hypothetical binary companions to these S-stars.

4.3.1 Producing Residual Radial Velocity Curves

The stars in this sample have visible motions due to their proximity to the SMBH. We are interested in studying their intrinsic motion to search for a potential periodic signal, which may be evidence for a spectroscopic binary. Therefore, we need to subtract their motion around the SMBH before conducting a periodic search. The methodology for subtracting out this motion depends on the star.

We began by determining which stars have significant accelerations in both radial velocity and astrometry. To determine significant accelerations along the line of sight, we performed a polynomial fit to the stars' radial velocities. The degree of the polynomial fit is determined by the F-test, where a higher degree polynomial must pass the F-test of the lower degree polynomial with a 95% significance. Accelerations in astrometry were determined using the same methodology as listed in Jia et al. (2019). The determination of accelerations and polynomial degree of the radial velocity fits are reported in Table 4.2. The sample of stars were then divided into two subsets:

1. Polynomial Stars

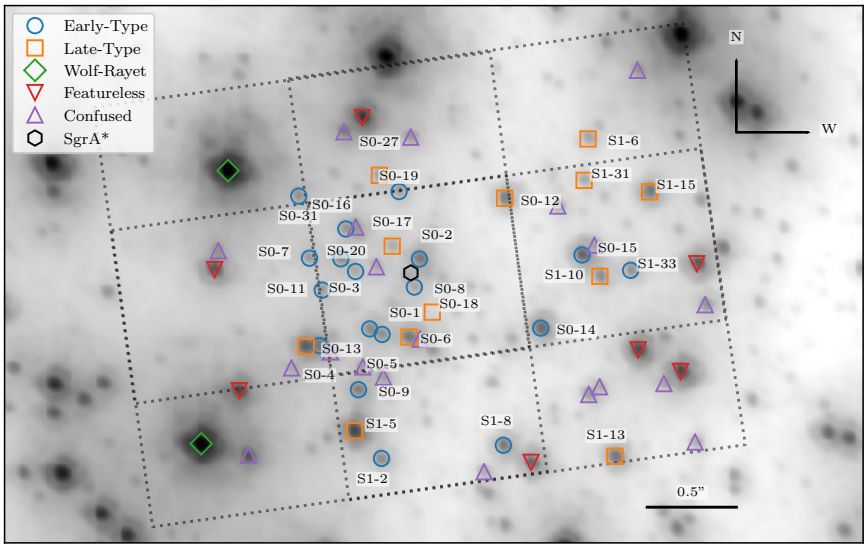

Figure 4.1: Stars that are included in the periodicity search, classified by spectral type. The GCG OSIRIS dither pattern overlayed on a NIRC2 image. These stars are located in the central pointing dither pattern. The central square is covered by all dither points, meaning more spectra are taken of these stars throughout the night. Stars brighter than $K = 16$ mag not included in this radial velocity sample because they are identified as Wolf-Rayet stars, lack absorption lines, or are confused with other stars are marked in green diamonds, red down triangles, or purple up triangles, respectively.

2. Orbit Stars

For stars in subset 1, we use the favored polynomial fit to their radial velocities to account for their motion around the SMBH. We take the fit and subtract it from the data to produce a residual radial velocity curve. An example of a star fit with a polynomial, S0-14, is shown in Figure 4.2. The favored polynomial fits for each star in the polynomial sample are reported in Table 4.3. Ultimately, 20 out of the 29 stars are part of the polynomial star, with only one star (S0-6) favoring a constant acceleration fit (1st order polynomial). The remaining 18 stars favor a constant velocity fit (0th order polynomial).

Table 4.3. Polynomial Fit Results

Star	t_0 (Epoch)	a_z (km s^{-1}yr^{-1})	$a_z\sigma$ (km s^{-1}yr^{-1})	v_{z0} (km s^{-1})	$v_{z0}\sigma$ (km s^{-1})	χ^2_{red}
S0-7	2006.4942			105.3	5.9	3.3
S0-9	2005.5031			114.5	4.8	2.08
S0-11	2006.4942			-22.2	4.6	1.5
S0-14	2006.4613			-31.3	2.8	1.03
S0-15	2006.4613			-552.5	4.82	2.85
S0-31	2006.4969			-118.9	10.6	1.74
S1-8	2006.4613			-112	7.2	1.92
S1-33	2006.4613			26.3	7.0	0.83
S0-6	2005.5031	0.8	0.1	83.1	1.1	1.65
S0-12	2006.4613			-39.3	0.4	2.01
S0-13	2006.4613			-45.1	0.4	2.19
S0-18	2006.4942			-289.3	1.0	3.52

Table 4.3 (cont'd)

Star	t_0 (Epoch)	a_z (km s^{-1}yr^{-1})	$a_z\sigma$ (km s^{-1}yr^{-1})	v_{z0} (km s^{-1})	$v_{z0}\sigma$ (km s^{-1})	χ^2_{red}
S0-27	2006.4613			-121.2	1.5	4.3
S1-5	2006.4613			11.2	0.5	1.9
S1-6	2007.5422			-42.0	1.5	1.1
S1-10	2006.4613			-33.6	1.0	1.37
S1-13	2006.4942			-749.1	1.6	6.8
S1-15	2006.4613			-120.4	0.82	2.12
S1-31	2007.5422			182.9	1.6	1.92

Stars in subset 2 have significant accelerations in both astrometry and radial velocity due to their orbits around the SMBH. They have also been monitored for years and have had their orbits previously reported (e.g. Gillessen et al. 2009b, 2017). For these 10 stars, we perform an orbital fit of their motion around the SMBH to create an orbital model of their radial velocities. In this method, we performed a more robust fit to their radial velocities compared to a polynomial model. Stars in subset 1 do not possess enough kinematic information to constrain their orbital parameters, which is why their radial velocities are fit with a polynomial instead.

Orbit stars have their motions fit in the same way as described in works such as Do et al. (2019), and we use the orbital solution reported in Do et al. (2019) for S0-2. For stars other than S0-2, we make a few changes. We still fit these stars with Newtonian plus relativistic redshift model, which also accounts for the Romer time delay. These stars are not expected to show observable relativistic redshift effects, so we fix the relativistic redshift parameter to be true.

We fit each star in a uniform way. We fix the black hole parameters (mass, distance, position, and velocity) to the values reported in Do et al. (2019), which come from the S0-2 orbital fit. S0-2 has the greatest orbital phase coverage of this sample and provides strong constraints on these black hole parameters. Additionally, leaving the black hole parameters free did not have a significant effect on the radial velocity models of these stars. While interesting, investigating the black hole and resulting orbital parameters favored by these stars are beyond the scope of this work. We do not fit for an offset and additive error between Keck and VLT data points. Finally, we fix an astrometric correlation length of 20 mas (which comes from S0-2) and fit for a mixing parameter. Details for this orbital fitting methodology are described in more detail in Section A.4.

Once the star's orbital fit is performed, a model for its radial velocity is generated and subtracted to create a residual. An example of a star's radial velocity data, orbital model, and residual are shown in Figure 4.3.

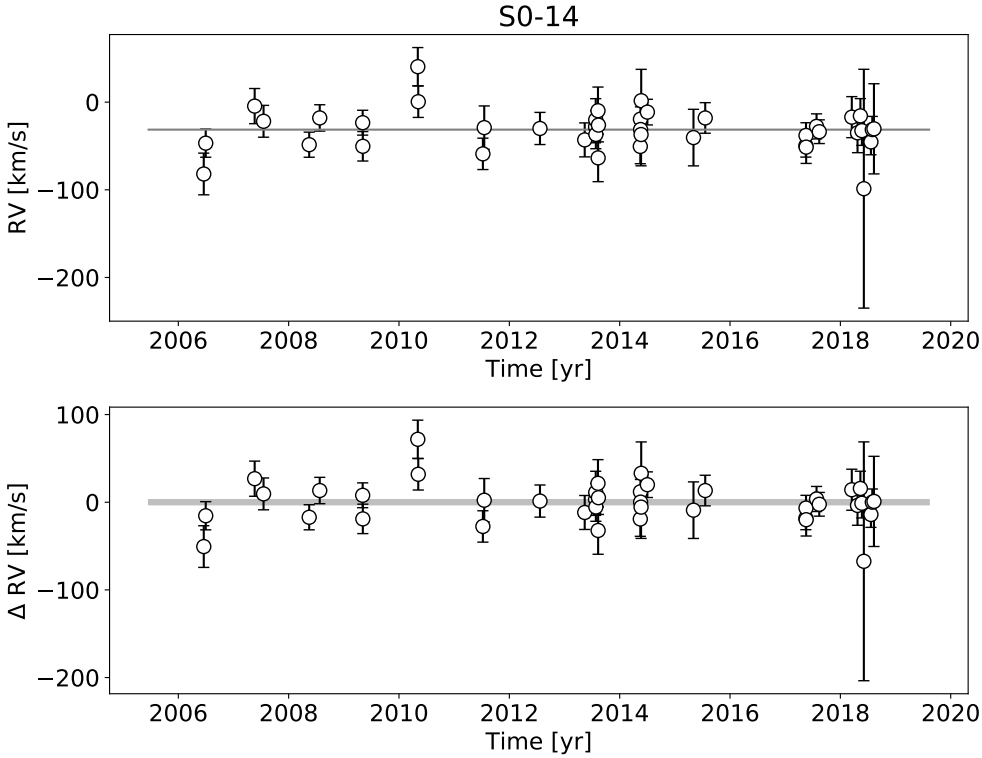

Figure 4.2: Top: Radial velocity of S0-14 over time. A model fit of polynomial order 0 is fit to the data. Bottom: Difference of measured radial velocity points from the model for S0-14. Uncertainty of the model fit is incorporated into the shaded region.

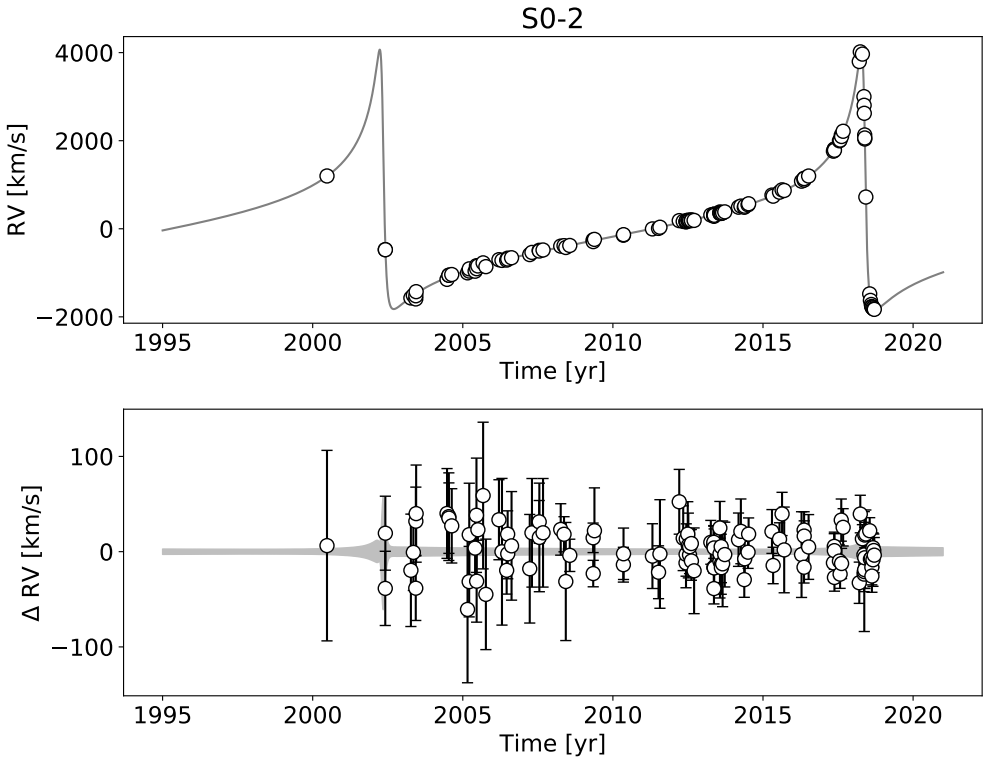

Figure 4.3: Top: Radial velocity of S0-2 over time. An orbital model fit is fit to the data is shown by the line. Bottom: Difference of measured radial velocity points from the model for S0-2. Uncertainty of the orbital model fit is incorporated into the shaded region. This orbital fit was first reported in Do et al. (2019).

4.3.2 Lomb-Scargle Analysis

Once a star's residual radial velocity curve is made, we run a Lomb-Scargle analysis to search for a periodic signal. We use the Lomb-Scargle package described in VanderPlas & Ivezić (2015); Vanderplas et al. (2016). When running this periodic search, we sample a range of periods from 2 to 1000 days. To ensure that we do not miss potential signals between on our uniformly spaced sampling, we use the "N samples per peak" feature. We specify $N = 10$ samples per peak, which carries out 10 additional, finer samples around a peak in Lomb-Scargle power (see VanderPlas & Ivezić 2015; Vanderplas et al. 2016). The periods are uniformly spaced at $1/N\Delta t$, where N is the samples per peak and Δt is the maximum time baseline of observations. Spacing the sampled periods at $1/N\Delta t$ ensures proper sampling of a dataset (VanderPlas 2018). The lower limit of 2 days comes the minimum period we would be sensitive to with our observing cadence. Chu et al. (2018) calculated an upper limit of 119 days for the longest period for an S0-2 binary star system, as systems with longer periods would separated at S0-2's closest approach to the SMBH. The stars in this sample are not expected to pass as close to the SMBH, hence would have longer maximum periods, which is why we decided to increase the upper period sampled. After this step, we obtain a Lomb-Scargle power spectrum, with power values for every sampled period. Example Lomb-Scargle periodograms for S0-14 and S0-2 are shown in Figures 4.4 and 4.5, respectively.

The next step we need to do is determine the significance of the Lomb-Scargle powers. We do this in two ways: i)Monte Carlo simulations and ii)bootstrap false alarm probability (FAP).

The Monte Carlo is conducted in the same way as described in Chu et al. (2018). To summarize, we generated 100,000 simulated residual curves with no periodic signal. Each simulated curve had the same observation times and uncertainties as the data. For each point, we drew from a Gaussian distribution centered around 0 km s^{-1}. We then ran each simulated curve through the Lomb-Scargle process described above and determined the maximum Lomb-Scargle power for each run. We then compiled a cumulative

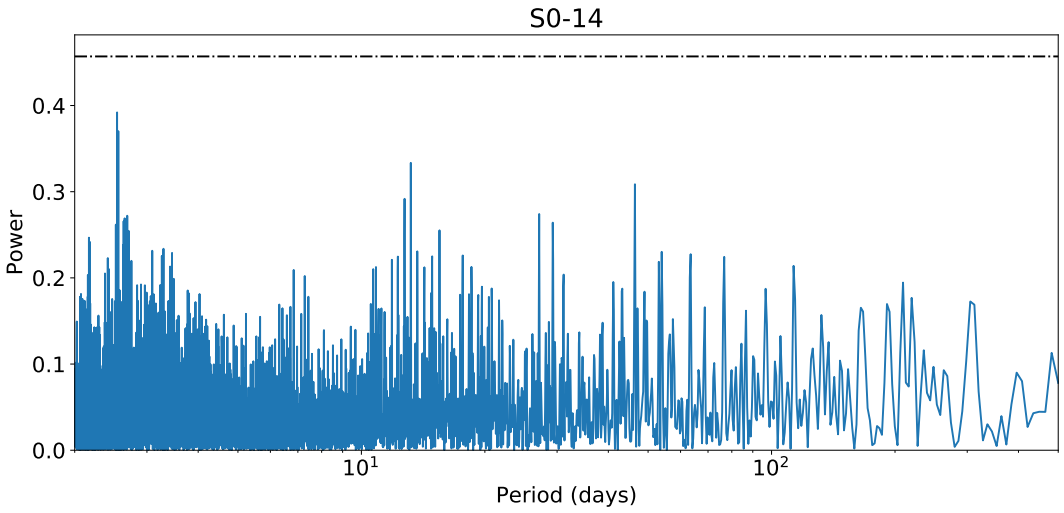

Figure 4.4: Lomb-Scargle periodogram of S0-14's residual radial velocity curve. The black dash-dotted line is the 95% confidence level detection value. No power reaches the 95% confidence level detection value implying that no significant periodic signal is found in the observations.

distribution function for the simulations, found the 3σ confidence level, and compared this value to the power values from the residual curve. This approach allows us to quantify the significance of our peak signal relative to a non-periodic data set taken at the same observation sampling and uncertainties. We define a significant detection to be anything greater than the 3σ confidence level.

The bootstrap FAP is another way to test the significance of the signal in a slightly different view than the Monte Carlo simulations. VanderPlas (2018) explains how the FAP addresses the probability that a signal with no periodic component would lead to a peak of a given magnitude. We choose the bootstrap method because it is the most robust estimate of the FAP (VanderPlas 2018). A similar bootstrap method was implemented by Gautam et al. (2019) to determine the FAP with Galactic center photometry data. For one simulated periodogram, we keep the observation times the same, draw residual values randomly with replacement from the residual curve, and then compute the maximum of the resulting periodogram. This is repeated 10,000 times. We then take the peak periodogram power from the data and compare it to the distribution of power values from the bootstrap to determine the FAP. The bootstrap false alarm test

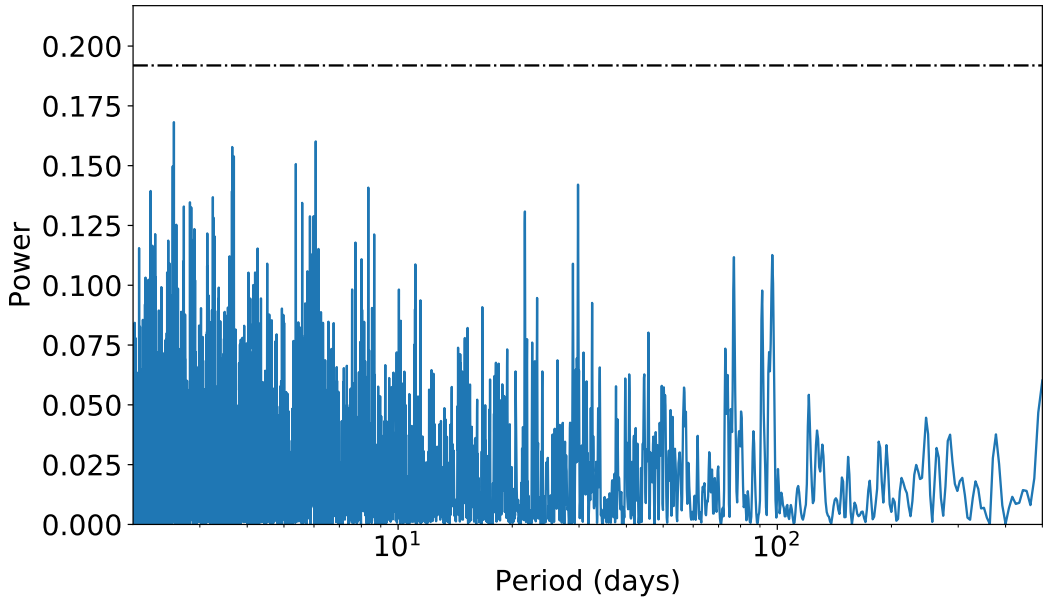

Figure 4.5: Lomb-Scargle periodogram of S0-2's residual radial velocity curve. The black dash-dotted line is the 95% confidence level detection value. No power reaches the 95% confidence level detection value implying that no significant periodic signal is found in the observations.

significance is then defined as 1 - FAP. We define the bootstrap false alarm test to be significant when it is greater than 3σ.

4.3.3 Binary Curve Fitting

The next way we search is through a Bayesian fit of the residual curve to the binary system curve. This is the same as the method described in Chu et al. (2018). We fit the residual curves with a binary star radial velocity model plus a constant. This constant is different than the instrumental offset discussed earlier between instruments. The following equation was used to model the radial velocity curve of an eccentric binary system (Hilditch 2001)

$$RV = K\frac{\sqrt{1-e^2}\cos E\cos\omega - \sin E\sin\omega}{1-e\cos E}, \tag{4.1}$$

with

$$K = \frac{2\pi a \sin i}{P}\,, \tag{4.2}$$

and where e is the binary eccentricity, ω the argument of periastron, E the eccentric anomaly determined by solving the Kepler equation, i the inclination, P the period and a the semimajor axis. This model is parametrized using the following 5 variables: the constant offset O, the radial velocity amplitude K, the eccentricity e, the argument of periastron ω and the mean longitude at J2000 (noted L_0). The use of the mean longitude at J2000 is preferred to the usual time of closest approach which is not bounded and not defined in case of circular orbits (Hilditch 2001). For different fixed binary orbital periods P, we fitted this model to the RV residuals using a MultiNest sampler (Feroz & Hobson 2008; Feroz et al. 2009, 2013). A strong periodic signal at a given period would lead to a large, peaked value of K in the posterior. This method takes into account parameters such as eccentricity, which changes the shape of the curve from a perfect sinusoid wave. We uniformly sampled in log space for periods from 2 to 500 days. For S0-2, we did the same methodology as Chu et al. (2018), where we evenly spaced at 0.05 days for periods from 2 to 150 days since periods beyond 119 days are excluded by the binary stability criteria. Because of the more computationally expensive nature of this method, we did not sample periods as long as the Lomb-Scargle method. An example of this methodology is shown in for S0-14 and S0-2 in Figures 4.6 and 4.7.

4.3.4 Results from the Periodicity Search

We present the detailed results from the Lomb-Scargle periodicity search in Table 4.4. We report that none of the stars' residual curves have periodic variations beyond the 3σ confidence limit using the Monte Carlo method, nor do they have Bootstrap False Alarm significance greater than 3σ, as were detailed in Section 4.3.2. We plot these significance values in Figure 4.8. Additionally, we look at the fit amplitude from the Lomb-Scargle analysis of the highest-power period for each star. We take the amplitude of the sinusoid fit and divide it by the median uncertainty for that star to determine the

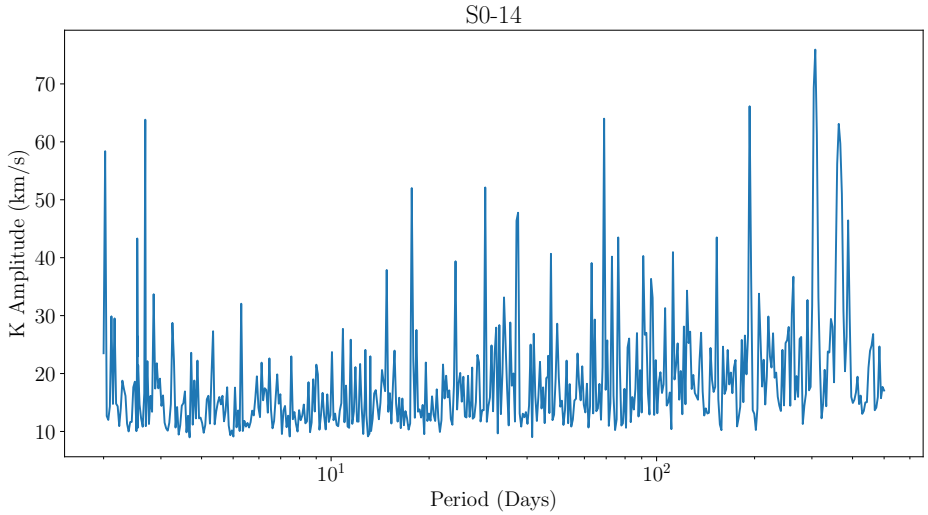

Figure 4.6: 95% upper confidence limit on the amplitude of RV variations induced by a binary system (K) as a function of the binary orbital period for S0-14.

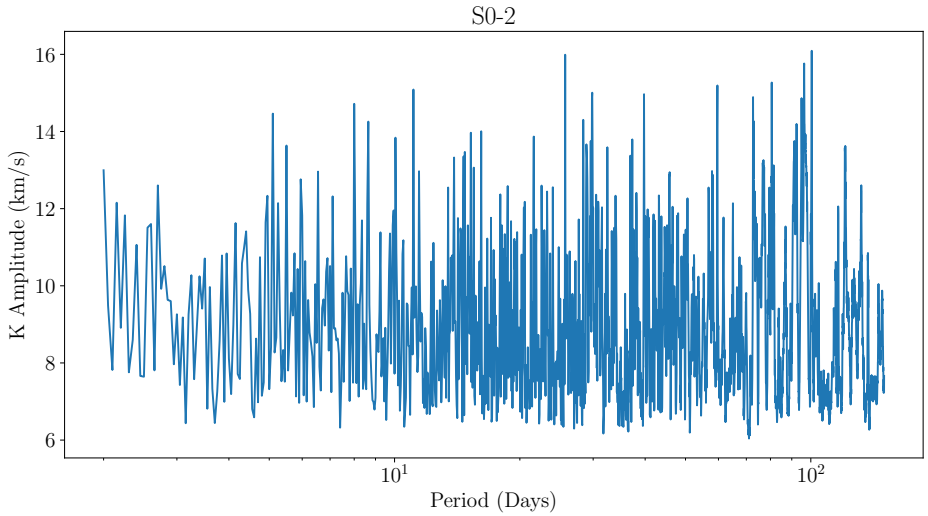

Figure 4.7: 95% upper confidence limit on the amplitude of RV variations induced by a binary system (K) as a function of the binary orbital period.

amplitude significance in terms of sigma. Ultimately, none of these stars have model amplitudes greater than 3 sigma, further showing evidence that there are no significant periodic signals in this sample according to the Lomb-Scargle method (Figure 4.9).

Table 4.4. Lomb-Scargle Periodicity Search Results

Star	Spectral Type	Residual Amp. (km s^{-1})	Median σ (km s^{-1})	Amp./σ	Bootstrap False Alarm Test Significance	Monte Carlo Test Significance
S0-1	Early	68	54	1.26	92.34%	99.94%
S0-2	Early	12	23	0.50	72.00%	80.32%
S0-3	Early	26	37	0.70	94.70%	90.03%
S0-4	Early	43	46	0.94	92.50%	98.66%
S0-5	Early	24	61	0.40	94.88%	98.52%
S0-7	Early	53	30	1.76	93.80%	92.38%
S0-8	Early	66	95	0.69	96.40%	99.79%
S0-9	Early	37	36	1.04	95.90%	92.38%
S0-11	Early	26	32	0.82	90.20%	86.80%
S0-14	Early	17	18	0.92	98.60%	70.99%
S0-15	Early	35	32	1.08	93.50%	33.37%
S0-16	Early	98	75	1.31	67.00%	99.27%

Table 4.4 (cont'd)

Star	Spectral Type	Residual Amp. (km s^{-1})	Median σ (km s^{-1})	Amp./σ	Bootstrap False Alarm Test Significance	Monte Carlo Test Significance
S0-19	Early	18	118	0.15	64.00%	99.73%
S0-20	Early	14	195	0.07	88.60%	99.97%
S0-31	Early	34	41	0.82	100.00%	42.34%
S1-8	Early	62	33	1.87	90.40%	29.82%
S1-33	Early	74	32	2.33	92.00%	43.47%
S0-6	Late	2	3	0.73	98.08%	92.13%
S0-12	Late	3	3	1.07	99.00%	94.57%
S0-13	Late	3	3	1.00	90.50%	86.34%
S0-17	Late	24	90	0.27	75.00%	99.90%
S0-18	Late	11	4	2.63	97.80%	73.03%
S0-27	Late	14	7	1.99	90.30%	52.30%
S1-5	Late	4	3	1.33	92.70%	4.47%

Table 4.4 (cont'd)

Star	Spectral Type	Residual Amp. (km s^{-1})	Median σ (km s^{-1})	Amp./σ	Bootstrap False Alarm Test Significance	Monte Carlo Test Significance
S1-6	Late	14	8	1.70	96.30%	63.66%
S1-10	Late	5	5	1.04	99.00%	95.40%
S1-13	Late	14	5	2.80	100.00%	45.61%
S1-15	Late	6	4	1.43	93.20%	46.69%
S1-31	Late	10	8	1.23	82.50%	51.89%

Because we found no periodic signal that passed our criteria, we conclude that the S-stars in the sample do not contain detectable signals of being part of a spectroscopic binary system. We report the median limits on K amplitude in Table 4.5. The median K amplitude results for the sample are also shown in Figures 4.10 and 4.11.

4.4 Placing limits on companion masses

With the results from the binary curve fitting, in particular our limits on the K amplitude, we move to place limits on hypothetical companion masses of binary systems. We use the same methodology as Chu et al. (2018). For each period P, we have a limit on K, and we solve for the binary mass equation:

$$M_{\text{comp}} \sin i = \left(\frac{P M_{tot}^2}{2\pi G} \right)^{1/3} K \,, \tag{4.3}$$

Assuming for a total mass, we can calculate a limit for the companion mass for each period. In order to determine the total mass for a star, we use its K' photometry reported Gautam et al. (2019) and an isochrone generated with the SPISEA software (Hosek et al. 2020a,b). For early-type stars, we use an 6.78 Myr isochrone. For late-type stars, we use a 1 Gry isochrone. Each isochrone is corrected for extinction to the Galactic Center with a value of $A_{K'} = 2.46$ (Schödel et al. 2010). We also use solar metalicities for both isochrones. These isochrones are shown in Figure 4.12. The total mass we use for each star is given in Table 4.5. Habibi et al. (2017) reported masses for early-type S-stars stars in their analysis. For stars that overlap with our sample, their reported mass values are lower than the isochrone mass values but still consistent within 2σ. We report the median upper limits for the companion masses for all periods in Table 4.5 and Figure 4.13.

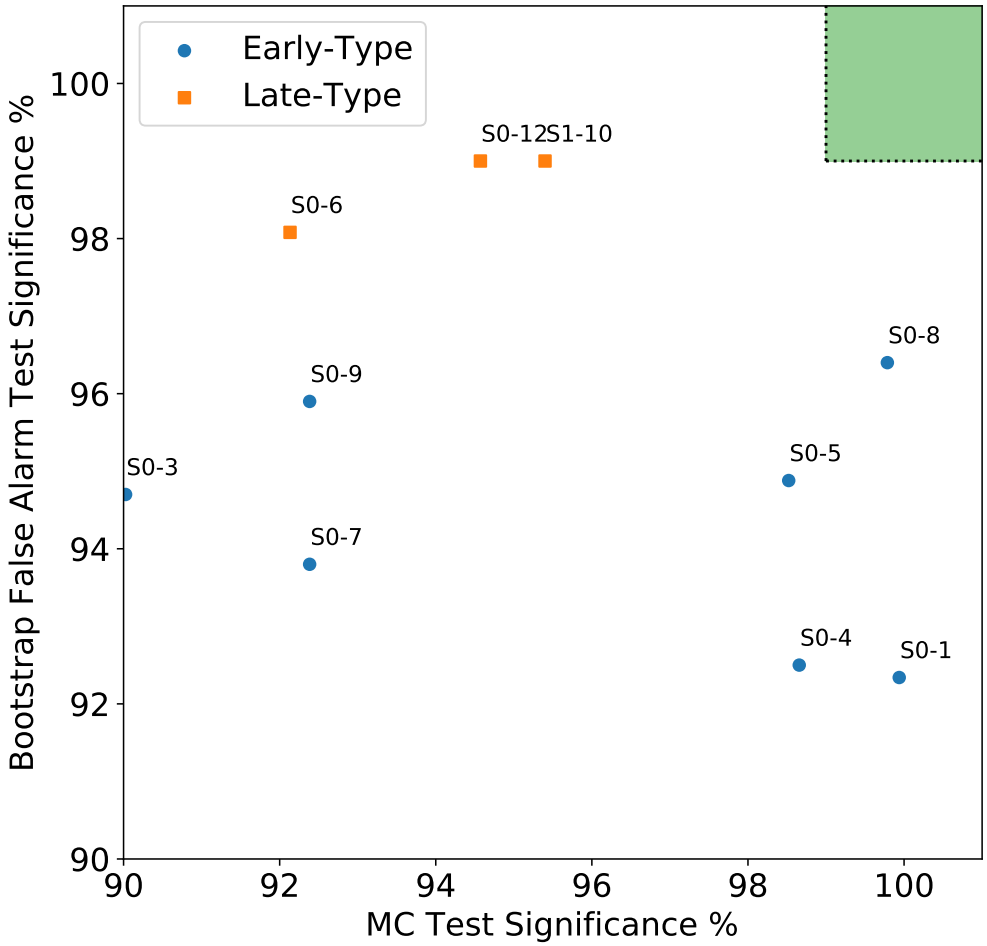

Figure 4.8: Significance of Monte Carlo simulation and significance of bootstrap false alarm test, focusing on stars with the highest significance. Stars shown in this diagram have highest values for both significance values. A star is considered periodic if the significance values are greater than 3σ for both tests, a region shown by the green shaded square. No stars meet the criteria for significant periodicity.

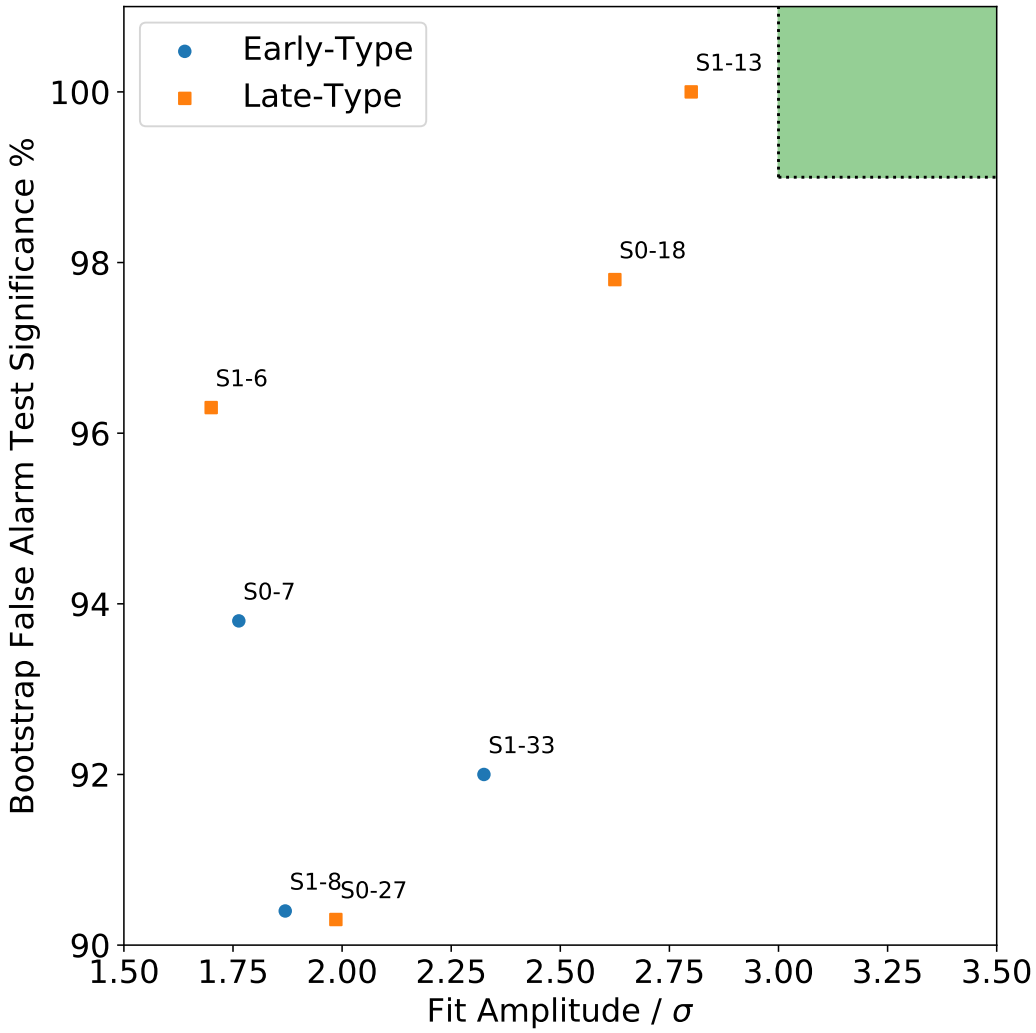

Figure 4.9: Significance of Lomb-Scargle fit amplitude divided by median RV error and significance of bootstrap false alarm test, focusing on stars with the highest significance. Stars shown in this diagram have highest values for both significance values. A star is considered periodic if the significance values are greater than 3σ for both tests, a region shown by the green shaded square. No stars meet the criteria for significant periodicity.

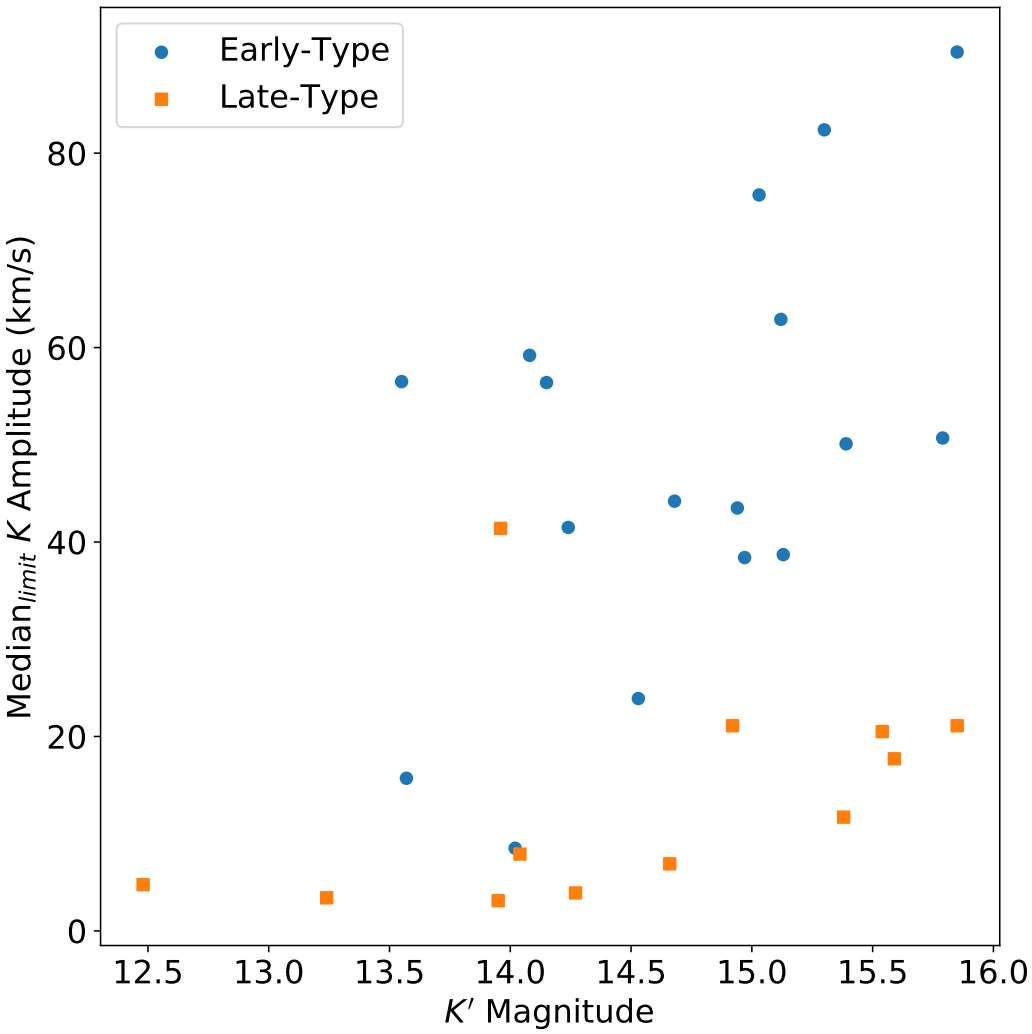

Figure 4.10: Median K amplitude value plotted with the K' magnitude for each star, color coded by their spectral types. The median K amplitude value comes from marginalizing the K amplitude limits over all sampled periods.

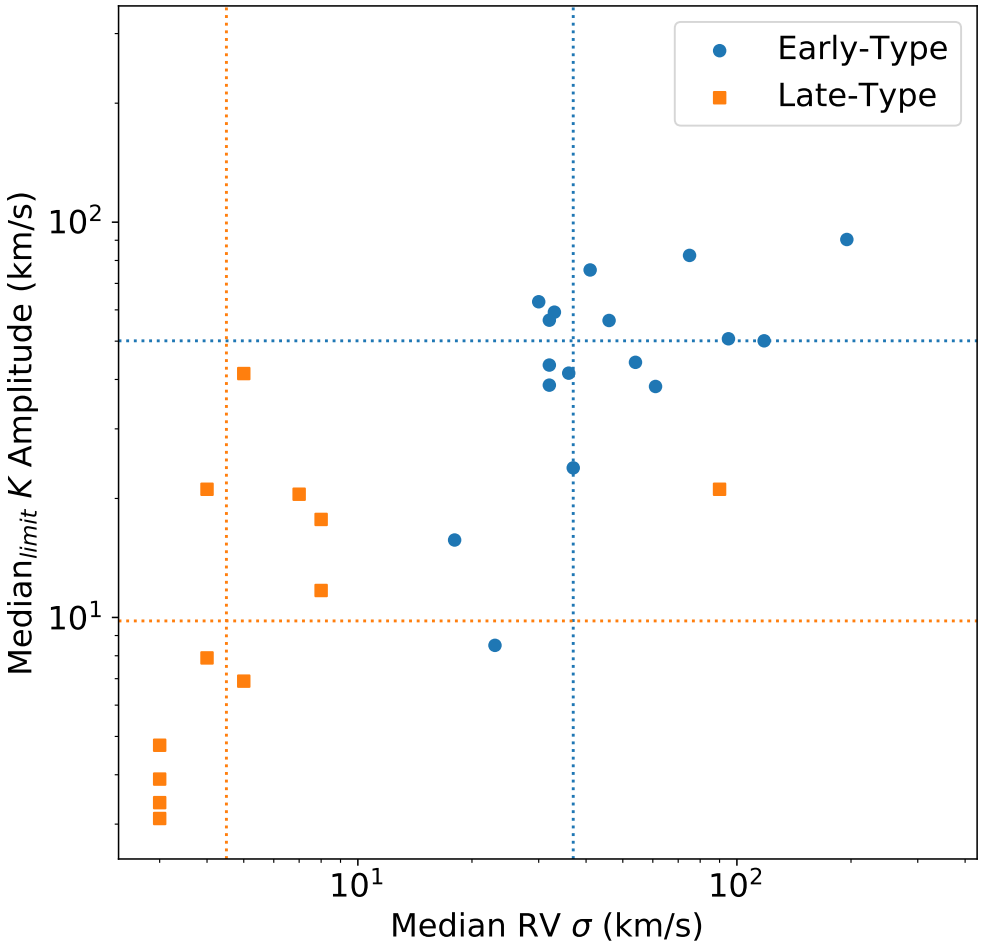

Figure 4.11: Median RV uncertainty plotted with the median limit K amplitude value for each star, color coded by their spectral types. The median K amplitude value comes from marginalizing the K amplitude limits over all sampled periods. The dashed lines represent the median values of the limits and RV uncertainties for both the early-type and late-type stars.

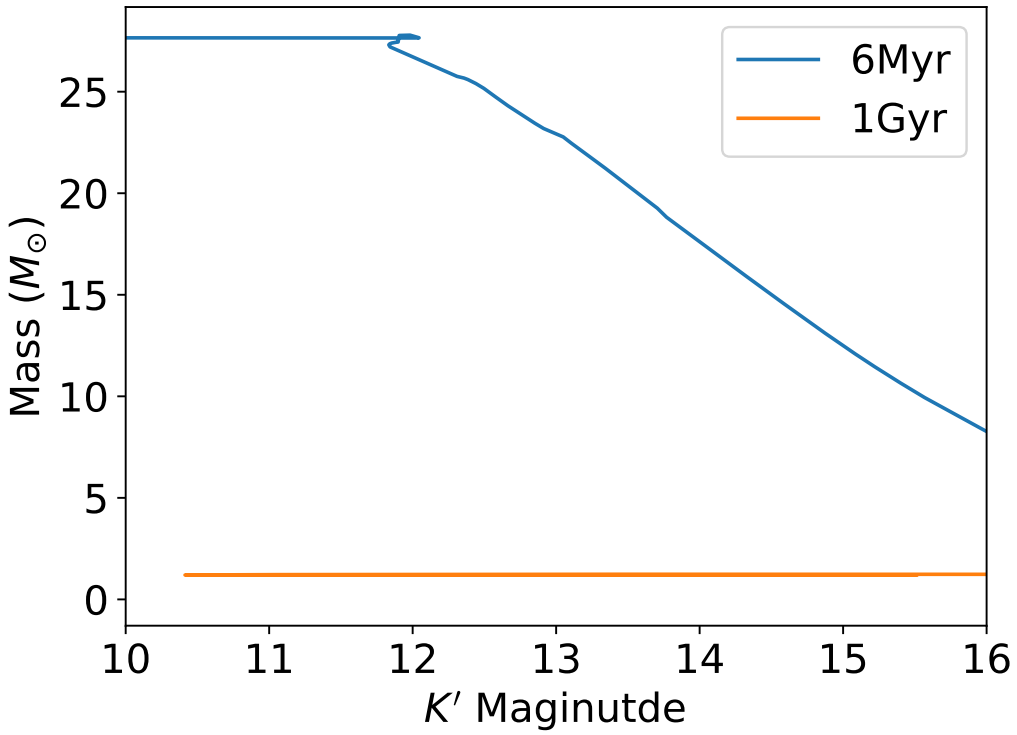

Figure 4.12: Two SPISEA isochronese used for determining the mass of a star based on its K' magnitude. The 6Myr isochrone was used for the early-type stars, while the 1 Gyr isochrone was used for the late-type stars.

4.4.1 Using Photometry to Place Constraints

We also use photometry of each star to place limits on the masses of an equal mass binary system. We take the total flux from the star and divide the flux in half. We then search the SPISEA isochrone to find the mass of a star that would contribute the equivalent amount of flux. This places a limit on the components of a face-on binary system composed of equal mass stars. This can be thought of as a conservative limit, as the spectral differences between different mass stars are not considered in this part of the analysis. These limits are reported in Table 4.5.

Table 4.5. Mass Limits

Star	Mean Mag (K')	Spectral Type	Isochrone Mass ($M_\odot$)	Med$_{\rm lim}$ K (km s^{-1})	Med$_{\rm lim}$ M_{comp} Mass ($M_\odot$)	Med$_{\rm lim}$ Mass Ratio	Equal Mass Binary ($M_\odot$)
S1-5	12.48	Late	1.2	4.75	0.1	0.08	1.2
S0-13	13.24	Late	1.2	3.4	0.1	0.08	1.2
S0-15	13.55	Early	20.2	56.5	5.4	0.267	16.7
S0-14	13.57	Early	20.0	15.7	1.7	0.085	16.3
S0-6	13.95	Late	1.2	3.1	0.1	0.08	1.2
S1-13	13.96	Late	1.2	41.4	0.7	0.58	1.2
S0-2	14.02	Early	17.5	8.5	1.1	0.06	14.2
S1-15	14.04	Late	1.2	7.9	0.1	0.08	1.2
S1-8	14.08	Early	17.0	59.2	5.6	0.329	13.9
S0-4	14.15	Early	16.7	56.4	5.7	0.341	13.7
S0-9	14.24	Early	16.3	41.5	3.8	0.233	13.4
S0-12	14.27	Late	1.2	3.9	0.1	0.08	1.2

Table 4.5 (cont'd)

Star	Mean Mag (K')	Spectral Type	Isochrone Mass ($M_\odot$)	Med$_{\rm lim}$ K (km s^{-1})	Med$_{\rm lim}$ M_{comp} Mass ($M_\odot$)	Med$_{\rm lim}$ Mass Ratio	Equal Mass Binary ($M_\odot$)
S0-3	14.53	Early	14.9	23.9	2.2	0.147	12.1
S1-2	14.64	Early	14.2	75.68	5.2	0.388	11.7
S1-10	14.66	Late	1.2	6.9	0.1	0.08	1.2
S0-1	14.68	Early	13.9	44.2	3.1	0.223	11.4
S0-18	14.92	Late	1.2	21.1	0.4	0.33	1.2
S1-33	14.94	Early	12.8	43.5	3.5	0.277	10.5
S0-5	14.97	Early	12.6	38.4	2.2	0.174	10.3
S0-31	15.03	Early	12.3	75.7	4.9	0.485	10.1
S0-7	15.12	Early	11.9	62.9	4.6	0.386	9.7
S0-11	15.13	Early	11.9	38.7	3.0	0.252	9.7
S0-16	15.3	Early	11.0	82.4	5.4	0.49	9.0
S0-19	15.36	Early	10.9	50.1	3.6	0.33	8.9

Table 4.5 (cont'd)

Star	Mean Mag (K')	Spectral Type	Isochrone Mass ($M_\odot$)	Med$_{\rm lim}$ K (km s^{-1})	Med$_{\rm lim}$ M_{comp} Mass ($M_\odot$)	Med$_{\rm lim}$ Mass Ratio	Equal Mass Binary ($M_\odot$)
S1-6	15.38	Late	1.2	11.7	0.2	0.16	1.2
S0-27	15.54	Late	1.2	20.5	0.3	0.25	1.2
S1-31	15.59	Late	1.2	17.7	0.3	0.25	1.2
S0-8	15.79	Early	9.0	50.7	3.1	0.344	7.4
S0-20	15.85	Early	8.8	90.4	5.8	0.644	7.2
S0-17	15.85	Late	1.2	21.1	0.3	0.25	1.2

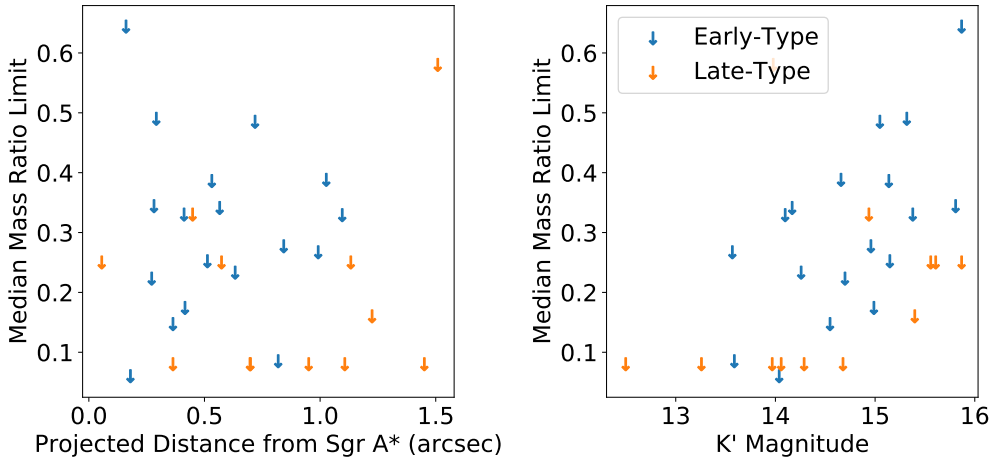

Figure 4.13: Left: Median companion mass limits for each star plotted with their projected distance from Sgr A*. These median companion mass limits come from marginalizing the mass limits over all sampled periods. Right: Median companion mass limits for each star plotted with their K' magnitude.

4.5 Discussion

4.5.1 Placing the Lack of Detections into Context - Early-Type Stars

Performing this systematic search for spectroscopic binaries has yielded no candidates, and we can use this result to place limits on the intrinsic binary population. Sana et al. (2012) reports distributions of binary system parameters (mass ratios q, eccentricities, periods) for massive star populations. We draw from the given distributions of log P, e, and mass ratio q from Sana et al. (2012), shown in Figure 4.14. We do this 100,000 times to create a population of 100,000 binary systems. Using Eq 2.5, we can calculate the distribution of K amplitudes for this simulated binary star population. When generating a binary system, we also make sure that the system does not result in a merger by calculating the minimum separation and ensuring it does not fall below the radius of the star (~ 6 $R_\odot$). With this distribution, we can then place our K amplitude limits - and zero detections - in context with this simulated population.

The calculated K amplitude distribution described above is for a population made completely of binaries (a binary fraction of 100%). To make K amplitude distributions

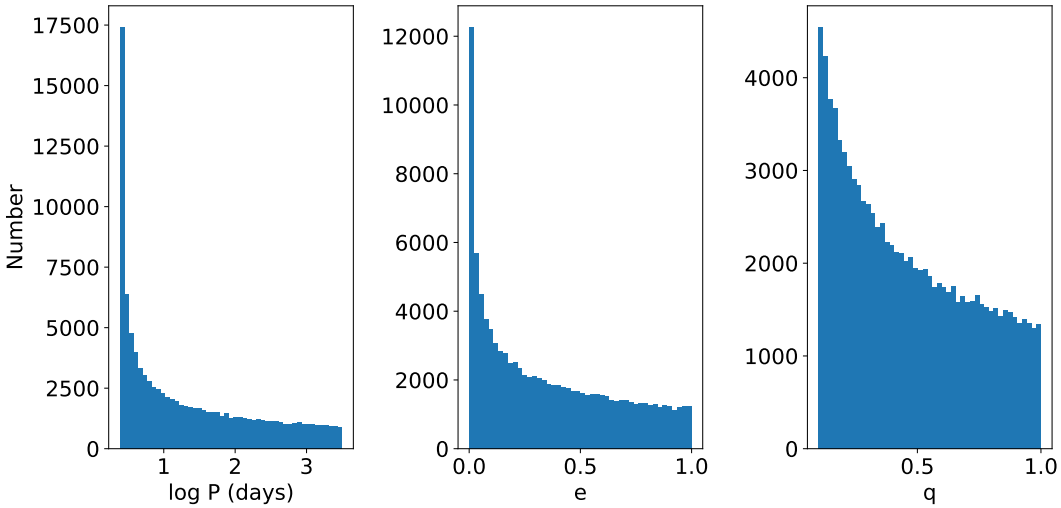

Figure 4.14: Distribution of binary star parameters from Sana et al. (2012) that were drawn from to make our K amplitude distributions.

for binary fraction less than 100%, we randomly replace the corresponding percentage of K values with 0 km s^{-1}, representing the single star population. For example, a population with a binary fraction of 50% will have 50,000 values of 0 km s^{-1}, and 50,000 values randomly drawn from the original simulated distribution. We create adjusted K amplitude distributions for different populations with binary fractions ranging from 10 - 100%, spaced evenly at 10%. We manually conduct finer sampling at binary fractions between 30-50%.

Once we have our adjusted K amplitude distribution, we run our detection simulation. We take the median K limit from each of our 17 early-type stars in Table 4.5. We compare each value from our sample to a randomly drawn K value from our adjusted distribution. If the drawn K value from the population is higher than the limit from the sample star, we consider it a detection. For each simulation, we can have a minimum of 0 detections and a maximum of 17 detections. We repeat this simulation 100,000 times, for each different adjusted K amplitude distribution.

We plot the fraction of simulations with 0 detections for each adjusted K amplitude distribution in Figure 4.16. We found that for a population with a 42% binary fraction, 5% of the of simulations yielded 0 detections. Based on this simulation and our 0 binary

detections, we can exclude a binary fraction greater than 42% for this population with a 95% confidence limit. This limit is well below the $70 \pm 9\%$ binary fraction value reported in Sana et al. (2012). A merger rate of 13% and evaporation rate of 27% for all young binaries at the Galactic Center may help explain this discrepancy (Stephan et al. 2016). Starting with a binary fraction of 70% from Sana et al. (2012) and having 60% of young binary systems survive (40% of binaries merge or evaporate) according to Stephan et al. (2016), the resulting binary fraction would be 42%. We note that these limits are dependent on the binary system separation and mass.

The fact that we do not find any binary stars among the young S-stars attests to formation mechanisms that result in a low binary fraction. This includes the binary disruption scenario, where the S-star we see is a tidally captured star originally part of binary system (Hills 1988; Perets et al. 2009). Additionally, these S-stars may be merger products that appear as main-sequence B-stars (Stephan et al. 2016; Stephan et al. 2019).

4.5.2 Placing the Lack of Detections into Context - Late-Type Stars

We apply a similar simulation approach as described in Section 4.5.1 to the late-type stars. We draw from the distribution of binary properties reported in Raghavan et al. (2010) to create our K amplitude distributions, which focused on systems around a solar mass (see Figure 4.15).

Following the same steps as in 4.5.1, we obtain the fraction of simulations with 0 detections for each population of binary fractions. We found that even for binary fractions of 100%, around 30% of our simulations had 0 detections 4.16. This mostly has to do with the fact that the K amplitude distribution for this population is dominated by small values. This is expected, as K is $\propto P^{-1/3}$, so K decreases with long period binaries. Since the Raghavan et al. (2010) distribution is dominated by long period binaries ($P = 10^5$ days), it is expected that the K amplitude distribution would mostly contain small values.

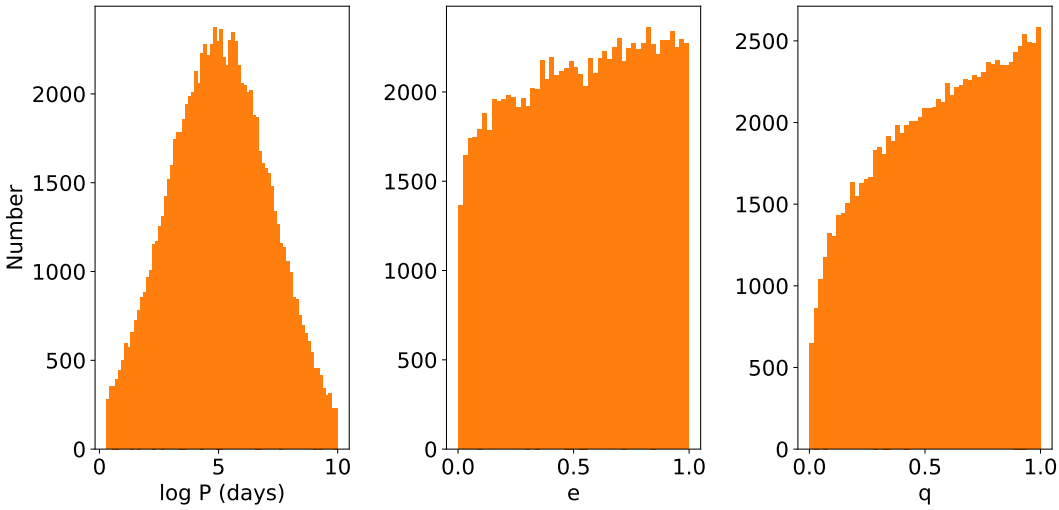

Figure 4.15: Distribution of binary star parameters from Raghavan et al. (2010) that were drawn from to make our K amplitude distributions.

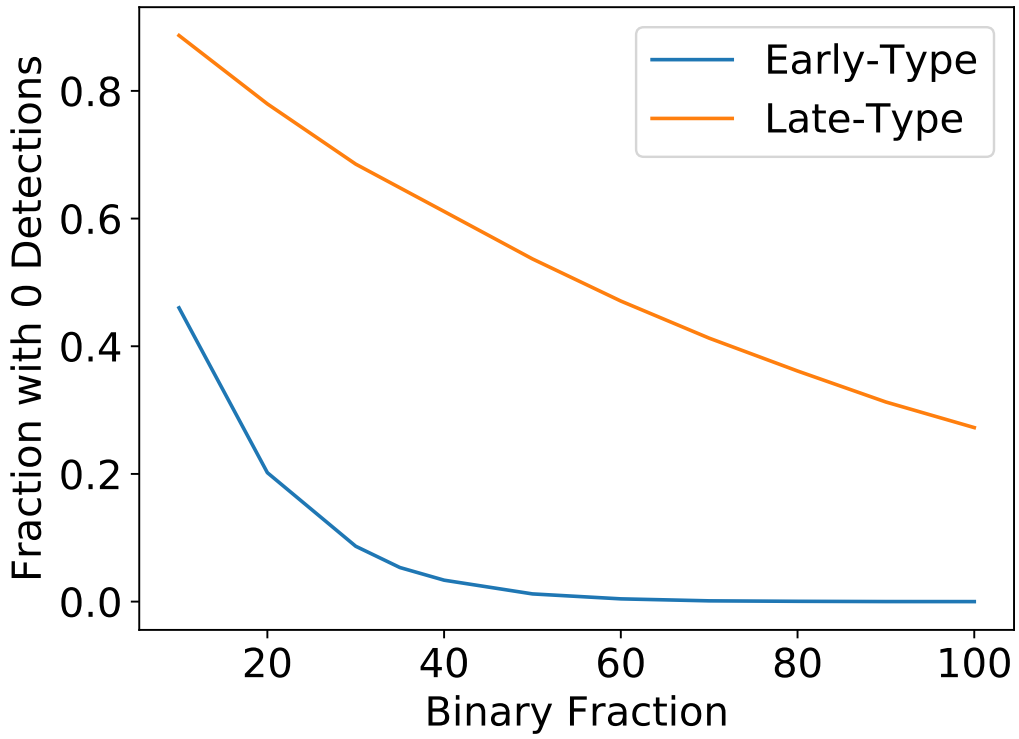

Figure 4.16: The fraction of simulations with 0 detections for each population of binary fractions, for both early-type and late-type stars. Our constraining power lies with the early-type stars, as the K amplitude distribution contains higher values of K compared to the late-type distribution.

Not identifying binary candidates among the late-type stars is not surprising. Stephan et al. (2016); Stephan et al. (2019) reports that the evaporation timescale for a binary system with a total mass of $2M_{\odot}$ and separated by 3 AU (P ~ 1300 days) evaporates in under 10^6 years. Since these late-type stars are $\sim$ 1 Gyr old, these stars have had sufficient time to evaporate, if they were previously part of binary star systems. After a Gyr, Stephan et al. (2016) explains that there has been more time for mergers to take place, so even though binary star systems can survive longer than the evaporation time due to hardening interactions, these hardened, close binary stars can merge as they evolve off the main-sequence[2]. These compounding effects means it is unsurprising that we do not find binaries among this population.

For consistency in approach, we used the entire Raghavan et al. (2010) binary period distribution for our analysis, but it is incredibly unlikely that solar mass binary systems with these long periods would have survived.

4.6 Conclusion

We have finished systematic search for spectroscopic binaries for stars located within an arcsecond of the black hole. We found no significant periodic detection these stars' radial velocities and detect no binary candidates. We then place limits on binary radial velocity curve amplitudes and companion masses for these stars. By drawing from reported binary simulations, we are able to place some limits on the binary fraction of the stars closest to the black hole. We place a limit of 42% for the early-type stars, which is well below the binary fraction of 70% reported for massive stars in nearby field stars. These limits are dependent on the binary system separation and mass. Expanding on the statistics of the simulations can help lead to further insights into the limits on the intrinsic binary fraction of the region. Additionally, continued monitoring of these stars will further improve our measured binary limits, or may also lead to detections of

[2]These merged stars would also appear younger by comparison.

binary systems.

CHAPTER 5

Extension of the Galactic Center OSIRIS Wide-field Survey

We present new high angular resolution near-infrared spectroscopy observations with adaptive optics of the nuclear star cluster surrounding the Milky Way supermassive black hole. This work is a 11 field extension of the Galactic Center OSIRIS Wide-field Survey (GCOWS) and includes observations that span 6 years. We spectral type 169 stars: 47 of which are Wolf-Rayet and O/B stars, and the remaining 122 are K and M giants. This addition to the rich GCOWS data set provides opportunities to further study stellar demographics and dynamics of the nuclear star cluster.

5.1 Introduction

Near-IR integral-field spectroscopy behind adaptive optics has proved to be extremely valuable for studying the stellar population and kinematics at the Galactic center. The near-IR wavelength coverage enables observers to peer through the large amounts of visual extinction, and the adaptive optics technology has enable astronomers to spatially resolve individual sources in the crowded region. Spectroscopy plays a crucial role in spectral typing stars at the Galactic center, as imaging data alone cannot distinguish Wolf-Rayet and O/B main-sequence (young) stars from evolved red giants (old stars) (Do et al. 2013). The advent of spectroscopy data has led to the ground breaking discoveries such as: (1) the existence of young, main-sequence B-stars within 0.04 pc of the supermassive black hole (SMBH), raising questions about their formation so close to the black hole (e.g. Ghez et al. 2003; Eisenhauer et al. 2005; Habibi et al. 2017), (2) a

clockwise disk of young stars located just over 1″ from the SMBH (e.g. Lu et al. 2009; Bartko et al. 2009), (3) a potentially missing stellar cusp of red giant stars, which would be expected from a relaxed population around the SMBH (e.g. Do et al. 2009), and (4) a population of dust-enshrouded objects (e.g. Gillessen et al. 2012; Witzel et al. 2014; Ciurlo et al. 2020).

The combination of spectral and positional information makes data from adaptive-optics fed imaging spectrographs valuable tools for studying the Galactic center. Stars can be spectral typed to determine their ages and placed into their respective population of young or old stars. Spectroscopy also provides radial velocities, and when combined with extensive proper motion studies, provide valuable information into the three dimensional motions of Galactic center stars.

The UCLA Galactic Center Group began an observing campaign to observe the central nuclear star cluster, known as the Galactic Center OSIRIS Wide-field Survey (GCOWS, Do et al. 2013). This work builds upon the initial phase of the GCOWS survey reported in Do et al. (2013). The first phase observed fields east of Sgr A*, located along the projected disk of the young stellar disk. This extended phase observed fields located to the north and south of Sgr A*, perpendicular to the plane of the disk. The addition of this dataset provides valuable information for understanding the dynamics and population of the region.

5.2 Observations and Data

New observations of near-IR integral-field spectra were obtained between 2013 and 2019 using the OH-Suppressing Infrared Imaging Spectrograph (OSIRIS; Larkin et al. 2006) on the Keck I Telescope. Observations were taken with the narrowband filter Kn3 (2.121-2.220 μm) and a plate scale of 50 mas per pixel. We observed 8 fields south Sgr A* and 3 fields north of Sgr A*. These fields are perpendicular to the plane of the clockwise disk of young stars identified by Lu et al. (2009). The details of adaptive optics setup and calibrations are the same as reported in Do et al. (2013). Each field was

Table 5.1. Summary of GCOWS OSIRIS Observations

Field Name	Field Center[a] (")	Date (UT)	$N_{\text{frames}} \times t_{\text{int}}$ (s)	Scale (mas)	FWHM[b] (mas)	Filter	PA (°)
N5-3	-0.37, 11.21	2013-05-17	3×900	50	75	Kn3	285
S4-1	-0.87, -11.03	2014-05-20	6×900	50	90	Kn3	195
S4-2	-3.19, -10.41	2014-05-20	8×900	50	89	Kn3	195
S4-3	-5.50, -9.79	2014-06-05	9×900	50	140	Kn3	195
S3-2	-2.35, -7.31	2014-07-18	6×900	50	94	Kn3	195
N5-1	4.40, 9.93	2016-07-21	5×900	50	77	Kn3	195
N5-1	4.40, 9.93	2016-07-22	3×900	50	61	Kn3	195
N5-2	2.01, 10.58	2016-07-22	5×900	50	98	Kn3	195
S2-3	-3.80, -3.59	2019-05-25	5×900	50	89	Kn3	195
S2-2	-1.49, -4.21	2019-05-27	5×900	50	103	Kn3	195
S3-1	-0.03, -7.95	2019-05-27	2×900	50	135	Kn3	195
S3-1	-0.03, -7.95	2019-07-08	3×900	50	145	Kn3	195
S3-3	-4.66, -6.67	2019-07-08	4×900	50	133	Kn3	195

[a]R.A. and decl. offset from Sgr A* (R.A. offset is positive to the east).

[b]Average FWHM of a relatively isolated star for the night, found from a two-dimensional Gaussian fit to the source.

observed with multiple 900 s exposures, separated by $\sim$0."1 dither offsets, representing a size of roughly 10 arcsec^2. This observing campaign spanned over 6 years and new observations are reported in Table 5.1. Images for each field, along with the spectral-typed stars are given in Figures 5.1-5.7.

These data were reduced using the most up to date version of the OSIRIS data reduction pipeline (Lyke et al. 2017; Lockhart et al. 2019). The pipeline assembles the data cubes, with the dimensions being position x, position y, and the spectral wavelength dimension λ. Sources are identified and matched with a catalog in the same way as Do et al. (2013). To summarize, we run the point-spread function (PSF) fitting routine *StarFinder* (Diolaiti et al. 2000) on an OSIRIS cube collapsed in the spectral wavelength dimension. We then match these sources to those identified in imaging data of the same region (Yelda et al. 2014, and references there in).

Spectral extraction for the stars is done in the same ways as reported in works such as Do et al. (2013). Spectra are extracted along the spectral channel with a circular aperture centered at the location of each star detected in imaging space. We use the median flux values in an annulus with an inner radius of 1–2 pixels and an outer radius of 2–4 pixels to conduct sky and background subtraction. We then correct for telluric absorption lines in the same way described in Do et al. (2013).

5.3 Spectral Typing

A primary goal of the GCOWS survey is to differentiate the young stars (Wolf-Rayet and O/B stars) from the old stars (M and K giants). We consider early-type stars to be stars with a spectral type of B or earlier. Late-type stars are all stars with spectral types later than B. Our manual method for spectral typing stars matches that of Do et al. (2013).

We consider stars late-type if they have significant Na I absorption lines. We manually identify 122 late-type stars and list these stars in Table 5.2. Sources with Brγabsorption and no Na I features are classified as early-type. We also classify bright ($K' \leq 13.0$) stars with no absorption features between 2.121 and 2.220 μm as early-type. These sources are most likely O_V or O/B_I stars with very weak Brγ gamma absorption or emission features (Do et al. 2013). We also include Wolf-Rayet stars in the early-type sample. We find a total of 47 early-type stars, listed in Table 5.3. This work reports a total of 169 spectral typed sources.

5.4 Early-Type Radial Velocities

For stars with sufficient signal to noise and significant Brγabsorptions lines, we measure their radial velocities by fitting a BOSZ grid of spectral models (Bohlin et al. 2017) to the data using the Starkit software package (Kerzendorf & Do 2015). This is the same method used to measure radial velocities of the main-sequence B star S0-2 in Do et al.

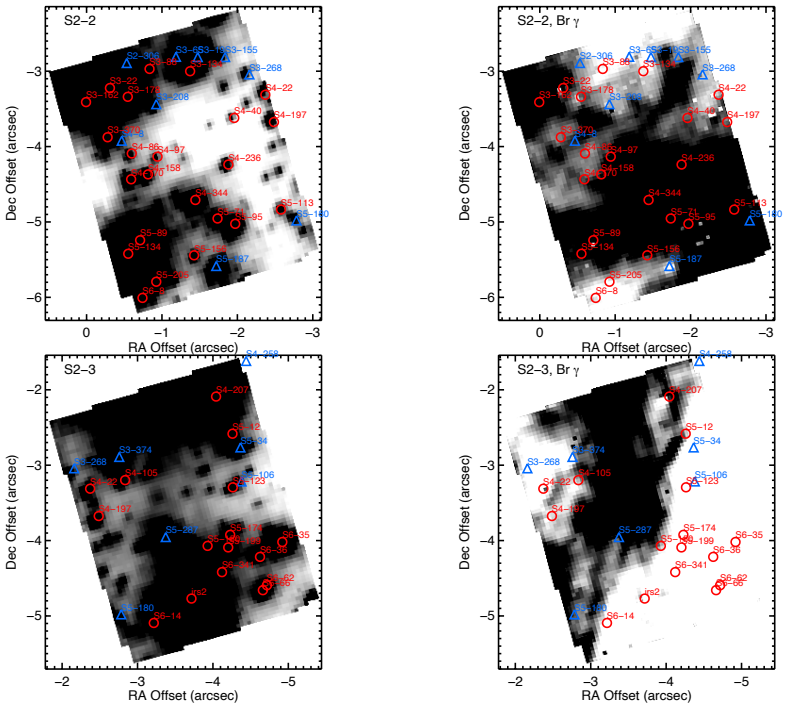

Figure 5.1: Images from collapsing the OSIRIS data cubes along the spectral wavelength dimension for each individual pointing of the GCOWS survey. Shown here are fields S2-2 and S2-3. Left: median of all spectral channels. Right: spectral channels near the Br gamma line showing the gas emission. The images are oriented with north up and east to the left. Spectroscopically identified early (blue triangles) and late-type (red circles) stars are marked.

(2019). This method only works if there are absorption lines, which is why only stars with Brγ absorption lines have measured radial velocities. Stars that are featureless in this region or emission line sources are excluded. We report 6 radial velocities in Table 5.3 We leave the radial velocity measurements of late-type stars to future work.

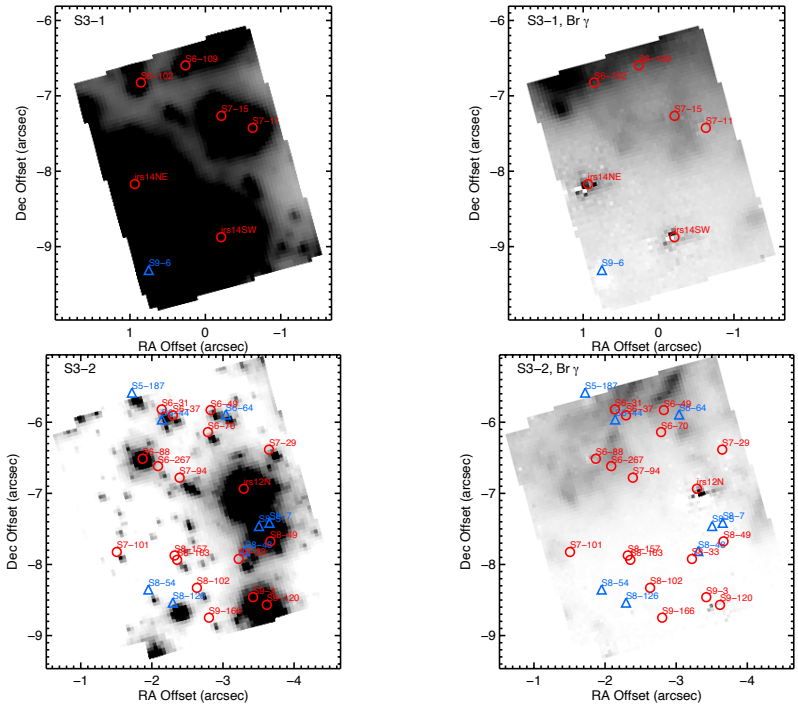

Figure 5.2: Similar to Figure 5.1, with fields S3-1 and S3-2 shown.

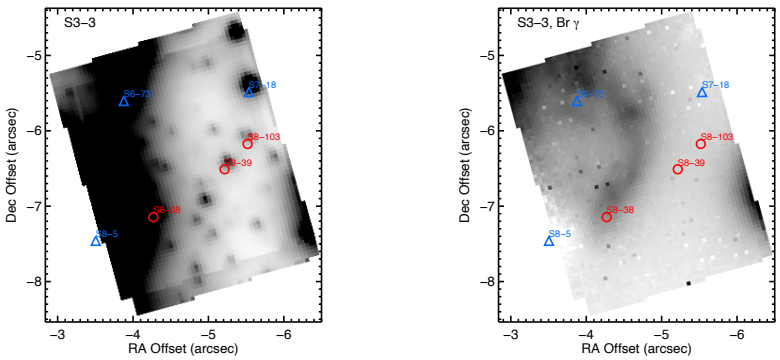

Figure 5.3: Similar to Figure 5.1, with field S3-3 shown.

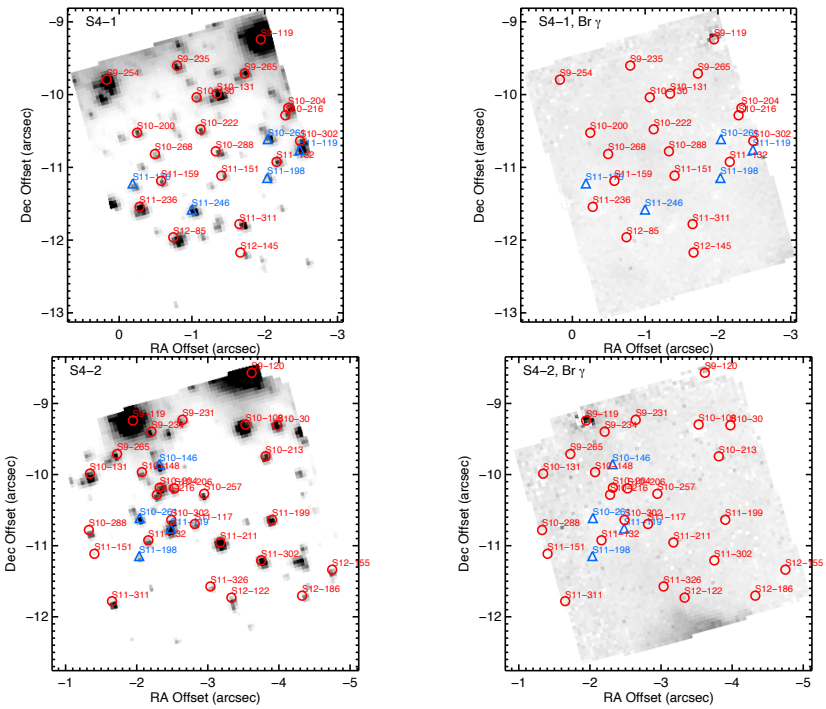

Figure 5.4: Similar to Figure 5.1, with fields S4-1 and S4-2 shown.

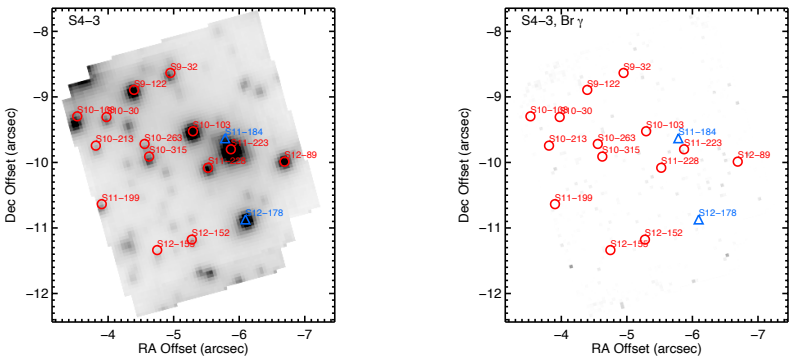

Figure 5.5: Similar to Figure 5.1, with field S4-3 shown.

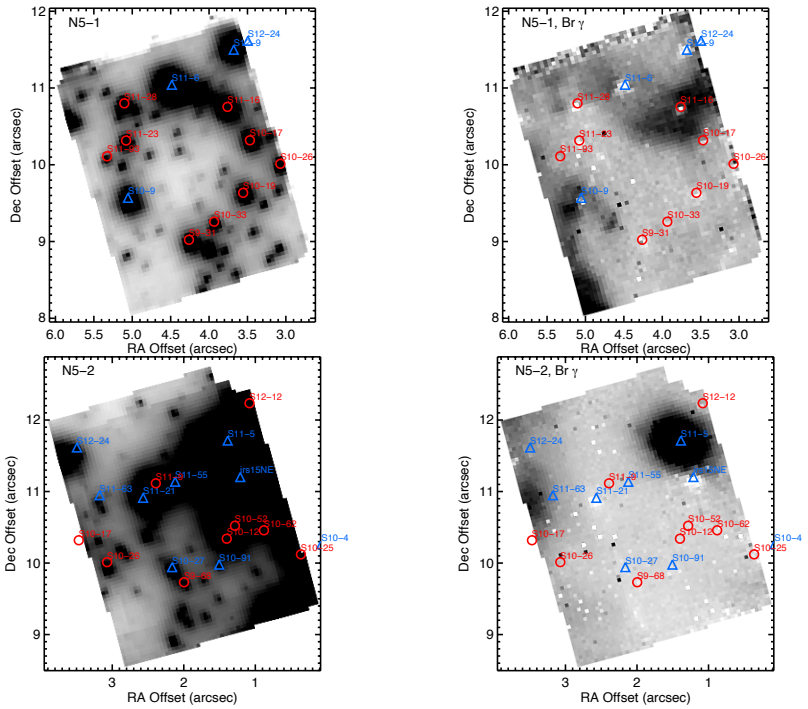

Figure 5.6: Similar to Figure 5.1, with fields N5-1 and N5-2 shown.

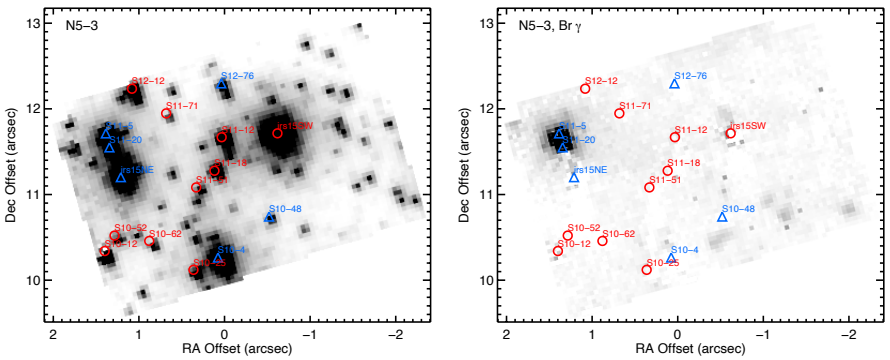

Figure 5.7: Similar to Figure 5.1, with field S4-3 shown.

Table 5.2. New OSIRIS Observations of Late-type Stars

Name	K'	R.A. Δ [a] ($''$)	Decl. Δ [a] ($''$)	R ($''$)	Epoch	Na (Å)	σ_{Na} (Å)	N_{obs}	S/N	Field
S10-17	13.6	3.44	10.30	10.86	2016.55	3.68	1.07	8	35	N5-1
S10-19	13.6	3.56	9.62	10.26	2016.55	5.57	0.05	8	31	N5-1
S10-33	14.6	3.95	9.22	10.03	2016.55	2.87	0.44	8	36	N5-1
S11-16	13.2	3.72	10.71	11.34	2016.55	4.44	0.56	8	29	N5-1
S11-23	13.6	5.07	10.34	11.51	2016.55	3.26	0.46	8	47	N5-1
S11-28	13.9	5.09	10.83	11.96	2016.55	2.8	0.93	8	52	N5-1
S11-93	15.4	5.36	10.12	11.45	2016.55	12.37	14.72	8	19	N5-1
S9-31	13.9	4.30	9.01	9.98	2016.55	4.18	0.99	8	57	N5-1
S10-12	13.3	1.43	10.29	10.39	2016.56	3.25	0.05	5	46	N5-2
S10-17	13.6	3.44	10.30	10.86	2016.55	9.92	12.44	4	6	N5-2
S10-17	13.6	3.44	10.30	10.86	2016.56	5.24	0.33	3	48	N5-2
S11-9	12.7	2.36	11.12	11.37	2016.56	6.11	0.67	5	49	N5-2

Table 5.2 (cont'd)

Name	K'	R.A. Δ [a] ($''$)	Decl. Δ [a] ($''$)	R ($''$)	Epoch	Na (Å)	σ_{Na} (Å)	N_{obs}	S/N	Field
S9-68	15.2	1.97	9.76	9.95	2016.56	4.59	2.38	5	20	N5-2
irs15SW	10.7	-0.60	11.70	11.72	2013.37	5.56	0.39	3	37	N5-3
S3-134	13.7	-1.39	-3.01	3.32	2019.40	4.91	0.3	5	15	S2-2
S3-162	14.5	-0.05	-3.41	3.41	2019.40	-8.82	4.37	3	15	S2-2
S3-178	12.8	-0.51	-3.39	3.43	2019.40	6.4	0.43	5	55	S2-2
S3-22	11.0	-0.34	-3.21	3.23	2019.40	5.39	0.15	5	68	S2-2
S3-88	14.1	-0.85	-3.00	3.12	2019.40	3.59	0.4	5	37	S2-2
S4-158	13.9	-0.86	-4.33	4.42	2019.40	3.51	0.2	5	30	S2-2
S4-170	14.0	-0.57	-4.41	4.45	2019.40	2.77	0.78	5	17	S2-2
S4-197	14.0	-2.55	-3.71	4.50	2019.40	6.32	...	1	25	S2-2
S4-22	15.1	-2.36	-3.30	4.06	2019.40	2.74	...	2	19	S2-2
S4-236	14.4	-1.91	-4.22	4.63	2019.40	4.15	1.25	5	18	S2-2

Table 5.2 (cont'd)

Name	K'	R.A. Δ [a] ($''$)	Decl. Δ [a] ($''$)	R ($''$)	Epoch	Na (Å)	σ_{Na} (Å)	N_{obs}	S/N	Field
S4-344	12.5	-1.43	-4.72	4.93	2019.40	5.35	0.09	5	67	S2-2
S4-40	15.5	-1.97	-3.61	4.11	2019.40	5.26	3.2	5	18	S2-2
S4-86	15.1	-0.66	-4.12	4.17	2019.40	4.02	0.73	5	19	S2-2
S4-97	15.4	-0.95	-4.12	4.22	2019.40	0.46	2.37	5	9	S2-2
S5-113	15.3	-2.55	-4.80	5.43	2019.40	4.9	0.58	4	21	S2-2
S5-156	15.1	-1.42	-5.45	5.63	2019.40	3.96	0.51	5	31	S2-2
S5-205	13.9	-0.91	-5.81	5.88	2019.40	3.84	0.44	4	54	S2-2
S5-71	13.7	-1.75	-4.94	5.24	2019.40	4.54	0.31	5	41	S2-2
S5-89	10.8	-0.79	-5.25	5.31	2019.40	5.8	0.13	5	66	S2-2
S5-95	13.3	-1.94	-4.99	5.36	2019.40	5.1	0.07	5	62	S2-2
S6-8	15.5	-0.76	-6.01	6.05	2019.40	4.03	1.44	3	15	S2-2
irs2	10.6	-3.70	-4.71	5.99	2019.40	5.5	0.15	5	61	S2-3

Table 5.2 (cont'd)

Name	K'	R.A. Δ [a] ($''$)	Decl. Δ [a] ($''$)	R ($''$)	Epoch	Na (Å)	σ_{Na} (Å)	N_{obs}	S/N	Field
S4-105	15.4	-2.82	-3.18	4.25	2019.40	22.44	1.51	5	4	S2-3
S4-197	14.0	-2.55	-3.71	4.50	2019.40	2.84	0.95	3	47	S2-3
S4-207	11.3	-4.05	-2.08	4.55	2019.40	5.18	0.04	5	90	S2-3
S4-22	15.1	-2.36	-3.30	4.06	2019.40	4.52	...	1	18	S2-3
S5-12	14.7	-4.28	-2.63	5.02	2019.40	3.67	0.58	5	13	S2-3
S5-123	15.9	-4.34	-3.30	5.45	2019.40	3.08	0.78	5	42	S2-3
S5-150	15.8	-3.91	-4.02	5.61	2019.40	2.81	9.1	5	6	S2-3
S5-174	14.3	-4.16	-3.94	5.73	2019.40	5.51	0.99	5	22	S2-3
S5-199	14.0	-4.20	-4.08	5.86	2019.40	5.53	0.15	5	24	S2-3
S6-14	15.1	-3.24	-5.16	6.09	2019.40	1.49	0.93	5	23	S2-3
S6-341	15.4	-4.12	-4.44	6.06	2019.40	3.52	1.42	5	27	S2-3
S6-35	12.4	-4.91	-3.96	6.31	2019.40	5.46	0.2	4	51	S2-3

Table 5.2 (cont'd)

Name	K'	R.A. Δ [a] ($''$)	Decl. Δ [a] ($''$)	R ($''$)	Epoch	Na (Å)	σ_{Na} (Å)	N_{obs}	S/N	Field
S6-36	15.6	-4.60	-4.28	6.28	2019.40	4.0	0.63	5	30	S2-3
S6-62	14.6	-4.70	-4.60	6.58	2019.40	5.27	0.21	5	65	S2-3
S6-66	13.9	-4.71	-4.66	6.63	2019.40	5.16	0.34	5	63	S2-3
irs14NE	9.8	0.91	-8.14	8.20	2019.47	4.87	0.05	5	87	S3-1
irs14SW	10.1	-0.21	-8.92	8.92	2019.47	5.59	0.16	5	73	S3-1
S6-102	13.8	0.86	-6.84	6.89	2019.47	3.93	0.74	5	14	S3-1
S6-109	14.3	0.26	-6.56	6.57	2019.47	4.24	1.12	5	24	S3-1
S7-11	11.9	-0.59	-7.39	7.42	2019.47	4.96	0.38	5	45	S3-1
S7-15	12.6	-0.17	-7.25	7.25	2019.47	5.25	0.78	5	42	S3-1
irs12N	9.7	-3.27	-6.92	7.65	2014.54	3.91	0.23	5	53	S3-2
S6-267	15.4	-2.09	-6.65	6.97	2014.54	3.95	0.58	6	14	S3-2
S6-31	13.9	-2.12	-5.85	6.22	2014.54	7.02	0.4	5	27	S3-2

Table 5.2 (cont'd)

Name	K'	R.A. Δ [a] ($''$)	Decl. Δ [a] ($''$)	R ($''$)	Epoch	Na (Å)	σ_{Na} (Å)	N_{obs}	S/N	Field
S6-37	14.8	-2.31	-5.87	6.30	2014.54	3.86	0.29	5	18	S3-2
S6-49	14.3	-2.85	-5.77	6.44	2014.54	3.68	0.68	6	40	S3-2
S6-70	14.5	-2.80	-6.15	6.76	2014.54	4.19	0.23	6	48	S3-2
S6-88	11.8	-1.80	-6.41	6.66	2014.54	5.56	0.38	6	43	S3-2
S7-101	15.1	-1.48	-7.76	7.90	2014.54	5.78	...	2	12	S3-2
S7-29	14.1	-3.66	-6.38	7.36	2014.54	3.71	0.51	3	31	S3-2
S7-94	14.1	-2.43	-6.83	7.25	2014.54	4.55	1.05	6	31	S3-2
S8-102	15.2	-2.64	-8.34	8.75	2014.54	4.0	0.56	6	25	S3-2
S8-157	15.7	-2.26	-7.92	8.23	2014.54	4.73	1.44	6	25	S3-2
S8-163	15.2	-2.40	-7.92	8.28	2014.54	4.46	1.67	6	29	S3-2
S8-33	14.1	-3.24	-7.92	8.55	2014.54	2.93	0.83	6	30	S3-2
S8-49	14.8	-3.67	-7.70	8.53	2014.54	3.97	1.14	5	29	S3-2

Table 5.2 (cont'd)

Name	K'	R.A. Δ [a] ($''$)	Decl. Δ [a] ($''$)	R ($''$)	Epoch	Na (Å)	σ_{Na} (Å)	N_{obs}	S/N	Field
S9-120	11.9	-3.63	-8.58	9.32	2014.54	3.54	...	2	44	S3-2
S9-166	15.4	-2.76	-8.75	9.18	2014.54	5.17	...	2	11	S3-2
S9-3	10.6	-3.41	-8.51	9.17	2014.54	4.31	...	2	37	S3-2
S8-38	14.5	-4.26	-7.14	8.31	2019.52	3.22	1.65	4	28	S3-3
S8-39	14.5	-5.20	-6.52	8.34	2019.52	5.74	1.09	4	22	S3-3
S10-130	15.4	-1.05	-10.03	10.09	2014.38	4.82	0.57	6	33	S4-1
S10-131	13.9	-1.36	-10.00	10.09	2014.38	4.52	0.36	6	48	S4-1
S10-200	15.2	-0.23	-10.47	10.47	2014.38	3.25	0.68	6	19	S4-1
S10-268	15.4	-0.47	-10.79	10.80	2014.38	4.53	0.91	6	28	S4-1
S10-288	14.9	-1.36	-10.79	10.87	2014.38	6.27	0.91	6	48	S4-1
S11-132	14.9	-2.13	-10.91	11.11	2014.38	3.76	0.36	4	33	S4-1
S11-151	15.5	-1.39	-11.07	11.16	2014.38	4.81	1.0	6	24	S4-1

Table 5.2 (cont'd)

Name	K'	R.A. Δ [a] ($''$)	Decl. Δ [a] ($''$)	R ($''$)	Epoch	Na (Å)	σ_{Na} (Å)	N_{obs}	S/N	Field
S11-159	15.2	-0.53	-11.16	11.18	2014.38	4.46	1.33	6	24	S4-1
S11-236	13.9	-0.24	-11.52	11.52	2014.38	5.24	0.47	4	33	S4-1
S11-311	14.5	-1.65	-11.76	11.88	2014.38	6.04	0.44	6	45	S4-1
S12-145	15.3	-1.67	-12.20	12.31	2014.38	5.63	1.53	6	27	S4-1
S12-85	13.8	-0.75	-12.00	12.02	2014.38	4.61	0.34	6	36	S4-1
S9-235	14.8	-0.77	-9.61	9.64	2014.38	5.7	0.22	4	34	S4-1
S9-254	12.9	0.18	-9.78	9.79	2014.38	3.41	...	2	48	S4-1
S9-265	14.8	-1.69	-9.69	9.83	2014.38	3.82	0.26	6	22	S4-1
S10-108	13.1	-3.49	-9.37	10.00	2014.38	1.91	0.61	5	90	S4-2
S10-148	15.3	-2.06	-9.96	10.17	2014.38	3.31	1.12	5	28	S4-2
S10-204	14.9	-2.33	-10.21	10.47	2014.38	3.75	0.47	6	33	S4-2
S10-206	15.3	-2.51	-10.17	10.48	2014.38	3.79	1.12	6	17	S4-2

Table 5.2 (cont'd)

Name	K'	R.A. Δ [a] ($''$)	Decl. Δ [a] ($''$)	R ($''$)	Epoch	Na (Å)	σ_{Na} (Å)	N_{obs}	S/N	Field
S10-213	15.1	-3.80	-9.79	10.51	2014.38	3.7	0.39	5	43	S4-2
S10-216	15.4	-2.28	-10.28	10.53	2014.38	4.94	0.41	6	23	S4-2
S10-257	14.9	-2.91	-10.29	10.69	2014.38	3.68	0.47	6	34	S4-2
S10-30	14.5	-3.95	-9.28	10.09	2014.38	4.44	0.96	4	44	S4-2
S10-302	14.9	-2.48	-10.66	10.94	2014.38	2.12	0.57	6	46	S4-2
S11-117	15.2	-2.81	-10.66	11.02	2014.38	5.89	3.77	6	22	S4-2
S11-199	14.3	-3.84	-10.63	11.30	2014.38	2.98	0.23	5	30	S4-2
S11-211	13.3	-3.15	-10.92	11.37	2014.38	4.77	0.23	6	34	S4-2
S11-302	14.5	-3.78	-11.23	11.85	2014.38	2.74	0.71	6	62	S4-2
S11-326	15.5	-3.02	-11.54	11.93	2014.38	3.66	1.24	6	14	S4-2
S12-122	15.2	-3.30	-11.76	12.21	2014.38	4.88	0.75	6	27	S4-2
S12-155	15.3	-4.69	-11.42	12.35	2014.38	4.52	...	2	30	S4-2

Table 5.2 (cont'd)

Name	K'	R.A. Δ [a] ($''$)	Decl. Δ [a] ($''$)	R ($''$)	Epoch	Na (Å)	σ_{Na} (Å)	N_{obs}	S/N	Field
S12-186	15.6	-4.37	-11.71	12.50	2014.38	2.86	0.96	4	27	S4-2
S9-119	11.1	-1.92	-9.20	9.40	2014.38	6.46	...	2	37	S4-2
S9-231	15.2	-2.64	-9.24	9.61	2014.38	4.48	1.37	6	19	S4-2
S9-234	15.3	-2.18	-9.39	9.63	2014.38	5.51	1.0	6	23	S4-2
S10-103	12.7	-5.28	-9.51	10.88	2014.43	5.57	0.43	9	34	S4-3
S10-108	13.1	-3.49	-9.37	10.00	2014.43	1.0	...	2	6	S4-3
S10-213	15.1	-3.80	-9.79	10.51	2014.43	-2.17	9.9	4	4	S4-3
S10-263	14.6	-4.58	-9.75	10.77	2014.43	6.1	4.15	9	19	S4-3
S10-30	14.5	-3.95	-9.28	10.09	2014.43	2.65	1.21	7	16	S4-3
S10-315	13.7	-4.60	-9.96	10.97	2014.43	7.01	1.58	9	26	S4-3
S11-223	11.5	-5.88	-9.83	11.45	2014.43	4.45	0.3	9	44	S4-3
S11-228	13.2	-5.51	-10.07	11.48	2014.43	4.23	1.85	9	29	S4-3

Table 5.2 (cont'd)

Name	K'	R.A. Δ [a] ($''$)	Decl. Δ [a] ($''$)	R ($''$)	Epoch	Na (Å)	σ_{Na} (Å)	N_{obs}	S/N	Field
S12-152	14.8	-5.25	-11.16	12.33	2014.43	8.92	1.67	9	4	S4-3
S12-89	12.6	-6.67	-10.02	12.03	2014.43	5.07	...	1	18	S4-3
S9-122	13.0	-4.38	-8.88	9.90	2014.43	5.65	0.62	8	32	S4-3

[a]From SgrA*

Table 5.3. New OSIRIS Observations of Early-type Stars

Name	K'	R.A. Δ [a] ($''$)	Decl. Δ [a] ($''$)	R ($''$)	Epoch	Brγ (Å)	$\sigma_{\mathrm{Br}\gamma}$ (Å)	N_{obs}	S/N	Field	v_{LSR} (km s^{-1})	σ_{vz} (km s^{-1})
S10-9	13.1	5.04	9.54	10.79	2016.55	...	...	8	37	N5-1	...	...
S11-6	12.2	4.49	11.03	11.91	2016.55	...	...	8	106	N5-1	...	...
S12-9	12.9	3.69	11.56	12.14	2016.55	...	...	8	61	N5-1	...	...
irs15NE	10.9	1.22	11.25	11.32	2016.56	...	...	5	68	N5-2	...	...
S10-27	14.2	2.18	9.97	10.20	2016.56	...	...	5	4	N5-2	...	...
S10-91	15.5	1.50	10.01	10.12	2016.56	...	...	5	5	N5-2	...	...
S11-21	13.5	2.57	10.93	11.23	2016.56	4.22	0.55	5	55	N5-2	-84.5	13.4
S11-5	11.9	1.38	11.69	11.77	2016.56	...	...	5	63	N5-2	...	...
S11-55	15.4	2.11	11.17	11.37	2016.56	...	...	5	3	N5-2	...	...
S11-63	15.5	3.15	10.90	11.35	2016.56	...	...	2	3	N5-2	...	...
S12-24	14.3	3.44	11.59	12.09	2016.56	...	...	2	19	N5-2	...	...
irs15NE	10.9	1.22	11.25	11.32	2013.37	...	...	2	24	N5-3	...	...

Table 5.3 (cont'd)

Name	K'	R.A. Δ [a] ($''$)	Decl. Δ [a] ($''$)	R ($''$)	Epoch	Brγ (Å)	$\sigma_{\mathrm{Br}\gamma}$ (Å)	N_{obs}	S/N	Field	v_{LSR} (km s^{-1})	σ_{vz} (km s^{-1})
S10-4	11.3	0.09	10.25	10.25	2013.37	...	...	2	76	N5-3	...	...
S10-48	15.2	-0.53	10.73	10.74	2013.37	8.26	11.13	3	23	N5-3	-292.5	44.8
S12-76	14.4	0.01	12.29	12.29	2013.37	4.11	1.66	3	44	N5-3	-147.5	32.0
S2-306	15.2	-0.49	-2.89	2.93	2019.40	...	...	5	31	S2-2	...	...
S3-155	15.1	-1.84	-2.83	3.38	2019.40	...	...	5	4	S2-2	...	...
S3-19	11.8	-1.55	-2.79	3.20	2019.40	...	...	5	211	S2-2	...	...
S3-208	14.4	-0.98	-3.41	3.55	2019.40	...	...	5	19	S2-2	...	...
S3-268	15.2	-2.15	-3.03	3.71	2019.40	...	...	4	21	S2-2	...	...
S3-65	15.6	-1.24	-2.80	3.06	2019.40	...	...	5	16	S2-2	...	...
S4-8	15.2	-0.45	-3.97	4.00	2019.40	...	...	5	11	S2-2	...	...
S5-180	15.5	-2.79	-5.01	5.73	2019.40	...	...	2	13	S2-2	...	...
S5-187	13.2	-1.71	-5.55	5.80	2019.40	...	...	5	122	S2-2	...	...

Table 5.3 (cont'd)

Name	K'	R.A. Δ [a] ($''$)	Decl. Δ [a] ($''$)	R ($''$)	Epoch	Brγ (Å)	$\sigma_{\mathrm{Br}\gamma}$ (Å)	N_{obs}	S/N	Field	v_{LSR} (km s^{-1})	σ_{vz} (km s^{-1})
S3-374	12.3	-2.76	-2.85	3.97	2019.40	...	...	5	76	S2-3	...	...
S5-106	15.4	-4.35	-3.20	5.40	2019.40	6.82	3.33	5	33	S2-3	-27.9	16.6
S5-180	15.5	-2.79	-5.01	5.73	2019.40	...	...	1	15	S2-3	...	...
S5-287	12.8	-3.40	-3.93	5.20	2019.40	...	...	5	71	S2-3	...	...
S5-34	13.6	-4.33	-2.74	5.13	2019.40	...	...	5	59	S2-3	...	...
S9-6	11.6	0.75	-9.33	9.36	2019.49	...	...	4	55	S3-1	...	...
S5-187	13.2	-1.71	-5.55	5.80	2014.54	...	...	2	31	S3-2	...	...
S6-44	15.1	-2.15	-6.00	6.37	2014.54	...	...	6	29	S3-2	...	...
S6-64	14.5	-3.05	-5.86	6.60	2014.54	...	...	5	49	S3-2	...	...
S8-126	12.8	-2.25	-8.56	8.85	2014.54	...	...	6	86	S3-2	...	...
S8-48	14.9	-3.34	-7.80	8.49	2014.54	...	...	6	18	S3-2	...	...
S8-5	11.2	-3.49	-7.51	8.28	2014.54	...	...	5	76	S3-2	...	...

Table 5.3 (cont'd)

Name	K'	R.A. Δ [a] ($''$)	Decl. Δ [a] ($''$)	R ($''$)	Epoch	Brγ (Å)	$\sigma_{\mathrm{Br}\gamma}$ (Å)	N_{obs}	S/N	Field	v_{LSR} (km s^{-1})	σ_{vz} (km s^{-1})
S8-54	15.1	-1.92	-8.38	8.60	2014.54	...	...	4	29	S3-2	...	...
S8-7	12.1	-3.69	-7.42	8.28	2014.54	...	...	5	59	S3-2	...	...
S6-73	12.9	-3.91	-5.57	6.80	2019.52	...	...	4	9	S3-3	...	...
S7-18	13.1	-5.53	-5.54	7.83	2019.52	...	...	2	62	S3-3	...	...
S10-261	14.6	-2.02	-10.58	10.77	2014.38	3.07	0.94	6	57	S4-1	78.6	18.8
S11-176	15.3	-0.16	-11.24	11.24	2014.38	6.44	3.59	4	13	S4-1	161.2	69.3
S11-246	14.2	-0.95	-11.56	11.59	2014.38	3.05	0.96	6	76	S4-1	115.6	18.5
S10-146	14.6	-2.34	-9.88	10.16	2014.38	...	...	6	24	S4-2	...	...
S11-119	13.9	-2.44	-10.75	11.02	2014.38	...	...	6	87	S4-2	...	...
S11-198	15.4	-2.00	-11.12	11.30	2014.38	...	...	2	7	S4-2	...	...
S11-184	13.9	-5.78	-9.67	11.26	2014.43	...	...	9	20	S4-3	...	...
S12-178	12.1	-6.08	-10.86	12.44	2014.43	...	...	9	76	S4-3	...	...

Table 5.3 (cont'd)

Name	K'	R.A. Δ [a] ($''$)	Decl. Δ [a] ($''$)	R ($''$)	Epoch	Brγ (Å)	$\sigma_{\mathrm{Br}\gamma}$ (Å)	N_{obs}	S/N	Field	v_{LSR} (km s^{-1})	σ_{vz} (km s^{-1})

[a]From SgrA*

5.5 Discussion and Conclusion

The stars reported in these GCOWS fields lie perpendicular to the plane of the young, clockwise disk (Lu et al. 2009). With these fields now observed, there is an opportunity to compare this population young stars to those of the stellar disk. The coherent, organized structure and dynamics of the disk may suggest that the disk young stars are a distinct population from these spectral typed young stars in this work. Further analysis into the motions of these stars can help answer this question.

This work also compliments other works that have spectral typed stars at the Galactic center, such as Feldmeier-Krause et al. (2017), who used the KMOS instrument on the VLT. The high angular resolution of OSIRIS compliments the seeing-limited KMOS data, which covers a large area of nuclear star cluster.

The OSIRIS fields S2-2, S2-3, S3-1, S3-2, and S3-3 cover the minispiral located just south of the SMBH. This enables the gas dynamics to be explored in greater detail. Integral fields spectrographs provide opportunities to study gas dynamics at the Galactic center (e.g. Ciurlo et al. 2019), and this additional data can contribute to our knowledge of the gas and interstellar medium.

This expansion of the GCOWS survey has provided additional coverage of 110 arcsec^2 of adaptive optics fed spectroscopy coverage to the nuclear star cluster. The addition of 169 spectral typed stars increases our understanding of the stellar demographics and provides tremendous opportunities to further our knowledge of the regions' dynamics and processes.

CHAPTER 6

Conclusions

The development of spectroscopy behind adaptive optics has revolutionized our understanding of the Galactic center stellar population and environment. Spectroscopy led to the discovery of young, massive stars within a parsec of the central black hole, raising questions about star formation and dynamics. Through continued observations, we have learned more about the stellar demographics and have begun to search for spectroscopic binaries at the Galactic center. This thesis has expanded the depth of spectroscopic binary searches to an unprecedented level through a combination of continued observations and improved methodologies for extracting and analyzing spectroscopy data.

We presented the first search for spectroscopic binary stars among the Galactic center S-stars in this thesis. We investigated S0-2, the most well-studied star of the S-star cluster, and found no significant evidence of binarity. We also placed limits on the hypothetical companion mass to be 1.6 $M_{\odot}$, which is below current detection limits. Using the same methodology as the S0-2 search but with improved spectral analysis tools, we expand the spectroscopic binary search to 28 other stars closest to the black hole. We found no significant periodic signals and placed limits on the intrinsic binary fraction of the young stars near the SMBH.

We also present an expansion of integral field spectroscopy of stars at the Galactic center. This data was taken over 6 years and reports the spectral types of 169 stars. This study improves our understanding of stellar demographics and opens up incredible potential for future studies of binarity and dynamics.

With continued observations over time, our sensitivity to binarity will improve. The

field of spectroscopic binary searches at the Galactic center is rich with potential and will play a pivotal role in understanding the stellar population and evolution of the nuclear star cluster. The expansion of spectral coverage through integral field spectroscopy will also reveal more about the stellar demographics. This in turn will open the opportunity for further spectroscopic binary searches.

APPENDIX A

Appendix

A.1 Orbital Fit for S0-2 in Chu et al. (2018)

The model for S0-2's long-term RV variation is based on a joint orbital fit of S0-2 and S0-38. We used the same S0-2 and S0-38 astrometry[1] and process as Boehle et al. (2016), S0-38 RV from (Gillessen et al. 2017), but with the S0-2 RVs from Table 2.2. It should also be noted that the impact of S0-38 is negligible for this S0-2 binary study. The resulting orbital parameters are listed in Table A.1, with all results being consistent with Boehle et al. (2016) within 1σ.

A.2 Lomb-Scargle Eccentricity Simulations

In this work, we used the Lomb-Scargle method to look for periodic signals in the S0-2 data. The Lomb-Scargle method works best at detecting sinusoidal signals, which corresponds to a circular binary system. However, as binaries become eccentric, their radial velocity curve deviates more from a perfect sine wave. Although their curves are periodic, their non-sinusoidal shapes could lead to reduced sensitivity using the Lomb-Scargle periodogram.

We explored the method's sensitivity to eccentricity by generating four sets of 100,000 simulated eccentric binary radial velocity curves. The first set of curves had $e = 0$, the second set had $e = 0.25$, the third set had $e = 0.5$ and the fourth set had $e = 0.9$. All

[1]We do not report new astrometric measurements, as additional astrometric data is not expected to significantly affect S0-2FLs RV curve.

Table A.1. Results from Orbital Fit

Model Parameter (units)	Parameter Value [a]
Black Hole Properties:	
Distance (kpc)	$7.93 \pm 0.13 \pm 0.04$
Mass (10^6 $M_\odot$)	$4.03 \pm 0.14 \pm 0.04$
X position of Sgr A* (mas)	$2.17 \pm 0.47 \pm 1.90$
Y position of Sgr A* (mas)	$-4.31 \pm 0.60 \pm 1.23$
X velocity (mas yr^{-1})	$-0.11 \pm 0.03 \pm 0.13$
Y velocity (mas yr^{-1})	$0.67 \pm 0.06 \pm 0.22$
Z velocity (km s^{-1})	$-9.99 \pm 6.25 \pm 4.28$
S0-2 Properties:	
Period (yr)	15.92 ± 0.04
Time of closest approach (yr)	2018.266 ± 0.04
Eccentricity	0.892 ± 0.002
Inclination (deg)	134.3 ± 0.3
Arguement of periapse (deg)	66.7 ± 0.5
Angle of the ascending node (deg)	228.0 ± 0.5
S0-38 Properties:	
Period (yr)	19.20 ± 0.2
Time of closest approach (yr)	2003.1 ± 0.04
Eccentricity	0.811 ± 0.004
Inclination (deg)	170 ± 2
Arguement of periapse (deg)	194 ± 160
Angle of the ascending node (deg)	79 ± 24

[a]The first error term for each best-fit value corresponds to the statistical error determined by the orbital fit. For the black hole parameters, the second error term corresponds to jackknife uncertainty from the reference frame, which were reported in Boehle et al. (2016).

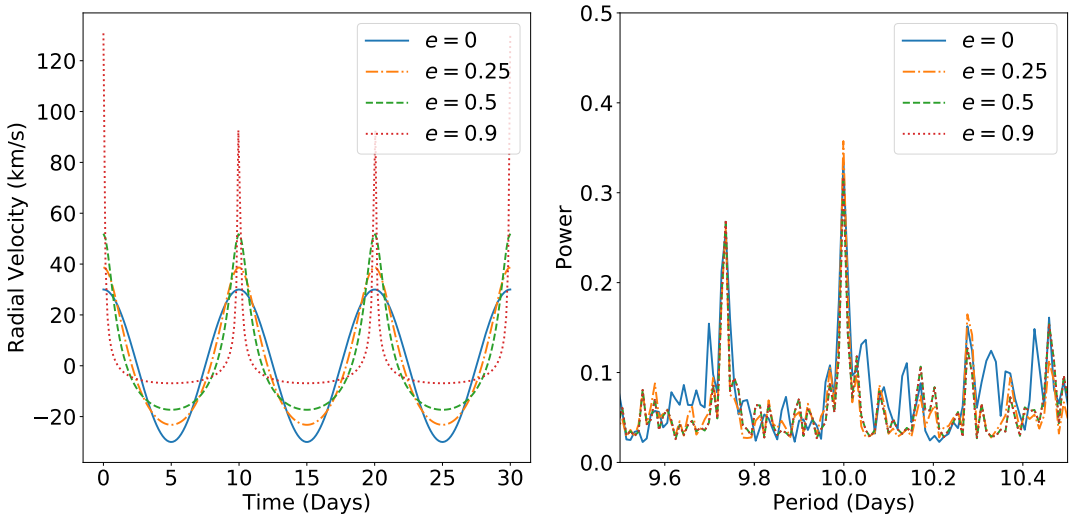

Figure A.1: Left: Sample radial velocity curves with different eccentricities. Each curve has a period of 10 days, an amplitude of 30 km $s^{-1}$and ω of 0 degrees. Right: Median Lomb-Scargle power values for each set of 100,000 simulations run for the different eccentric curves.

curves had the same period of 10 days, amplitude of 30 km s^{-1}, and ω of 0 degrees (Figure A.1). These curves were also sampled at the same times as our data. We ran each set of curves through the Lomb-Scargle analysis and took the median power values for each period. The Lomb-Scargle method successfully identified the 10 day period in the different sets of simulated curves. The median power values at the 10 days period varied by less than 0.04 between the sets. While the periodogram changes slightly with eccentricity, we find it is still a robust method to search for periodicity in the radial velocity data.

A.3 Radial Velocity Measurements and Residuals For S-star Sample

We report here the radial velocity measurements for the stars used in the binary search sample. All reported radial velocities are corrected for the local standard of rest, as discussed in Chu et al. (2018); Do et al. (2019). S0-2's radial velocity and residual were originally reported in Do et al. (2019).

Table A.2. S0-1 Radial Velocities

Epoch	MJD	$v_{\rm LSR}$ (km s^{-1})	$v_{\rm LSR}\sigma$ (km s^{-1})	Residual (km s^{-1})	Source
2003.271	52739.23	-917.0	70.0	-6.01	VLT
2004.537	53201.64	-1000.0	70.0	24.34	VLT
2004.632	53236.34	-1015.0	35.0	16.66	VLT
2005.212	53448.18	-1066.0	140.0	6.64	VLT
2005.215	53449.28	-1070.0	70.0	2.83	VLT
2005.455	53536.94	-1058.0	140.0	29.85	VLT
2005.461	53539.13	-1100.0	70.0	-11.79	VLT
2005.503	53554.50	-1053.81	21.9	36.92	Kbb
2005.769	53651.63	-1086.0	175.0	19.86	VLT
2006.204	53810.51	-1109.0	88.0	18.73	VLT
2006.305	53847.40	-1190.0	175.0	-57.7	VLT
2006.494	53916.50	-1178.91	26.27	-38.55	Kn3
2006.497	53917.50	-1215.91	25.87	-75.44	Kn3
2006.624	53963.92	-1192.0	175.0	-46.49	VLT
2007.230	54185.26	-1180.0	175.0	-14.33	VLT
2007.550	54302.14	-1161.0	175.0	12.86	VLT
2008.262	54562.20	-1115.0	53.0	71.4	VLT
2008.372	54602.50	-1212.14	19.45	-24.44	Kn3
2009.342	54956.50	-1261.5	79.79	-69.22	Kn3
2009.342	54956.52	-1209.9	22.89	-17.62	Kn3
2009.344	54957.50	-1119.87	30.53	72.41	Kn3

Table A.2 (cont'd)

Epoch	MJD	$v_{\rm LSR}$ (km s^{-1})	$v_{\rm LSR}\sigma$ (km s^{-1})	Residual (km s^{-1})	Source
2009.385	54972.37	-1087.0	123.0	105.23	VLT
2010.349	55324.53	-1110.77	53.83	75.4	Kn3
2010.354	55326.30	-1191.0	81.0	-4.88	VLT
2011.317	55678.03	-1149.0	123.0	23.08	VLT
2011.520	55752.33	-1085.33	56.64	82.96	Kn3
2012.210	56004.20	-1115.0	53.0	38.67	VLT
2012.494	56107.93	-1022.0	175.0	124.96	VLT
2012.513	56114.87	-1099.0	88.0	47.5	VLT
2012.555	56130.31	-1079.56	34.39	65.91	Kn3
2013.262	56388.45	-1035.0	44.0	92.11	VLT
2013.358	56423.53	-1054.43	25.73	70.04	Kbb
2013.655	56531.99	-1102.0	88.0	14.15	VLT
2013.726	56557.92	-975.0	105.0	139.13	VLT
2014.185	56725.57	-1093.0	88.0	7.69	VLT
2014.263	56754.06	-1120.0	88.0	-21.64	VLT
2014.502	56841.33	-1048.85	40.56	42.27	Kn3
2014.521	56848.30	-1053.0	44.0	37.54	VLT
2015.299	57132.46	-1021.0	53.0	45.25	VLT
2015.551	57224.35	-1011.97	44.15	46.23	Kn3
2016.284	57492.23	-1067.0	88.0	-32.61	VLT
2016.372	57524.51	-970.58	48.86	60.91	Kbb

Table A.2 (cont'd)

Epoch	MJD	$v_{\rm LSR}$ (km s^{-1})	$v_{\rm LSR}\sigma$ (km s^{-1})	Residual (km s^{-1})	Source
2016.519	57578.06	-1003.0	70.0	23.67	VLT
2017.374	57890.52	-977.71	25.33	20.65	Kn3
2017.546	57953.33	-988.84	37.07	3.8	Kn3
2017.568	57961.32	-968.83	29.45	23.08	Kn3
2018.311	58232.57	-959.0	24.13	8.2	Kn3
2018.390	58261.50	-957.58	17.22	6.99	Kn3
2018.554	58321.33	-917.95	29.26	41.18	Kn3
2018.579	58330.32	-937.81	18.49	20.5	Kn3
2018.609	58341.31	-966.26	22.61	-8.95	Kn3

Table A.3. S0-3 Radial Velocities

Epoch	MJD	$v_{\rm LSR}$ (km s^{-1})	$v_{\rm LSR}\sigma$ (km s^{-1})	Residual (km s^{-1})	Source
2004.535	53200.91	-553.0	50.0	62.07	VLT
2004.537	53201.64	-525.0	31.0	90.14	VLT
2004.632	53236.34	-595.0	44.0	23.75	VLT
2005.158	53428.46	-676.0	100.0	-37.35	VLT
2005.212	53448.18	-618.0	62.0	22.68	VLT
2005.215	53449.28	-605.0	50.0	35.79	VLT
2005.455	53536.94	-622.0	75.0	27.79	VLT
2005.461	53539.13	-665.0	50.0	-14.98	VLT
2005.769	53651.63	-692.0	62.0	-30.49	VLT
2006.204	53810.51	-660.0	62.0	17.63	VLT
2006.305	53847.40	-712.0	87.0	-30.64	VLT
2006.497	53917.50	-709.35	18.75	-20.93	Kn3
2006.624	53963.92	-727.0	87.0	-33.93	VLT
2007.230	54185.26	-783.0	125.0	-67.87	VLT
2007.304	54212.29	-853.0	125.0	-135.19	VLT
2007.673	54347.06	-853.0	87.0	-121.92	VLT
2008.262	54562.20	-745.0	50.0	7.02	VLT
2008.372	54602.52	-804.0	25.11	-48.08	Kn3
2008.563	54672.28	-782.88	33.64	-20.25	Kn3
2009.342	54956.50	-846.86	35.79	-57.26	Kn3
2009.344	54957.50	-803.31	26.26	-13.61	Kn3

Table A.3 (cont'd)

Epoch	MJD	$v_{\rm LSR}$ (km s^{-1})	$v_{\rm LSR}\sigma$ (km s^{-1})	Residual (km s^{-1})	Source
2009.385	54972.37	-786.0	75.0	5.09	VLT
2010.349	55324.50	-825.73	24.91	-2.14	Kn3
2010.354	55326.30	-860.0	59.0	-36.25	VLT
2011.317	55678.03	-918.0	87.0	-62.92	VLT
2011.567	55769.35	-864.0	37.0	-0.99	VLT
2012.210	56004.20	-850.0	37.0	33.0	VLT
2012.342	56052.42	-851.0	37.0	36.03	VLT
2012.444	56089.49	-885.45	28.02	4.65	Kn3
2012.494	56107.93	-888.0	37.0	3.62	VLT
2012.513	56114.87	-814.0	62.0	78.19	VLT
2012.613	56151.31	-896.41	28.29	-1.23	Kn3
2012.616	56152.33	-884.77	27.45	10.5	Kn3
2012.705	56185.00	-926.0	62.0	-28.07	VLT
2013.262	56388.45	-902.0	25.0	12.2	VLT
2013.366	56426.50	-907.03	20.46	10.14	Kn3
2013.372	56428.53	-872.39	29.11	44.94	Kn3
2013.374	56429.49	-887.62	20.69	29.78	Kn3
2013.568	56500.31	-975.47	19.97	-52.57	Kn3
2013.607	56514.29	-952.39	36.85	-28.42	Kn3
2013.609	56515.32	-1020.73	51.21	-96.68	Kn3
2013.655	56531.99	-957.0	62.0	-31.68	VLT

Table A.3 (cont'd)

Epoch	MJD	$v_{\rm LSR}$ (km s^{-1})	$v_{\rm LSR}\sigma$ (km s^{-1})	Residual (km s^{-1})	Source
2013.726	56557.92	-1003.0	37.0	-75.7	VLT
2014.185	56725.57	-892.0	37.0	47.81	VLT
2014.263	56754.06	-910.0	37.0	31.89	VLT
2014.376	56795.51	-958.61	32.26	-13.72	Kn3
2014.379	56796.51	-948.3	21.43	-3.34	Kn3
2014.502	56841.33	-1020.26	24.12	-72.09	Kn3
2014.521	56848.30	-926.0	25.0	22.67	VLT
2015.299	57132.46	-939.0	37.0	29.11	VLT
2015.551	57224.35	-977.37	38.78	-3.32	Kn3
2016.284	57492.23	-1015.0	50.0	-24.77	VLT
2016.519	57578.06	-950.0	37.0	45.06	VLT
2016.525	57580.35	-993.52	17.16	1.66	Kbb
2017.617	57979.29	-1033.11	14.65	-18.26	Kn3
2018.390	58261.50	-1002.62	17.7	23.06	Kn3
2018.554	58321.33	-1029.74	16.85	-2.14	Kn3
2018.579	58330.32	-1038.54	19.77	-10.66	Kn3
2018.609	58341.31	-1058.5	17.55	-30.29	Kn3

Table A.4. S0-5 Radial Velocities

Epoch	MJD	$v_{\rm LSR}$ (km s^{-1})	$v_{\rm LSR}\sigma$ (km s^{-1})	Residual (km s^{-1})	Source
2004.537	53201.64	632.0	115.0	48.2	VLT
2004.632	53236.34	610.0	165.0	23.84	VLT
2005.461	53539.13	604.0	132.0	-2.22	VLT
2005.503	53554.50	631.16	17.93	23.95	Kbb
2005.769	53651.63	571.0	82.0	-42.39	VLT
2006.204	53810.51	649.0	82.0	25.75	VLT
2006.494	53916.50	680.22	46.01	50.58	Kn3
2006.624	53963.92	567.0	165.0	-65.46	VLT
2007.230	54185.26	390.0	165.0	-255.3	VLT
2007.550	54302.14	786.0	165.0	134.18	VLT
2008.262	54562.20	670.0	115.0	4.29	VLT
2008.372	54602.50	652.56	43.37	-15.22	Kn3
2008.563	54672.28	699.23	29.61	27.92	Kn3
2009.342	54956.50	657.47	43.28	-27.57	Kn3
2010.354	55326.30	693.0	105.0	-8.16	VLT
2011.317	55678.03	689.0	165.0	-25.51	VLT
2011.520	55752.35	703.78	56.64	-13.26	Kn3
2012.494	56107.93	732.0	165.0	4.25	VLT
2012.513	56114.87	798.0	165.0	70.07	VLT
2013.262	56388.45	728.0	99.0	-6.36	VLT
2013.366	56426.54	748.98	25.21	13.85	Kn3

Table A.4 (cont'd)

Epoch	MJD	$v_{\rm LSR}$ (km s^{-1})	$v_{\rm LSR}\sigma$ (km s^{-1})	Residual (km s^{-1})	Source
2013.607	56514.29	757.23	23.83	20.5	Kn3
2013.655	56531.99	679.0	82.0	-58.03	VLT
2013.726	56557.92	675.0	99.0	-62.44	VLT
2014.185	56725.57	756.0	82.0	16.24	VLT
2014.263	56754.06	801.0	66.0	60.94	VLT
2014.379	56796.51	762.06	30.47	21.57	Kn3
2014.390	56800.53	729.34	53.84	-11.19	Kn3
2014.502	56841.33	757.36	29.36	16.47	Kn3
2014.521	56848.30	746.0	41.0	5.05	VLT
2015.299	57132.46	740.0	49.0	-1.88	VLT
2015.551	57224.35	687.61	55.3	-53.97	Kn3
2016.284	57492.23	805.0	99.0	66.26	VLT
2016.519	57578.06	660.0	66.0	-77.15	VLT
2017.374	57890.52	691.96	19.22	-36.18	Kn3
2017.377	57891.51	742.3	46.77	14.2	Kn3
2017.546	57953.33	687.86	94.38	-37.79	Kn3
2017.568	57961.32	711.28	22.06	-14.03	Kn3
2018.390	58261.50	680.84	22.29	-28.55	Kn3
2018.554	58321.34	691.08	23.23	-14.29	Kn3
2018.579	58330.31	707.58	18.71	2.83	Kn3
2018.609	58341.30	634.54	35.5	-69.42	Kn3

Table A.4 (cont'd)

Epoch	MJD	$v_{\rm LSR}$ (km s^{-1})	$v_{\rm LSR}\sigma$ (km s^{-1})	Residual (km s^{-1})	Source

Table A.5. S0-7 Radial Velocities

Epoch	MJD	$v_{\rm LSR}$ (km s^{-1})	$v_{\rm LSR}\sigma$ (km s^{-1})	Residual (km s^{-1})	Source
2006.494	53916.50	71.62	72.65	-33.66	Kn3
2010.341	55321.50	268.79	46.66	163.51	Kn3
2010.349	55324.50	173.21	25.67	67.93	Kn3
2011.520	55752.33	192.81	42.2	87.53	Kn3
2012.616	56152.33	210.73	30.93	105.45	Kn3
2013.366	56426.50	83.33	32.6	-21.95	Kn3
2013.372	56428.54	19.22	32.6	-86.06	Kn3
2013.568	56500.31	90.59	21.95	-14.69	Kn3
2013.607	56514.29	190.91	28.06	85.63	Kn3
2013.609	56515.32	75.82	33.8	-29.46	Kn3
2013.615	56517.31	109.57	28.12	4.29	Kn3
2014.376	56795.51	88.82	49.02	-16.46	Kn3
2014.379	56796.52	38.95	19.67	-66.33	Kn3
2014.502	56841.33	126.88	21.99	21.6	Kn3
2015.551	57224.35	156.97	63.99	51.69	Kn3
2016.525	57580.36	92.58	35.04	-12.7	Kbb
2017.374	57890.53	77.96	30.49	-27.32	Kn3
2017.546	57953.33	84.61	26.86	-20.67	Kn3
2017.568	57961.33	33.97	35.96	-71.31	Kn3
2017.618	57979.30	114.92	22.74	9.64	Kn3
2018.390	58261.50	88.01	27.17	-17.27	Kn3

Table A.5 (cont'd)

Epoch	MJD	$v_{\rm LSR}$ (km s^{-1})	$v_{\rm LSR}\sigma$ (km s^{-1})	Residual (km s^{-1})	Source
2018.554	58321.34	95.7	20.46	-9.58	Kn3
2018.609	58341.30	96.94	23.33	-8.34	Kn3

Table A.6. S0-9 Radial Velocities

Epoch	MJD	$v_{\rm LSR}$ (km s^{-1})	$v_{\rm LSR}\sigma$ (km s^{-1})	Residual (km s^{-1})	Source
2005.503	53554.50	135.34	20.5	20.87	Kbb
2008.563	54672.28	100.02	30.65	-14.45	Kn3
2009.342	54956.50	68.17	43.52	-46.3	Kn3
2010.341	55321.50	193.61	57.35	79.14	Kn3
2010.349	55324.50	162.77	39.03	48.3	Kn3
2011.520	55752.33	49.77	31.57	-64.7	Kn3
2011.545	55761.30	130.54	60.78	16.07	Kn3
2012.555	56130.31	161.89	38.86	47.42	Kn3
2013.366	56426.50	92.39	28.19	-22.08	Kn3
2013.563	56498.32	89.45	47.32	-25.02	Kn3
2013.566	56499.34	103.04	50.34	-11.43	Kn3
2013.568	56500.31	79.21	27.07	-35.26	Kn3
2013.607	56514.29	177.23	27.43	62.76	Kn3
2013.609	56515.31	142.8	37.94	28.33	Kn3
2013.615	56517.31	89.63	49.0	-24.84	Kn3
2014.374	56794.51	136.44	41.8	21.97	Kn3
2014.376	56795.51	116.73	30.38	2.26	Kn3
2014.379	56796.51	115.66	18.16	1.19	Kn3
2014.387	56799.53	127.17	44.51	12.7	Kn3
2014.390	56800.53	15.41	40.22	-99.06	Kn3
2014.502	56841.33	65.55	35.55	-48.92	Kn3

Table A.6 (cont'd)

Epoch	MJD	$v_{\rm LSR}$ (km s^{-1})	$v_{\rm LSR}\sigma$ (km s^{-1})	Residual (km s^{-1})	Source
2015.551	57224.35	96.38	26.22	-18.09	Kn3
2017.374	57890.52	106.63	20.99	-7.84	Kn3
2017.377	57891.51	95.13	54.75	-19.34	Kn3
2017.380	57892.50	109.75	61.34	-4.72	Kn3
2017.568	57961.33	76.68	18.56	-37.79	Kn3
2017.617	57979.29	85.19	11.7	-29.28	Kn3
2018.207	58194.64	270.72	59.32	156.25	Kn3
2018.311	58232.57	138.8	123.7	24.33	Kn3
2018.390	58261.49	159.79	21.32	45.32	Kn3
2018.554	58321.33	135.48	15.74	21.01	Kn3
2018.579	58330.33	175.5	27.51	61.03	Kn3
2018.609	58341.32	198.56	28.79	84.09	Kn3

Table A.7. S0-11 Radial Velocities

Epoch	MJD	$v_{\rm LSR}$ (km s^{-1})	$v_{\rm LSR}\sigma$ (km s^{-1})	Residual (km s^{-1})	Source
2006.494	53916.50	-59.2	29.39	-37.03	Kn3
2008.563	54672.28	-17.99	29.78	4.18	Kn3
2009.342	54956.50	10.27	44.73	32.44	Kn3
2010.341	55321.50	120.64	52.16	142.81	Kn3
2010.349	55324.50	-14.52	32.48	7.65	Kn3
2011.520	55752.33	21.55	42.55	43.72	Kn3
2012.444	56089.50	-81.11	84.78	-58.94	Kn3
2012.613	56151.31	-17.09	27.76	5.08	Kn3
2012.616	56152.33	-125.5	141.82	-103.33	Kn3
2013.358	56423.53	-21.44	23.37	0.73	Kbb
2013.568	56500.31	-34.88	14.09	-12.71	Kn3
2013.607	56514.29	-65.28	38.24	-43.11	Kn3
2013.609	56515.31	-0.47	62.21	21.7	Kn3
2013.615	56517.31	1.21	48.68	23.38	Kn3
2014.376	56795.51	-57.45	93.9	-35.28	Kn3
2014.379	56796.52	-34.83	36.22	-12.66	Kn3
2014.502	56841.33	-44.56	30.48	-22.39	Kn3
2015.551	57224.35	-79.15	25.14	-56.98	Kn3
2016.525	57580.36	-8.35	9.27	13.82	Kbb
2017.374	57890.52	3.71	23.72	25.88	Kn3
2017.546	57953.34	-3.68	20.12	18.49	Kn3

Table A.7 (cont'd)

Epoch	MJD	$v_{\rm LSR}$ (km s^{-1})	$v_{\rm LSR}\sigma$ (km s^{-1})	Residual (km s^{-1})	Source
2017.568	57961.33	-21.72	31.71	0.45	Kn3
2017.617	57979.29	-19.14	17.1	3.03	Kn3
2018.207	58194.64	-32.23	50.83	-10.06	Kn3
2018.311	58232.57	-70.37	80.12	-48.2	Kn3
2018.390	58261.50	-52.1	33.81	-29.93	Kn3
2018.554	58321.33	-101.53	21.28	-79.36	Kn3
2018.609	58341.31	-5.61	12.94	16.56	Kn3

Table A.8. S0-14 Radial Velocities

Epoch	MJD	$v_{\rm LSR}$ (km s^{-1})	$v_{\rm LSR}\sigma$ (km s^{-1})	Residual (km s^{-1})	Source
2006.461	53904.50	-81.94	23.77	-50.58	Kn3
2006.497	53917.50	-46.78	16.08	-15.42	Kn3
2007.384	54241.50	-4.51	20.05	26.85	Kn3
2007.545	54300.29	-21.84	18.16	9.52	Kn3
2008.372	54602.50	-48.53	14.32	-17.17	Kn3
2008.563	54672.28	-18.0	15.03	13.36	Kn3
2009.342	54956.50	-23.44	14.17	7.92	Kn3
2009.344	54957.50	-50.37	16.79	-19.01	Kn3
2010.341	55321.50	40.45	21.81	71.81	Kn3
2010.349	55324.53	0.51	17.94	31.87	Kn3
2011.520	55752.33	-58.99	17.9	-27.63	Kn3
2011.545	55761.32	-29.06	24.74	2.3	Kn3
2012.555	56130.31	-30.03	18.33	1.33	Kn3
2013.366	56426.50	-43.05	19.38	-11.69	Kn3
2013.563	56498.32	-28.11	18.23	3.25	Kn3
2013.566	56499.34	-20.11	24.08	11.25	Kn3
2013.568	56500.31	-36.82	16.3	-5.46	Kn3
2013.607	56514.28	-9.79	27.01	21.57	Kn3
2013.609	56515.31	-63.57	27.14	-32.21	Kn3
2013.615	56517.30	-26.2	19.12	5.16	Kn3
2014.374	56794.52	-50.5	19.73	-19.14	Kn3

Table A.8 (cont'd)

Epoch	MJD	$v_{\rm LSR}$ (km s^{-1})	$v_{\rm LSR}\sigma$ (km s^{-1})	Residual (km s^{-1})	Source
2014.376	56795.51	-19.41	14.02	11.95	Kn3
2014.379	56796.51	-31.23	15.24	0.13	Kn3
2014.387	56799.52	-36.95	35.67	-5.59	Kn3
2014.390	56800.53	1.65	35.77	33.01	Kn3
2014.502	56841.33	-11.36	14.63	20.0	Kn3
2015.338	57146.55	-40.43	32.27	-9.07	Kn3
2015.551	57224.35	-18.03	17.45	13.33	Kn3
2017.374	57890.51	-49.65	13.03	-18.29	Kn3
2017.377	57891.50	-37.99	14.49	-6.63	Kn3
2017.380	57892.50	-51.31	18.59	-19.95	Kn3
2017.568	57961.31	-27.66	14.3	3.7	Kn3
2017.617	57979.29	-33.71	13.53	-2.35	Kn3
2018.207	58194.64	-17.11	23.4	14.25	Kn3
2018.311	58232.57	-35.01	22.63	-3.65	Kn3
2018.363	58251.52	-15.65	19.66	15.71	NIFS
2018.390	58261.47	-32.52	16.78	-1.16	Kn3
2018.426	58274.45	-98.74	136.22	-67.38	Kn3
2018.554	58321.32	-45.37	14.67	-14.01	Kn3
2018.579	58330.32	-31.29	15.03	0.07	Kn3
2018.609	58341.31	-30.43	51.43	0.93	Kn3

Table A.9. S0-15 Radial Velocities

Epoch	MJD	$v_{\rm LSR}$ (km s^{-1})	$v_{\rm LSR}\sigma$ (km s^{-1})	Residual (km s^{-1})	Source
2006.461	53904.50	-738.47	35.56	-185.96	Kn3
2007.545	54300.29	-541.1	28.94	11.41	Kn3
2008.372	54602.50	-615.19	30.43	-62.68	Kn3
2008.563	54672.28	-632.63	36.23	-80.12	Kn3
2009.342	54956.50	-558.07	25.53	-5.56	Kn3
2009.344	54957.50	-593.78	21.78	-41.27	Kn3
2010.341	55321.50	-466.72	66.45	85.79	Kn3
2010.349	55324.53	-633.45	36.97	-80.94	Kn3
2011.520	55752.33	-582.97	24.09	-30.46	Kn3
2013.358	56423.54	-550.18	25.24	2.33	Kbb
2013.366	56426.50	-565.08	31.78	-12.57	Kn3
2013.563	56498.33	-561.36	47.25	-8.85	Kn3
2013.568	56500.31	-565.92	21.63	-13.41	Kn3
2013.607	56514.29	-610.92	34.52	-58.41	Kn3
2013.609	56515.31	-501.86	34.14	50.65	Kn3
2013.615	56517.31	-511.33	26.88	41.18	Kn3
2014.374	56794.51	-622.77	31.84	-70.26	Kn3
2014.376	56795.50	-553.31	34.76	-0.8	Kn3
2014.379	56796.51	-526.18	33.35	26.33	Kn3
2014.387	56799.52	-552.82	38.38	-0.31	Kn3
2014.390	56800.54	-482.97	53.36	69.54	Kn3

Table A.9 (cont'd)

Epoch	MJD	$v_{\rm LSR}$ (km s^{-1})	$v_{\rm LSR}\sigma$ (km s^{-1})	Residual (km s^{-1})	Source
2015.338	57146.55	-565.29	37.7	-12.78	Kn3
2015.551	57224.35	-614.41	31.97	-61.9	Kn3
2017.374	57890.53	-535.26	18.5	17.25	Kn3
2017.377	57891.50	-516.31	19.86	36.2	Kn3
2017.568	57961.32	-529.54	18.29	22.97	Kn3
2017.618	57979.30	-520.26	20.91	32.25	Kn3
2018.311	58232.57	-471.43	37.31	81.08	Kn3
2018.390	58261.50	-523.68	16.84	28.83	Kn3
2018.579	58330.31	-548.26	26.32	4.25	Kn3
2018.609	58341.31	-522.93	19.13	29.58	Kn3

Table A.10. S0-16 Radial Velocities

Epoch	MJD	$v_{\rm LSR}$ (km s^{-1})	$v_{\rm LSR}\sigma$ (km s^{-1})	Residual (km s^{-1})	Source
2004.537	53201.64	735.0	172.0	62.69	VLT
2004.632	53236.34	765.0	259.0	102.95	VLT
2005.461	53539.13	549.0	172.0	-34.32	VLT
2005.769	53651.63	605.0	216.0	46.9	VLT
2006.204	53810.51	471.0	216.0	-54.38	VLT
2007.673	54347.06	370.0	216.0	-63.83	VLT
2008.262	54562.20	324.0	194.0	-79.21	VLT
2009.385	54972.37	293.0	172.0	-58.72	VLT
2010.354	55326.30	205.0	194.0	-107.98	VLT
2011.520	55752.33	138.72	27.75	-132.9	Kn3
2012.555	56130.31	225.55	41.53	-13.21	Kn3
2012.616	56152.33	211.83	27.44	-25.11	Kn3
2013.568	56500.31	178.21	22.51	-31.14	Kn3
2014.263	56754.06	262.0	151.0	71.49	VLT
2015.299	57132.46	241.0	108.0	76.88	VLT
2015.551	57224.35	126.92	34.39	-31.07	Kn3
2016.284	57492.23	131.0	129.0	-9.66	VLT
2016.525	57580.35	110.88	23.65	-24.24	Kbb
2017.374	57890.52	138.12	15.32	21.89	Kn3
2017.568	57961.32	162.75	43.29	50.71	Kn3
2017.617	57979.29	133.93	20.8	22.94	Kn3

Table A.10 (cont'd)

Epoch	MJD	$v_{\rm LSR}$ (km s^{-1})	$v_{\rm LSR}\sigma$ (km s^{-1})	Residual (km s^{-1})	Source
2018.554	58321.33	169.11	22.67	77.74	Kn3
2018.579	58330.31	199.77	24.91	108.91	Kn3
2018.609	58341.31	115.1	29.46	24.85	Kn3

Table A.11. S0-19 Radial Velocities

Epoch	MJD	$v_{\rm LSR}$ (km s^{-1})	$v_{\rm LSR}\sigma$ (km s^{-1})	Residual (km s^{-1})	Source
2003.271	52739.23	330.0	237.0	-50.91	VLT
2004.537	53201.64	330.0	118.0	11.98	VLT
2004.632	53236.34	315.0	118.0	1.23	VLT
2005.215	53449.28	285.0	237.0	-3.82	VLT
2005.461	53539.13	330.0	189.0	51.16	VLT
2005.769	53651.63	310.0	237.0	43.2	VLT
2006.204	53810.51	349.0	118.0	98.49	VLT
2006.305	53847.40	315.0	237.0	68.15	VLT
2006.624	53963.92	279.0	237.0	43.44	VLT
2007.230	54185.26	282.0	237.0	66.88	VLT
2007.550	54302.14	319.0	237.0	114.15	VLT
2007.673	54347.06	298.0	237.0	97.02	VLT
2008.262	54562.20	243.0	272.0	59.88	VLT
2009.385	54972.37	293.0	237.0	141.47	VLT
2010.354	55326.30	104.0	144.0	-22.53	VLT
2011.317	55678.03	143.0	118.0	39.6	VLT
2012.210	56004.20	131.0	118.0	47.74	VLT
2012.342	56052.42	110.0	71.0	29.62	VLT
2012.494	56107.93	55.0	71.0	-22.09	VLT
2012.513	56114.87	70.0	118.0	-6.68	VLT
2012.616	56152.33	83.33	31.08	8.85	Kn3

Table A.11 (cont'd)

Epoch	MJD	$v_{\rm LSR}$ (km s^{-1})	$v_{\rm LSR}\sigma$ (km s^{-1})	Residual (km s^{-1})	Source
2012.705	56185.00	84.0	118.0	11.43	VLT
2013.262	56388.45	42.0	71.0	-18.94	VLT
2013.366	56426.50	42.61	15.82	-16.19	Kn3
2013.374	56429.49	58.79	32.2	0.16	Kn3
2013.568	56500.32	66.82	20.99	12.13	Kn3
2013.607	56514.29	50.58	26.2	-3.33	Kn3
2013.609	56515.31	-47.86	34.66	-101.72	Kn3
2013.615	56517.31	30.56	22.38	-23.19	Kn3
2013.655	56531.99	-35.0	166.0	-87.94	VLT
2014.263	56754.06	26.0	95.0	-14.88	VLT
2014.502	56841.33	31.31	30.78	-4.94	Kn3
2014.521	56848.30	58.0	142.0	22.12	VLT
2015.299	57132.46	89.0	118.0	67.8	VLT
2015.551	57224.35	2.12	35.83	-14.44	Kn3
2016.284	57492.23	-90.0	142.0	-93.35	VLT
2016.525	57580.36	49.15	20.86	50.05	Kbb
2017.617	57979.29	64.9	36.57	84.55	Kn3
2018.554	58321.33	32.93	43.87	68.06	Kn3

Table A.12. S0-20 Radial Velocities

Epoch	MJD	$v_{\rm LSR}$ (km s^{-1})	$v_{\rm LSR}\sigma$ (km s^{-1})	Residual (km s^{-1})	Source
2004.535	53200.91	-409.0	236.0	54.28	VLT
2004.537	53201.64	-328.0	182.0	134.91	VLT
2004.632	53236.34	-302.0	254.0	143.28	VLT
2005.215	53449.28	-260.0	214.0	69.54	VLT
2005.461	53539.13	-124.0	375.0	154.04	VLT
2006.204	53810.51	-56.0	246.0	64.85	VLT
2008.262	54562.20	351.0	325.0	110.01	VLT
2008.372	54602.51	261.15	27.69	5.57	Kn3
2009.385	54972.37	369.0	260.0	2.81	VLT
2010.354	55326.30	432.0	299.0	-5.83	VLT
2011.317	55678.03	396.0	357.0	-87.64	VLT
2012.210	56004.20	474.0	130.0	-35.02	VLT
2012.494	56107.93	597.0	227.0	82.66	VLT
2012.513	56114.87	602.0	227.0	87.34	VLT
2012.705	56185.00	594.0	227.0	76.41	VLT
2013.262	56388.45	543.0	130.0	19.49	VLT
2013.655	56531.99	594.0	227.0	68.39	VLT
2013.726	56557.92	499.0	195.0	-26.83	VLT
2014.263	56754.06	482.0	195.0	-44.06	VLT
2014.521	56848.30	492.0	146.0	-33.32	VLT
2015.299	57132.46	557.0	195.0	36.63	VLT

Table A.12 (cont'd)

Epoch	MJD	$v_{\rm LSR}$ (km s^{-1})	$v_{\rm LSR}\sigma$ (km s^{-1})	Residual (km s^{-1})	Source
2015.551	57224.35	439.46	45.21	-78.55	Kn3
2016.284	57492.23	492.0	162.0	-17.27	VLT
2016.519	57578.06	310.0	227.0	-195.96	VLT
2016.525	57580.36	432.07	45.21	-73.8	Kbb
2017.374	57890.51	487.77	42.73	-4.38	Kn3
2017.546	57953.31	393.21	72.89	-95.88	Kn3
2017.617	57979.29	460.67	27.85	-27.13	Kn3
2018.311	58232.57	484.01	42.47	9.6	Kn3
2018.390	58261.50	483.17	39.64	10.36	Kn3
2018.554	58321.33	359.35	89.31	-110.08	Kn3
2018.579	58330.30	351.06	53.36	-117.87	Kn3
2019.357	58614.54	324.76	36.07	-127.3	Kn3

Table A.13. S0-31 Radial Velocities

Epoch	MJD	$v_{\rm LSR}$ (km s^{-1})	$v_{\rm LSR}\sigma$ (km s^{-1})	Residual (km s^{-1})	Source
2006.497	53917.50	-131.74	29.68	-12.87	Kn3
2008.372	54602.50	-92.07	20.19	26.8	Kn3
2009.342	54956.50	-116.09	92.47	2.78	Kn3
2013.366	56426.50	-176.69	32.75	-57.82	Kn3
2013.568	56500.33	-90.08	20.44	28.79	Kn3
2014.379	56796.51	-201.5	44.66	-82.63	Kn3
2014.502	56841.33	-154.73	53.89	-35.86	Kn3
2015.551	57224.35	-74.39	44.52	44.48	Kn3
2017.617	57979.29	-177.62	40.9	-58.75	Kn3

Table A.14. S1-8 Radial Velocities

Epoch	MJD	$v_{\rm LSR}$ (km s^{-1})	$v_{\rm LSR}\sigma$ (km s^{-1})	Residual (km s^{-1})	Source
2006.461	53904.50	56.87	47.92	168.83	Kn3
2006.497	53917.50	-82.78	29.37	29.18	Kn3
2008.372	54602.50	-142.74	27.29	-30.78	Kn3
2008.563	54672.28	-121.41	30.01	-9.45	Kn3
2009.342	54956.50	-180.77	32.72	-68.81	Kn3
2010.341	55321.50	-89.26	50.74	22.7	Kn3
2010.349	55324.50	-100.17	37.22	11.79	Kn3
2011.520	55752.33	-130.79	33.25	-18.83	Kn3
2013.366	56426.50	-138.41	18.17	-26.45	Kn3
2014.376	56795.52	-128.51	47.57	-16.55	Kn3
2014.379	56796.52	-143.64	54.11	-31.68	Kn3
2014.502	56841.33	-115.66	20.82	-3.7	Kn3
2015.551	57224.35	-85.09	27.95	26.87	Kn3
2017.374	57890.51	-110.85	34.99	1.11	Kn3
2017.568	57961.31	-163.89	38.45	-51.93	Kn3
2017.617	57979.29	-80.38	16.57	31.58	Kn3

Table A.15. S1-33 Radial Velocities

Epoch	MJD	$v_{\rm LSR}$ (km s^{-1})	$v_{\rm LSR}\sigma$ (km s^{-1})	Residual (km s^{-1})	Source
2006.461	53904.50	43.52	23.23	17.27	Kn3
2006.497	53917.50	-29.34	35.01	-55.59	Kn3
2008.563	54672.28	8.81	19.61	-17.44	Kn3
2009.342	54956.50	15.3	14.17	-10.95	Kn3
2010.349	55324.50	22.14	61.99	-4.11	Kn3
2011.520	55752.33	41.59	24.45	15.34	Kn3
2013.366	56426.50	33.34	85.3	7.09	Kn3
2014.376	56795.50	17.08	23.59	-9.17	Kn3
2014.379	56796.51	63.94	59.26	37.69	Kn3
2014.502	56841.33	71.59	57.54	45.34	Kn3
2015.551	57224.35	13.77	20.75	-12.48	Kn3
2017.377	57891.50	56.79	44.42	30.54	Kn3
2017.380	57892.50	60.3	28.58	34.05	Kn3
2017.617	57979.29	119.0	53.06	92.75	Kn3
2018.390	58261.47	44.91	31.66	18.66	Kn3

Table A.16. S0-6 Radial Velocities

Epoch	MJD	$v_{\rm LSR}$ (km s^{-1})	$v_{\rm LSR}\sigma$ (km s^{-1})	Residual (km s^{-1})	Source
2005.503	53554.50	84.99	2.34	1.86	Kbb
2006.461	53904.50	83.54	2.89	-0.38	Kn3
2006.494	53916.50	84.42	3.52	0.47	Kn3
2007.545	54300.29	91.36	5.04	6.54	Kn3
2008.372	54602.50	81.62	3.0	-3.89	Kn3
2008.563	54672.28	80.09	3.06	-5.57	Kn3
2009.342	54956.50	90.25	2.95	3.94	Kn3
2009.344	54957.50	91.23	2.67	4.92	Kn3
2010.349	55324.53	95.22	3.58	8.08	Kn3
2011.520	55752.33	85.03	2.85	-3.08	Kn3
2011.545	55761.31	86.59	5.37	-1.54	Kn3
2012.444	56089.50	78.18	8.33	-10.7	Kn3
2012.555	56130.31	81.57	4.4	-7.4	Kn3
2012.613	56151.31	89.83	2.81	0.81	Kn3
2012.616	56152.34	94.26	4.36	5.24	Kn3
2013.358	56423.52	88.61	2.37	-1.02	Kbb
2013.366	56426.50	90.07	3.25	0.43	Kn3
2013.372	56428.54	94.37	2.55	4.72	Kn3
2013.374	56429.47	93.18	3.74	3.53	Kn3
2013.563	56498.32	86.37	3.13	-3.43	Kn3
2013.566	56499.34	88.65	4.99	-1.16	Kn3

Table A.16 (cont'd)

Epoch	MJD	$v_{\rm LSR}$ (km s^{-1})	$v_{\rm LSR}\sigma$ (km s^{-1})	Residual (km s^{-1})	Source
2013.568	56500.31	86.8	2.66	-3.01	Kn3
2013.607	56514.29	86.44	3.25	-3.4	Kn3
2013.609	56515.31	86.0	3.0	-3.84	Kn3
2013.615	56517.31	87.9	3.05	-1.95	Kn3
2014.374	56794.52	87.82	2.47	-2.66	Kn3
2014.376	56795.51	88.13	2.69	-2.35	Kn3
2014.379	56796.51	88.29	2.93	-2.19	Kn3
2014.387	56799.53	87.02	2.92	-3.47	Kn3
2014.390	56800.53	88.58	2.8	-1.91	Kn3
2014.502	56841.33	92.66	2.5	2.08	Kn3
2015.551	57224.35	83.45	2.92	-8.0	Kn3
2016.367	57522.53	95.01	2.08	2.88	Kbb
2016.369	57523.30	94.23	2.13	2.1	Kbb
2016.372	57524.50	95.44	2.13	3.31	Kbb
2017.374	57890.52	93.06	2.23	0.1	Kn3
2017.380	57892.51	92.46	2.5	-0.5	Kn3
2017.546	57953.33	93.16	2.86	0.06	Kn3
2017.568	57961.32	93.94	2.53	0.82	Kn3
2018.207	58194.64	93.65	3.72	0.0	Kn3
2018.363	58251.52	104.7	3.09	10.92	NIFS
2018.387	58260.50	100.33	2.86	6.53	NIFS

Table A.16 (cont'd)

Epoch	MJD	$v_{\rm LSR}$ (km s^{-1})	$v_{\rm LSR}\sigma$ (km s^{-1})	Residual (km s^{-1})	Source
2018.390	58261.50	91.64	2.46	-2.16	Kn3
2018.426	58274.47	90.82	4.08	-3.01	Kn3
2018.554	58321.33	93.14	2.47	-0.8	Kn3
2018.579	58330.32	92.5	2.61	-1.46	Kn3
2018.609	58341.31	90.65	2.52	-3.33	Kn3

Table A.17. S0-12 Radial Velocities

Epoch	MJD	$v_{\rm LSR}$ (km s^{-1})	$v_{\rm LSR}\sigma$ (km s^{-1})	Residual (km s^{-1})	Source
2006.461	53904.50	-38.32	6.53	0.94	Kn3
2006.494	53916.50	-39.76	5.43	-0.5	Kn3
2007.384	54241.50	-27.56	7.32	11.7	Kn3
2007.545	54300.29	-35.89	4.23	3.37	Kn3
2008.372	54602.50	-41.02	3.0	-1.76	Kn3
2008.563	54672.28	-44.38	3.62	-5.12	Kn3
2009.342	54956.50	-40.13	4.66	-0.87	Kn3
2009.344	54957.50	-40.21	3.15	-0.95	Kn3
2010.349	55324.50	-42.95	3.02	-3.69	Kn3
2011.520	55752.33	-41.24	4.39	-1.98	Kn3
2011.545	55761.31	-47.16	5.37	-7.9	Kn3
2012.555	56130.31	-37.18	4.02	2.08	Kn3
2012.616	56152.33	-24.12	5.37	15.14	Kn3
2013.358	56423.53	-39.61	2.25	-0.35	Kbb
2013.361	56424.53	-42.23	2.09	-2.97	Kbb
2013.364	56425.53	-39.95	2.22	-0.69	Kbb
2013.366	56426.50	-41.14	2.76	-1.88	Kn3
2013.372	56428.55	-31.37	3.54	7.89	Kn3
2013.374	56429.49	-33.37	3.55	5.89	Kn3
2013.563	56498.32	-39.99	3.45	-0.73	Kn3
2013.566	56499.34	-38.18	5.01	1.08	Kn3

Table A.17 (cont'd)

Epoch	MJD	$v_{\rm LSR}$ (km s^{-1})	$v_{\rm LSR}\sigma$ (km s^{-1})	Residual (km s^{-1})	Source
2013.568	56500.31	-37.77	3.2	1.49	Kn3
2013.607	56514.29	-42.99	2.66	-3.73	Kn3
2013.609	56515.31	-44.31	2.95	-5.05	Kn3
2013.615	56517.29	-43.49	3.04	-4.23	Kn3
2014.374	56794.52	-43.22	4.9	-3.96	Kn3
2014.376	56795.51	-46.91	2.72	-7.65	Kn3
2014.379	56796.51	-38.02	2.89	1.24	Kn3
2014.387	56799.52	-40.06	3.37	-0.8	Kn3
2014.390	56800.53	-41.46	3.88	-2.2	Kn3
2014.502	56841.33	-42.28	2.98	-3.02	Kn3
2015.338	57146.55	-44.71	4.69	-5.45	Kn3
2015.551	57224.35	-49.58	2.51	-10.32	Kn3
2016.528	57581.33	-38.76	2.27	0.5	Kbb
2017.374	57890.51	-35.66	2.89	3.6	Kn3
2017.377	57891.50	-37.26	3.19	2.0	Kn3
2017.380	57892.50	-39.73	3.07	-0.47	Kn3
2017.568	57961.32	-32.66	2.85	6.6	Kn3
2017.617	57979.29	-36.7	2.96	2.56	Kn3
2018.207	58194.64	-37.4	3.91	1.86	Kn3
2018.311	58232.57	-37.91	3.68	1.35	Kn3
2018.363	58251.52	-32.65	2.93	6.61	NIFS

Table A.17 (cont'd)

Epoch	MJD	$v_{\rm LSR}$ (km s^{-1})	$v_{\rm LSR}\sigma$ (km s^{-1})	Residual (km s^{-1})	Source
2018.387	58260.50	-30.11	2.74	9.15	NIFS
2018.390	58261.49	-38.75	2.51	0.51	Kn3
2018.426	58274.45	-41.06	6.33	-1.8	Kn3
2018.554	58321.33	-36.93	2.33	2.33	Kn3
2018.579	58330.32	-34.02	2.3	5.24	Kn3
2018.609	58341.31	-39.53	2.2	-0.27	Kn3

Table A.18. S0-13 Radial Velocities

Epoch	MJD	$v_{\rm LSR}$ (km s^{-1})	$v_{\rm LSR}\sigma$ (km s^{-1})	Residual (km s^{-1})	Source
2006.461	53904.50	-50.56	2.86	-5.45	Kn3
2006.494	53916.50	-44.73	2.88	0.38	Kn3
2006.497	53917.50	-46.13	2.58	-1.02	Kn3
2007.384	54241.50	-38.4	5.83	6.71	Kn3
2008.372	54602.50	-46.52	3.46	-1.41	Kn3
2008.563	54672.28	-57.29	3.48	-12.18	Kn3
2009.342	54956.50	-49.79	3.19	-4.68	Kn3
2009.344	54957.50	-40.54	3.0	4.57	Kn3
2010.349	55324.53	-48.08	3.53	-2.97	Kn3
2011.520	55752.33	-46.49	5.23	-1.38	Kn3
2011.545	55761.31	-47.16	4.52	-2.05	Kn3
2012.443	56089.48	-48.16	3.48	-3.05	Kn3
2012.555	56130.31	-35.44	4.03	9.67	Kn3
2012.613	56151.31	-44.56	3.96	0.55	Kn3
2013.358	56423.53	-48.3	2.15	-3.19	Kbb
2013.361	56424.53	-49.71	2.08	-4.6	Kbb
2013.364	56425.53	-48.58	2.1	-3.47	Kbb
2013.366	56426.50	-49.38	2.74	-4.27	Kn3
2013.372	56428.50	-42.45	3.2	2.66	Kn3
2013.563	56498.33	-45.67	3.03	-0.56	Kn3
2013.566	56499.35	-48.09	2.89	-2.98	Kn3

Table A.18 (cont'd)

Epoch	MJD	$v_{\rm LSR}$ (km s^{-1})	$v_{\rm LSR}\sigma$ (km s^{-1})	Residual (km s^{-1})	Source
2013.568	56500.32	-48.05	2.43	-2.94	Kn3
2013.607	56514.29	-45.86	2.52	-0.75	Kn3
2013.609	56515.32	-46.76	3.01	-1.65	Kn3
2013.615	56517.31	-45.65	3.07	-0.54	Kn3
2014.374	56794.52	-45.34	2.67	-0.23	Kn3
2014.376	56795.51	-47.07	3.43	-1.96	Kn3
2014.379	56796.51	-38.17	2.9	6.94	Kn3
2014.388	56799.54	-51.3	2.94	-6.19	Kn3
2014.390	56800.53	-45.28	3.1	-0.17	Kn3
2014.502	56841.33	-44.57	3.66	0.54	Kn3
2015.338	57146.56	-43.8	2.65	1.31	Kn3
2015.551	57224.35	-54.13	3.3	-9.02	Kn3
2017.374	57890.52	-41.9	2.58	3.21	Kn3
2017.377	57891.52	-40.39	2.43	4.72	Kn3
2017.380	57892.51	-41.75	2.55	3.36	Kn3
2017.546	57953.33	-44.89	2.81	0.22	Kn3
2017.568	57961.32	-43.22	2.38	1.89	Kn3
2017.617	57979.29	-44.01	2.44	1.1	Kn3
2018.207	58194.64	-33.45	3.26	11.66	Kn3
2018.311	58232.57	-48.15	2.48	-3.04	Kn3
2018.363	58251.52	-38.65	3.15	6.46	NIFS

Table A.18 (cont'd)

Epoch	MJD	$v_{\rm LSR}$ (km s^{-1})	$v_{\rm LSR}\sigma$ (km s^{-1})	Residual (km s^{-1})	Source
2018.387	58260.50	-36.02	3.29	9.09	NIFS
2018.390	58261.50	-42.93	2.23	2.18	Kn3
2018.426	58274.48	-43.16	2.73	1.95	Kn3
2018.554	58321.34	-41.82	2.31	3.29	Kn3
2018.579	58330.32	-42.51	2.17	2.6	Kn3
2018.609	58341.31	-43.99	2.31	1.12	Kn3

Table A.19. S0-17 Radial Velocities

Epoch	MJD	$v_{\rm LSR}$ (km s^{-1})	$v_{\rm LSR}\sigma$ (km s^{-1})	Residual (km s^{-1})	Source
2003.271	52739.23	864.0	242.0	47.36	VLT
2004.537	53201.64	713.0	81.0	18.74	VLT
2004.632	53236.34	705.0	100.0	19.67	VLT
2005.215	53449.28	640.0	96.0	8.61	VLT
2005.455	53536.94	605.0	180.0	-4.63	VLT
2005.461	53539.13	618.0	68.0	8.91	VLT
2005.503	53554.50	640.92	12.35	35.62	Kbb
2005.677	53618.02	647.0	141.0	57.3	VLT
2005.769	53651.63	603.0	110.0	21.49	VLT
2006.204	53810.51	547.0	99.0	3.74	VLT
2006.305	53847.40	529.0	162.0	-5.49	VLT
2006.624	53963.92	516.0	93.0	8.91	VLT
2007.550	54302.14	498.0	137.0	67.99	VLT
2007.673	54347.06	452.0	154.0	31.95	VLT
2008.262	54562.20	382.0	150.0	8.81	VLT
2008.372	54602.50	370.2	158.56	5.64	Kn3
2008.431	54623.92	405.0	180.0	45.0	VLT
2009.385	54972.37	305.0	150.0	17.27	VLT
2010.354	55326.30	240.0	120.0	22.09	VLT
2011.317	55678.03	161.0	75.0	9.08	VLT
2012.210	56004.20	95.0	90.0	1.37	VLT

Table A.19 (cont'd)

Epoch	MJD	$v_{\rm LSR}$ (km s^{-1})	$v_{\rm LSR}\sigma$ (km s^{-1})	Residual (km s^{-1})	Source
2012.342	56052.42	75.0	90.0	-10.24	VLT
2012.494	56107.93	44.0	90.0	-31.64	VLT
2012.513	56114.87	76.0	90.0	1.55	VLT
2012.616	56152.33	96.66	38.76	28.63	Kn3
2013.262	56388.45	44.0	120.0	15.7	VLT
2013.568	56500.31	4.84	10.26	-5.08	Kn3
2013.655	56531.99	-4.0	150.0	-8.78	VLT
2014.185	56725.57	-38.0	105.0	-11.82	VLT
2014.263	56754.06	-32.0	90.0	-1.34	VLT
2014.502	56841.36	-62.72	9.77	-18.41	Kn3
2014.521	56848.30	-50.0	90.0	-4.62	VLT
2015.299	57132.46	-79.0	120.0	9.66	VLT
2016.284	57492.23	-165.0	90.0	-23.93	VLT
2016.519	57578.06	-162.0	90.0	-8.79	VLT
2017.377	57891.51	-200.42	9.03	-4.07	Kn3
2017.546	57953.33	-211.63	8.95	-6.99	Kn3
2017.568	57961.32	-225.01	14.17	-19.31	Kn3
2017.617	57979.29	-207.47	3.6	0.62	Kn3
2018.311	58232.57	-222.48	5.92	18.75	Kn3
2018.390	58261.50	-255.51	7.1	-10.57	Kn3
2018.554	58321.33	-253.01	6.31	-0.43	Kn3

Table A.19 (cont'd)

Epoch	MJD	$v_{\rm LSR}$ (km s^{-1})	$v_{\rm LSR}\sigma$ (km s^{-1})	Residual (km s^{-1})	Source
2018.579	58330.32	-258.7	4.11	-4.98	Kn3
2018.609	58341.31	-249.19	5.95	5.93	Kn3

Table A.20. S0-18 Radial Velocities

Epoch	MJD	$v_{\rm LSR}$ (km s^{-1})	$v_{\rm LSR}\sigma$ (km s^{-1})	Residual (km s^{-1})	Source
2006.494	53916.50	-283.11	5.31	6.2	Kn3
2008.372	54602.50	-259.06	5.65	30.25	Kn3
2008.563	54672.28	-282.62	12.08	6.69	Kn3
2010.349	55324.50	-274.65	6.52	14.66	Kn3
2011.520	55752.33	-287.79	7.97	1.52	Kn3
2013.366	56426.50	-280.59	3.45	8.72	Kn3
2013.568	56500.31	-286.42	3.19	2.89	Kn3
2013.609	56515.31	-285.88	6.24	3.43	Kn3
2014.502	56841.33	-290.07	3.23	-0.76	Kn3
2015.551	57224.35	-296.18	3.02	-6.87	Kn3
2017.377	57891.51	-287.82	5.74	1.49	Kn3
2017.546	57953.33	-292.25	4.03	-2.94	Kn3
2017.568	57961.32	-291.23	3.63	-1.92	Kn3
2017.617	57979.29	-292.91	3.36	-3.6	Kn3
2018.390	58261.49	-287.56	4.36	1.75	Kn3
2018.554	58321.32	-295.36	3.87	-6.05	Kn3
2018.579	58330.32	-294.36	3.56	-5.05	Kn3
2018.609	58341.31	-298.58	4.11	-9.27	Kn3

Table A.21. S0-27 Radial Velocities

Epoch	MJD	$v_{\rm LSR}$ (km s^{-1})	$v_{\rm LSR}\sigma$ (km s^{-1})	Residual (km s^{-1})	Source
2006.461	53904.50	-145.47	5.92	-24.24	Kn3
2008.372	54602.50	-123.03	7.76	-1.8	Kn3
2008.563	54672.28	-149.71	41.13	-28.48	Kn3
2009.342	54956.50	-142.92	16.12	-21.69	Kn3
2010.341	55321.50	-33.33	24.0	87.9	Kn3
2011.520	55752.33	-109.66	14.9	11.57	Kn3
2011.545	55761.31	-126.67	10.62	-5.44	Kn3
2013.366	56426.50	-122.46	4.35	-1.23	Kn3
2013.568	56500.33	-125.68	4.81	-4.45	Kn3
2014.376	56795.50	-123.83	5.59	-2.6	Kn3
2014.502	56841.33	-92.15	10.61	29.08	Kn3
2015.551	57224.35	-146.64	6.78	-25.41	Kn3
2017.374	57890.51	-122.42	5.37	-1.19	Kn3
2017.377	57891.51	-125.7	11.85	-4.47	Kn3
2017.617	57979.29	-127.12	5.1	-5.89	Kn3
2018.363	58251.52	-106.49	3.43	14.74	NIFS
2018.390	58261.50	-112.91	7.24	8.32	Kn3
2018.579	58330.32	-115.02	5.64	6.21	Kn3
2018.609	58341.31	-121.44	6.59	-0.21	Kn3

Table A.22. S1-5 Radial Velocities

Epoch	MJD	$v_{\rm LSR}$ (km s^{-1})	$v_{\rm LSR}\sigma$ (km s^{-1})	Residual (km s^{-1})	Source
2006.461	53904.50	9.58	2.73	-1.62	Kn3
2006.494	53916.50	8.35	2.77	-2.85	Kn3
2007.384	54241.50	9.92	4.48	-1.28	Kn3
2008.563	54672.28	5.16	3.28	-6.04	Kn3
2009.342	54956.50	11.75	2.9	0.55	Kn3
2009.344	54957.50	13.68	2.61	2.48	Kn3
2010.349	55324.50	13.92	2.75	2.72	Kn3
2011.520	55752.33	7.53	3.55	-3.67	Kn3
2012.555	56130.31	5.25	3.72	-5.95	Kn3
2013.366	56426.50	9.74	2.78	-1.46	Kn3
2014.376	56795.50	11.7	2.36	0.5	Kn3
2014.379	56796.50	11.1	2.5	-0.1	Kn3
2014.502	56841.33	9.1	2.55	-2.1	Kn3
2015.551	57224.35	2.58	2.57	-8.62	Kn3
2017.374	57890.52	12.95	2.28	1.75	Kn3
2017.377	57891.51	10.7	2.25	-0.5	Kn3
2017.380	57892.50	10.68	2.33	-0.52	Kn3
2017.568	57961.32	13.54	2.44	2.34	Kn3
2017.617	57979.29	11.14	2.29	-0.06	Kn3
2018.311	58232.57	10.8	2.53	-0.4	Kn3
2018.363	58251.52	21.58	2.63	10.38	NIFS

Table A.22 (cont'd)

Epoch	MJD	$v_{\rm LSR}$ (km s^{-1})	$v_{\rm LSR}\sigma$ (km s^{-1})	Residual (km s^{-1})	Source
2018.387	58260.50	18.86	2.57	7.66	NIFS
2018.390	58261.48	11.39	2.26	0.19	Kn3
2018.426	58274.46	11.69	2.6	0.49	Kn3
2018.554	58321.32	11.47	2.38	0.27	Kn3
2018.579	58330.33	10.67	2.49	-0.53	Kn3
2018.609	58341.32	9.35	2.49	-1.85	Kn3

Table A.23. S1-6 Radial Velocities

Epoch	MJD	$v_{\rm LSR}$ (km s^{-1})	$v_{\rm LSR}\sigma$ (km s^{-1})	Residual (km s^{-1})	Source
2007.542	54299.29	-57.08	7.64	-15.02	Kn3
2009.342	54956.50	-44.83	8.6	-2.77	Kn3
2010.349	55324.50	-64.33	11.11	-22.27	Kn3
2011.520	55752.33	-155.33	89.51	-113.27	Kn3
2013.366	56426.50	-47.53	7.68	-5.47	Kn3
2013.563	56498.30	-43.1	7.65	-1.04	Kn3
2013.568	56500.30	-47.74	15.61	-5.68	Kn3
2013.607	56514.29	-38.12	4.46	3.94	Kn3
2013.609	56515.31	-42.27	5.23	-0.21	Kn3
2013.615	56517.31	-37.32	4.9	4.74	Kn3
2014.376	56795.50	-57.56	12.57	-15.5	Kn3
2014.379	56796.50	-44.82	8.83	-2.76	Kn3
2014.390	56800.54	-42.86	7.66	-0.8	Kn3
2014.502	56841.33	-49.2	11.43	-7.14	Kn3
2015.551	57224.35	-21.43	29.27	20.63	Kn3
2017.374	57890.54	-41.3	3.89	0.76	Kn3
2017.377	57891.50	-51.74	12.92	-9.68	Kn3
2017.568	57961.34	-46.26	5.43	-4.2	Kn3
2017.617	57979.29	-34.69	3.62	7.37	Kn3

Table A.24. S1-10 Radial Velocities

Epoch	MJD	$v_{\rm LSR}$ (km s^{-1})	$v_{\rm LSR}\sigma$ (km s^{-1})	Residual (km s^{-1})	Source
2006.461	53904.50	-33.85	5.61	-0.27	Kn3
2007.542	54299.29	-24.43	4.4	9.15	Kn3
2008.372	54602.50	-37.19	5.03	-3.61	Kn3
2008.563	54672.28	-41.3	5.14	-7.72	Kn3
2009.342	54956.50	-32.6	4.14	0.98	Kn3
2010.349	55324.50	-33.27	5.34	0.31	Kn3
2011.520	55752.33	-27.68	6.83	5.9	Kn3
2011.545	55761.31	-39.43	8.35	-5.85	Kn3
2012.555	56130.31	-19.8	22.7	13.78	Kn3
2013.366	56426.50	-32.27	4.06	1.31	Kn3
2014.376	56795.50	-40.77	2.91	-7.19	Kn3
2014.379	56796.51	-39.38	5.81	-5.8	Kn3
2014.502	56841.33	-21.1	5.36	12.48	Kn3
2015.551	57224.35	-38.35	5.42	-4.77	Kn3
2017.374	57890.53	-36.44	3.43	-2.86	Kn3
2017.377	57891.50	-41.77	13.93	-8.19	Kn3
2017.568	57961.32	-25.34	4.55	8.24	Kn3
2017.618	57979.30	-29.8	3.27	3.78	Kn3
2018.311	58232.55	-37.05	6.19	-3.47	Kn3
2018.390	58261.49	-31.6	3.83	1.98	Kn3
2018.554	58321.32	-34.4	3.42	-0.82	Kn3

Table A.24 (cont'd)

Epoch	MJD	$v_{\rm LSR}$ (km s^{-1})	$v_{\rm LSR}\sigma$ (km s^{-1})	Residual (km s^{-1})	Source
2018.609	58341.30	-29.93	7.78	3.65	Kn3

Table A.25. S1-13 Radial Velocities

Epoch	MJD	$v_{\rm LSR}$ (km s^{-1})	$v_{\rm LSR}\sigma$ (km s^{-1})	Residual (km s^{-1})	Source
2006.494	53916.50	-759.98	5.66	-10.88	Kn3
2008.563	54672.28	-762.46	6.8	-13.36	Kn3
2009.344	54957.50	-742.37	5.66	6.73	Kn3
2014.376	56795.51	-756.0	5.11	-6.9	Kn3
2014.379	56796.51	-758.97	3.91	-9.87	Kn3
2015.597	57241.33	-760.77	5.19	-11.67	Kn3
2018.363	58251.52	-738.44	2.46	10.66	NIFS

Table A.26. S1-15 Radial Velocities

Epoch	MJD	$v_{\rm LSR}$ (km s^{-1})	$v_{\rm LSR}\sigma$ (km s^{-1})	Residual (km s^{-1})	Source
2006.461	53904.50	-125.24	6.58	-4.87	Kn3
2006.494	53916.50	-140.85	13.2	-20.48	Kn3
2006.497	53917.50	-122.82	7.37	-2.45	Kn3
2007.384	54241.50	-109.09	4.21	11.28	Kn3
2007.542	54299.29	-116.81	6.18	3.56	Kn3
2007.545	54300.29	-119.26	5.05	1.11	Kn3
2008.372	54602.50	-121.24	3.14	-0.87	Kn3
2008.563	54672.28	-125.66	4.15	-5.29	Kn3
2009.342	54956.50	-109.35	3.34	11.02	Kn3
2010.349	55324.50	-115.52	3.51	4.85	Kn3
2011.520	55752.33	-123.3	3.59	-2.93	Kn3
2011.545	55761.31	-115.48	4.11	4.89	Kn3
2012.555	56130.31	-123.61	7.16	-3.24	Kn3
2013.366	56426.50	-122.56	4.98	-2.19	Kn3
2014.376	56795.50	-125.12	2.69	-4.75	Kn3
2014.379	56796.51	-120.61	3.94	-0.24	Kn3
2014.502	56841.33	-124.25	3.74	-3.88	Kn3
2015.551	57224.35	-134.19	4.08	-13.82	Kn3
2017.374	57890.53	-118.49	3.27	1.88	Kn3
2017.377	57891.50	-120.95	3.73	-0.58	Kn3
2017.380	57892.50	-119.13	3.3	1.24	Kn3

Table A.26 (cont'd)

Epoch	MJD	$v_{\rm LSR}$ (km s^{-1})	$v_{\rm LSR}\sigma$ (km s^{-1})	Residual (km s^{-1})	Source
2017.568	57961.33	-115.54	3.35	4.83	Kn3
2017.617	57979.29	-123.34	3.2	-2.97	Kn3

A.4 Orbital Fitting Methodology For Orbit S-star Sample

We also investigated potential systematic effects of orbit fitting by running numerous combinations of orbital fits for each star. Specifically, we wanted to analyze the influence of the following sets of parameters:

1. SMBH parameters
2. Offset and additive error between Keck and VLT data points
3. Mixing and correlation length

There are 7 parameters that describe mass (M_{BH}), distance (R_0), the position (x, y), and velocity (v_x, v_y, v_z) of the black hole. We wanted to ensure that changes in the black hole parameters and resulting orbital fit would not introduce a signal into the radial velocity investigations. We investigated two combinations: we left all parameters free, and we fixed all parameters to values from Do et al. (2019).

We also fit for a radial velocity offset and additive error between Keck and VLT data points in order to account for potential systematic between the radial velocity values reported from different instruments. This procedure was also conducted in the orbital fit method used in Do et al. (2019). We wanted to ensure that there was no significant offset between Keck and VLT data, because otherwise this offset would produce an artificial signal in the periodicity search. We investigated two combinations: leaving both of these parameters free, and not including them at all.

Table A.27. S1-31 Radial Velocities

Epoch	MJD	$v_{\rm LSR}$ (km s^{-1})	$v_{\rm LSR}\sigma$ (km s^{-1})	Residual (km s^{-1})	Source
2007.542	54299.29	187.8	11.39	4.92	Kn3
2008.563	54672.28	134.98	56.51	-47.9	Kn3
2009.342	54956.50	193.12	21.45	10.24	Kn3
2010.349	55324.50	183.04	8.14	0.16	Kn3
2011.520	55752.33	192.71	4.25	9.83	Kn3
2013.366	56426.50	169.48	7.05	-13.4	Kn3
2014.376	56795.51	176.71	8.88	-6.17	Kn3
2014.379	56796.52	197.53	8.93	14.65	Kn3
2014.502	56841.33	159.0	8.45	-23.88	Kn3
2015.551	57224.35	173.73	6.12	-9.15	Kn3
2017.374	57890.53	181.76	9.25	-1.12	Kn3
2017.377	57891.50	178.5	6.04	-4.38	Kn3
2017.380	57892.50	175.59	5.56	-7.29	Kn3
2017.568	57961.33	181.56	7.04	-1.32	Kn3
2017.617	57979.29	182.1	6.05	-0.78	Kn3
2018.390	58261.48	188.43	3.13	5.55	Kn3

We also account for potential correlations in the uncertainty of astrometric measurements. This involves two parameters: a correlation length scale Λ and mixing parameter p. These parameters are discussed in greater depth in Do et al. (2019) and used in orbital fits in Ciurlo et al. (2020). We investigated two combinations: fixing Λ = 20 mas (Do et al. 2019; Ciurlo et al. 2020) and keeping p free, and not including them at all.

To summarize, each of the 3 set of parameters had two combination of fits. This meant that it was possible to have 8 different permutations of all of the set combinations. We fit 8 different fit combinations for each of the stars in our orbit sample and used Bayesian information criteria to investigate the importance of each parameter set, as done in Do et al. (2019). Generally, free black hole parameters were favored, but the black hole parameters were not well constrained. A more detailed investigation into these parameter values is beyond the scope of this work. The offset and additive error were not favored. Finally, a fixed Λ and fitting for p were favored.

Ultimately, we found that the different orbital fits did not effect the radial velocity models. We concluded that we would do the following for the different orbital fits for each star: fix the black hole parameters to those reported in Do et al. (2019); not include an instrumental offset and additive error; include a fixed Λ and fit for p.

Bibliography

Abbott, B. P., R. Abbott, T. D. Abbott, M. R. Abernathy, F. Acernese, K. Ackley, C. Adams, T. Adams, P. Addesso, R. X. Adhikari, V. B. Adya, C. Affeldt, M. Agathos, K. Agatsuma, N. Aggarwal, O. D. Aguiar, L. Aiello, A. Ain, P. Ajith, B. Allen, A. Allocca, P. A. Altin, S. B. Anderson, W. G. Anderson, K. Arai, M. A. Arain, M. C. Araya, C. C. Arceneaux, J. S. Areeda, N. Arnaud, K. G. Arun, S. Ascenzi, G. Ashton, M. Ast, S. M. Aston, P. Astone, P. Aufmuth, C. Aulbert, S. Babak, P. Bacon, M. K. M. Bader, P. T. Baker, F. Baldaccini, G. Ballardin, S. W. Ballmer, J. C. Barayoga, S. E. Barclay, B. C. Barish, D. Barker, F. Barone, B. Barr, L. Barsotti, M. Barsuglia, D. Barta, J. Bartlett, M. A. Barton, I. Bartos, R. Bassiri, A. Basti, J. C. Batch, C. Baune, V. Bavigadda, M. Bazzan, B. Behnke, M. Bejger, C. Belczynski, A. S. Bell, C. J. Bell, B. K. Berger, J. Bergman, G. Bergmann, C. P. L. Berry, D. Bersanetti, A. Bertolini, J. Betzwieser, S. Bhagwat, R. Bhandare, I. A. Bilenko, G. Billingsley, J. Birch, R. Birney, O. Birnholtz, S. Biscans, A. Bisht, M. Bitossi, C. Biwer, M. A. Bizouard, J. K. Blackburn, C. D. Blair, D. G. Blair, R. M. Blair, S. Bloemen, O. Bock, T. P. Bodiya, M. Boer, G. Bogaert, C. Bogan, A. Bohe, P. Bojtos, C. Bond, F. Bondu, R. Bonnand, B. A. Boom, R. Bork, V. Boschi, S. Bose, Y. Bouffanais, A. Bozzi, C. Bradaschia, P. R. Brady, V. B. Braginsky, M. Branchesi, J. E. Brau, T. Briant, A. Brillet, M. Brinkmann, V. Brisson, P. Brockill, A. F. Brooks, D. A. Brown, D. D. Brown, N. M. Brown, C. C. Buchanan, A. Buikema, T. Bulik, H. J. Bulten, A. Buonanno, D. Buskulic, C. Buy, R. L. Byer, M. Cabero, L. Cadonati, G. Cagnoli, C. Cahillane, J. C. Bustillo, T. Callister, E. Calloni, J. B. Camp, K. C. Cannon, J. Cao, C. D. Capano, E. Capocasa, F. Carbognani, S. Caride, J. C. Diaz, C. Casentini, S. Caudill, M. Cavaglià, F. Cavalier, R. Cavalieri, G. Cella, C. B. Cepeda, L. C. Baiardi, G. Cerretani, E. Cesarini, R. Chakraborty, T. Chalermsongsak, S. J. Chamberlin, M. Chan, S. Chao, P. Charlton, E. Chassande-Mottin, H. Y. Chen, Y. Chen, C. Cheng, A. Chincarini, A. Chiummo, H. S. Cho, M. Cho, J. H. Chow, N. Christensen, Q. Chu, S. Chua, S. Chung, G. Ciani, F. Clara, J. A. Clark, F. Cleva,

E. Coccia, P.-F. Cohadon, A. Colla, C. G. Collette, L. Cominsky, M. Constancio, A. Conte, L. Conti, D. Cook, T. R. Corbitt, N. Cornish, A. Corsi, S. Cortese, C. A. Costa, M. W. Coughlin, S. B. Coughlin, J.-P. Coulon, S. T. Countryman, P. Couvares, E. E. Cowan, D. M. Coward, M. J. Cowart, D. C. Coyne, R. Coyne, K. Craig, J. D. E. Creighton, T. D. Creighton, J. Cripe, S. G. Crowder, A. M. Cruise, A. Cumming, L. Cunningham, E. Cuoco, T. D. Canton, S. L. Danilishin, S. D'Antonio, K. Danzmann, N. S. Darman, C. F. Da Silva Costa, V. Dattilo, I. Dave, H. P. Daveloza, M. Davier, G. S. Davies, E. J. Daw, R. Day, S. De, D. DeBra, G. Debreczeni, J. Degallaix, M. De Laurentis, S. Deléglise, W. Del Pozzo, T. Denker, T. Dent, H. Dereli, V. Dergachev, R. T. DeRosa, R. De Rosa, R. DeSalvo, S. Dhurandhar, M. C. Díaz, L. Di Fiore, M. Di Giovanni, A. Di Lieto, S. Di Pace, I. Di Palma, A. Di Virgilio, G. Dojcinoski, V. Dolique, F. Donovan, K. L. Dooley, S. Doravari, R. Douglas, T. P. Downes, M. Drago, R. W. P. Drever, J. C. Driggers, Z. Du, M. Ducrot, S. E. Dwyer, T. B. Edo, M. C. Edwards, A. Effler, H.-B. Eggenstein, P. Ehrens, J. Eichholz, S. S. Eikenberry, W. Engels, R. C. Essick, T. Etzel, M. Evans, T. M. Evans, R. Everett, M. Factourovich, V. Fafone, H. Fair, S. Fairhurst, X. Fan, Q. Fang, S. Farinon, B. Farr, W. M. Farr, M. Favata, M. Fays, H. Fehrmann, M. M. Fejer, D. Feldbaum, I. Ferrante, E. C. Ferreira, F. Ferrini, F. Fidecaro, L. S. Finn, I. Fiori, D. Fiorucci, R. P. Fisher, R. Flaminio, M. Fletcher, H. Fong, J.-D. Fournier, S. Franco, S. Frasca, F. Frasconi, M. Frede, Z. Frei, A. Freise, R. Frey, V. Frey, T. T. Fricke, P. Fritschel, V. V. Frolov, P. Fulda, M. Fyffe, H. A. G. Gabbard, J. R. Gair, L. Gammaitoni, S. G. Gaonkar, F. Garufi, A. Gatto, G. Gaur, N. Gehrels, G. Gemme, B. Gendre, E. Genin, A. Gennai, J. George, L. Gergely, V. Germain, A. Ghosh, A. Ghosh, S. Ghosh, J. A. Giaime, K. D. Giardina, A. Giazotto, K. Gill, A. Glaefke, J. R. Gleason, E. Goetz, R. Goetz, L. Gondan, G. González, J. M. G. Castro, A. Gopakumar, N. A. Gordon, M. L. Gorodetsky, S. E. Gossan, M. Gosselin, R. Gouaty, C. Graef, P. B. Graff, M. Granata, A. Grant, S. Gras, C. Gray, G. Greco, A. C. Green, R. J. S. Greenhalgh, P. Groot, H. Grote, S. Grunewald, G. M. Guidi, X. Guo, A. Gupta, M. K. Gupta, K. E. Gushwa, E. K. Gustafson, R. Gustafson, J. J. Hacker, B. R. Hall, E. D. Hall, G. Hammond,

M. Haney, M. M. Hanke, J. Hanks, C. Hanna, M. D. Hannam, J. Hanson, T. Hardwick, J. Harms, G. M. Harry, I. W. Harry, M. J. Hart, M. T. Hartman, C.-J. Haster, K. Haughian, J. Healy, J. Heefner, A. Heidmann, M. C. Heintze, G. Heinzel, H. Heitmann, P. Hello, G. Hemming, M. Hendry, I. S. Heng, J. Hennig, A. W. Heptonstall, M. Heurs, S. Hild, D. Hoak, K. A. Hodge, D. Hofman, S. E. Hollitt, K. Holt, D. E. Holz, P. Hopkins, D. J. Hosken, J. Hough, E. A. Houston, E. J. Howell, Y. M. Hu, S. Huang, E. A. Huerta, D. Huet, B. Hughey, S. Husa, S. H. Huttner, T. Huynh-Dinh, A. Idrisy, N. Indik, D. R. Ingram, R. Inta, H. N. Isa, J.-M. Isac, M. Isi, G. Islas, T. Isogai, B. R. Iyer, K. Izumi, M. B. Jacobson, T. Jacqmin, H. Jang, K. Jani, P. Jaranowski, S. Jawahar, F. Jiménez-Forteza, W. W. Johnson, N. K. Johnson-McDaniel, D. I. Jones, R. Jones, R. J. G. Jonker, L. Ju, K. Haris, C. V. Kalaghatgi, V. Kalogera, S. Kandhasamy, G. Kang, J. B. Kanner, S. Karki, M. Kasprzack, E. Katsavounidis, W. Katzman, S. Kaufer, T. Kaur, K. Kawabe, F. Kawazoe, F. Kéfélian, M. S. Kehl, D. Keitel, D. B. Kelley, W. Kells, R. Kennedy, D. G. Keppel, J. S. Key, A. Khalaidovski, F. Y. Khalili, I. Khan, S. Khan, Z. Khan, E. A. Khazanov, N. Kijbunchoo, C. Kim, J. Kim, K. Kim, N.-G. Kim, N. Kim, Y.-M. Kim, E. J. King, P. J. King, D. L. Kinzel, J. S. Kissel, L. Kleybolte, S. Klimenko, S. M. Koehlenbeck, K. Kokeyama, S. Koley, V. Kondrashov, A. Kontos, S. Koranda, M. Korobko, W. Z. Korth, I. Kowalska, D. B. Kozak, V. Kringel, B. Krishnan, A. Królak, C. Krueger, G. Kuehn, P. Kumar, R. Kumar, L. Kuo, A. Kutynia, P. Kwee, B. D. Lackey, M. Landry, J. Lange, B. Lantz, P. D. Lasky, A. Lazzarini, C. Lazzaro, P. Leaci, S. Leavey, E. O. Lebigot, C. H. Lee, H. K. Lee, H. M. Lee, K. Lee, A. Lenon, M. Leonardi, J. R. Leong, N. Leroy, N. Letendre, Y. Levin, B. M. Levine, T. G. F. Li, A. Libson, T. B. Littenberg, N. A. Lockerbie, J. Logue, A. L. Lombardi, L. T. London, J. E. Lord, M. Lorenzini, V. Loriette, M. Lormand, G. Losurdo, J. D. Lough, C. O. Lousto, G. Lovelace, H. Lück, A. P. Lundgren, J. Luo, R. Lynch, Y. Ma, T. MacDonald, B. Machenschalk, M. MacInnis, D. M. Macleod, F. Magaña Sandoval, R. M. Magee, M. Mageswaran, E. Majorana, I. Maksimovic, V. Malvezzi, N. Man, I. Mandel, V. Mandic, V. Mangano, G. L. Mansell, M. Manske, M. Mantovani, F. Marchesoni, F. Marion, S. Márka,

Z. Márka, A. S. Markosyan, E. Maros, F. Martelli, L. Martellini, I. W. Martin, R. M. Martin, D. V. Martynov, J. N. Marx, K. Mason, A. Masserot, T. J. Massinger, M. Masso-Reid, F. Matichard, L. Matone, N. Mavalvala, N. Mazumder, G. Mazzolo, R. McCarthy, D. E. McClelland, S. McCormick, S. C. McGuire, G. McIntyre, J. McIver, D. J. McManus, S. T. McWilliams, D. Meacher, G. D. Meadors, J. Meidam, A. Melatos, G. Mendell, D. Mendoza-Gandara, R. A. Mercer, E. Merilh, M. Merzougui, S. Meshkov, C. Messenger, C. Messick, P. M. Meyers, F. Mezzani, H. Miao, C. Michel, H. Middleton, E. E. Mikhailov, L. Milano, J. Miller, M. Millhouse, Y. Minenkov, J. Ming, S. Mirshekari, C. Mishra, S. Mitra, V. P. Mitrofanov, G. Mitselmakher, R. Mittleman, A. Moggi, M. Mohan, S. R. P. Mohapatra, M. Montani, B. C. Moore, C. J. Moore, D. Moraru, G. Moreno, S. R. Morriss, K. Mossavi, B. Mours, C. M. Mow-Lowry, C. L. Mueller, G. Mueller, A. W. Muir, A. Mukherjee, D. Mukherjee, S. Mukherjee, N. Mukund, A. Mullavey, J. Munch, D. J. Murphy, P. G. Murray, A. Mytidis, I. Nardecchia, L. Naticchioni, R. K. Nayak, V. Necula, K. Nedkova, G. Nelemans, M. Neri, A. Neunzert, G. Newton, T. T. Nguyen, A. B. Nielsen, S. Nissanke, A. Nitz, F. Nocera, D. Nolting, M. E. N. Normandin, L. K. Nuttall, J. Oberling, E. Ochsner, J. O'Dell, E. Oelker, G. H. Ogin, J. J. Oh, S. H. Oh, F. Ohme, M. Oliver, P. Oppermann, R. J. Oram, B. O'Reilly, R. O'Shaughnessy, C. D. Ott, D. J. Ottaway, R. S. Ottens, H. Overmier, B. J. Owen, A. Pai, S. A. Pai, J. R. Palamos, O. Palashov, C. Palomba, A. Pal-Singh, H. Pan, Y. Pan, C. Pankow, F. Pannarale, B. C. Pant, F. Paoletti, A. Paoli, M. A. Papa, H. R. Paris, W. Parker, D. Pascucci, A. Pasqualetti, R. Passaquieti, D. Passuello, B. Patricelli, Z. Patrick, B. L. Pearlstone, M. Pedraza, R. Pedurand, L. Pekowsky, A. Pele, S. Penn, A. Perreca, H. P. Pfeiffer, M. Phelps, O. Piccinni, M. Pichot, M. Pickenpack, F. Piergiovanni, V. Pierro, G. Pillant, L. Pinard, I. M. Pinto, M. Pitkin, J. H. Poeld, R. Poggiani, P. Popolizio, A. Post, J. Powell, J. Prasad, V. Predoi, S. S. Premachandra, T. Prestegard, L. R. Price, M. Prijatelj, M. Principe, S. Privitera, R. Prix, G. A. Prodi, L. Prokhorov, O. Puncken, M. Punturo, P. Puppo, M. Pürrer, H. Qi, J. Qin, V. Quetschke, E. A. Quintero, R. Quitzow-James, F. J. Raab, D. S. Rabeling, H. Radkins, P. Raffai,

S. Raja, M. Rakhmanov, C. R. Ramet, P. Rapagnani, V. Raymond, M. Razzano, V. Re, J. Read, C. M. Reed, T. Regimbau, L. Rei, S. Reid, D. H. Reitze, H. Rew, S. D. Reyes, F. Ricci, K. Riles, N. A. Robertson, R. Robie, F. Robinet, A. Rocchi, L. Rolland, J. G. Rollins, V. J. Roma, J. D. Romano, R. Romano, G. Romanov, J. H. Romie, D. Rosińska, S. Rowan, A. Rüdiger, P. Ruggi, K. Ryan, S. Sachdev, T. Sadecki, L. Sadeghian, L. Salconi, M. Saleem, F. Salemi, A. Samajdar, L. Sammut, L. M. Sampson, E. J. Sanchez, V. Sandberg, B. Sandeen, G. H. Sanders, J. R. Sanders, B. Sassolas, B. S. Sathyaprakash, P. R. Saulson, O. Sauter, R. L. Savage, A. Sawadsky, P. Schale, R. Schilling, J. Schmidt, P. Schmidt, R. Schnabel, R. M. S. Schofield, A. Schönbeck, E. Schreiber, D. Schuette, B. F. Schutz, J. Scott, S. M. Scott, D. Sellers, A. S. Sengupta, D. Sentenac, V. Sequino, A. Sergeev, G. Serna, Y. Setyawati, A. Sevigny, D. A. Shaddock, T. Shaffer, S. Shah, M. S. Shahriar, M. Shaltev, Z. Shao, B. Shapiro, P. Shawhan, A. Sheperd, D. H. Shoemaker, D. M. Shoemaker, K. Siellez, X. Siemens, D. Sigg, A. D. Silva, D. Simakov, A. Singer, L. P. Singer, A. Singh, R. Singh, A. Singhal, A. M. Sintes, B. J. J. Slagmolen, J. R. Smith, M. R. Smith, N. D. Smith, R. J. E. Smith, E. J. Son, B. Sorazu, F. Sorrentino, T. Souradeep, A. K. Srivastava, A. Staley, M. Steinke, J. Steinlechner, S. Steinlechner, D. Steinmeyer, B. C. Stephens, S. P. Stevenson, R. Stone, K. A. Strain, N. Straniero, G. Stratta, N. A. Strauss, S. Strigin, R. Sturani, A. L. Stuver, T. Z. Summerscales, L. Sun, P. J. Sutton, B. L. Swinkels, M. J. Szczepańczyk, M. Tacca, D. Talukder, D. B. Tanner, M. Tápai, S. P. Tarabrin, A. Taracchini, R. Taylor, T. Theeg, M. P. Thirugnanasambandam, E. G. Thomas, M. Thomas, P. Thomas, K. A. Thorne, K. S. Thorne, E. Thrane, S. Tiwari, V. Tiwari, K. V. Tokmakov, C. Tomlinson, M. Tonelli, C. V. Torres, C. I. Torrie, D. Töyrä, F. Travasso, G. Traylor, D. Trifirò, M. C. Tringali, L. Trozzo, M. Tse, M. Turconi, D. Tuyenbayev, D. Ugolini, C. S. Unnikrishnan, A. L. Urban, S. A. Usman, H. Vahlbruch, G. Vajente, G. Valdes, M. Vallisneri, N. van Bakel, M. van Beuzekom, J. F. J. van den Brand, C. Van Den Broeck, D. C. Vander-Hyde, L. van der Schaaf, J. V. van Heijningen, A. A. van Veggel, M. Vardaro, S. Vass, M. Vasúth, R. Vaulin, A. Vecchio, G. Vedovato, J. Veitch, P. J. Veitch,

K. Venkateswara, D. Verkindt, F. Vetrano, A. Viceré, S. Vinciguerra, D. J. Vine, J.-Y. Vinet, S. Vitale, T. Vo, H. Vocca, C. Vorvick, D. Voss, W. D. Vousden, S. P. Vyatchanin, A. R. Wade, L. E. Wade, M. Wade, S. J. Waldman, M. Walker, L. Wallace, S. Walsh, G. Wang, H. Wang, M. Wang, X. Wang, Y. Wang, H. Ward, R. L. Ward, J. Warner, M. Was, B. Weaver, L.-W. Wei, M. Weinert, A. J. Weinstein, R. Weiss, T. Welborn, L. Wen, P. Weßels, T. Westphal, K. Wette, J. T. Whelan, S. E. Whitcomb, D. J. White, B. F. Whiting, K. Wiesner, C. Wilkinson, P. A. Willems, L. Williams, R. D. Williams, A. R. Williamson, J. L. Willis, B. Willke, M. H. Wimmer, L. Winkelmann, W. Winkler, C. C. Wipf, A. G. Wiseman, H. Wittel, G. Woan, J. Worden, J. L. Wright, G. Wu, J. Yablon, I. Yakushin, W. Yam, H. Yamamoto, C. C. Yancey, M. J. Yap, H. Yu, M. Yvert, A. Zadrożny, L. Zangrando, M. Zanolin, J.-P. Zendri, M. Zevin, F. Zhang, L. Zhang, M. Zhang, Y. Zhang, C. Zhao, M. Zhou, Z. Zhou, X. J. Zhu, M. E. Zucker, S. E. Zuraw, & J. Zweizig. 2016, Phys. Rev. Lett., 116, 061102

Alexander, T. 2005, Physics Reports, 419, 65

Angélil, R. & P. Saha. 2010, ApJ, 711, 157

—. 2011, ApJ, 734, L19

Antonini, F. & H. B. Perets. 2012, ApJ, 757, 27

Astropy Collaboration, T. P. Robitaille, E. J. Tollerud, P. Greenfield, M. Droettboom, E. Bray, T. Aldcroft, M. Davis, A. Ginsburg, A. M. Price-Whelan, W. E. Kerzendorf, A. Conley, N. Crighton, K. Barbary, D. Muna, H. Ferguson, F. Grollier, M. M. Parikh, P. H. Nair, H. M. Unther, C. Deil, J. Woillez, S. Conseil, R. Kramer, J. E. H. Turner, L. Singer, R. Fox, B. A. Weaver, V. Zabalza, Z. I. Edwards, K. Azalee Bostroem, D. J. Burke, A. R. Casey, S. M. Crawford, N. Dencheva, J. Ely, T. Jenness, K. Labrie, P. L. Lim, F. Pierfederici, A. Pontzen, A. Ptak, B. Refsdal, M. Servillat, & O. Streicher. 2013, A&A, 558, A33

Bartko, H., F. Martins, S. Trippe, T. K. Fritz, R. Genzel, T. Ott, F. Eisenhauer, S. Gillessen, T. Paumard, T. Alexander, K. Dodds-Eden, O. Gerhard, Y. Levin, L. Mascetti, S. Nayakshin, H. B. Perets, G. Perrin, O. Pfuhl, M. J. Reid, D. Rouan, M. Zilka, & A. Sternberg. 2009, The Astrophysical Journal, 708, 834

Bobylev, V. V. 2008, Astronomy Letters, 34, 686

Boehle, A., A. M. Ghez, R. Schödel, L. Meyer, S. Yelda, S. Albers, G. D. Martinez, E. E. Becklin, T. Do, J. R. Lu, K. Matthews, M. R. Morris, B. Sitarski, & G. Witzel. 2016, ApJ, 830, 17

Bohlin, R. C., S. Mészáros, S. W. Fleming, K. D. Gordon, A. M. Koekemoer, & J. Kovács. 2017, AJ, 153, 234

Borka, D., P. Jovanović, V. Borka Jovanović, & A. F. Zakharov. 2013, , 11, 50

Brown, W. R. 2015, Annual Review of Astronomy and Astrophysics, 53, 15

Chen, X. & P. Amaro-Seoane. 2014, The Astrophysical Journal, 786, L14

Chu, D. S., T. Do, A. Hees, A. Ghez, S. Naoz, G. Witzel, S. Sakai, S. Chappell, A. K. Gautam, J. R. Lu, & K. Matthews. 2018, ApJ, 854, 12

Ciurlo, A., T. Paumard, D. Rouan, & Y. Clénet. 2019, Astronomy and Astrophysics, 621, A65

Ciurlo, A., R. D. Campbell, M. R. Morris, T. Do, A. M. Ghez, A. Hees, B. N. Sitarski, K. Kosmo O'Neil, D. S. Chu, G. D. Martinez, S. Naoz, & A. P. Stephan. 2020, Nature, 577, 337

de Mink, S. E., N. Langer, R. G. Izzard, H. Sana, & A. de Koter. 2013, ApJ, 764, 166

Diolaiti, E., O. Bendinelli, D. Bonaccini, L. Close, D. Currie, & G. Parmeggiani. 2000, Astronomical Data Analysis Software and Systems IX, 216, 623

Do, T., A. M. Ghez, M. R. Morris, J. R. Lu, K. Matthews, S. Yelda, & J. Larkin. 2009, The Astrophysical Journal, 703, 1323

Do, T., W. Kerzendorf, Q. Konopacky, J. M. Marcinik, A. Ghez, J. R. Lu, & M. R. Morris. 2018, ApJ, 855, L5

Do, T., W. Kerzendorf, N. Winsor, M. Støstad, M. R. Morris, J. R. Lu, & A. M. Ghez. 2015, ApJ, 809, 143

Do, T., J. R. Lu, A. M. Ghez, M. R. Morris, S. Yelda, G. D. Martinez, S. A. Wright, & K. Matthews. 2013, The Astrophysical Journal, 764, 154

Do, T., A. Hees, A. Ghez, G. D. Martinez, D. S. Chu, S. Jia, S. Sakai, J. R. Lu, A. K. Gautam, K. K. O'Neil, E. E. Becklin, M. R. Morris, K. Matthews, S. Nishiyama, R. Campbell, S. Chappell, Z. Chen, A. Ciurlo, A. Dehghanfar, E. Gallego-Cano, W. E. Kerzendorf, J. E. Lyke, S. Naoz, H. Saida, R. Schödel, M. Takahashi, Y. Takamori, G. Witzel, & P. Wizinowich. 2019, Science, https://science.sciencemag.org/content/early/2019/07/24/science.aav8137.full.pdf

Duchêne, G. & A. Kraus. 2013, Annual Review of Astronomy and Astrophysics, 51, 269

Dworetsky, M. M. 1983, MNRAS, 203, 917

Eisenhauer, F., R. Genzel, T. Alexander, R. Abuter, T. Paumard, T. Ott, A. Gilbert, S. Gillessen, M. Horrobin, S. Trippe, H. Bonnet, C. Dumas, N. Hubin, A. Kaufer, M. Kissler Patig, G. Monnet, S. Strobele, T. Szeifert, A. Eckart, R. Schödel, & S. Zucker. 2005, The Astrophysical Journal, 628, 246

Feldmeier-Krause, A., W. Kerzendorf, N. Neumayer, R. Schödel, F. Nogueras-Lara, T. Do, P. T. de Zeeuw, & H. Kuntschner. 2017, MNRAS, 464, 194

Feroz, F. & M. P. Hobson. 2008, Monthly Notices of the Royal Astronomical Society, 384, 449

Feroz, F., M. P. Hobson, & M. Bridges. 2009, MNRAS, 398, 1601

Feroz, F., M. P. Hobson, E. Cameron, & A. N. Pettitt. 2013, ArXiv e-prints, arXiv:1306.2144

Gautam, A. K., T. Do, A. M. Ghez, M. R. Morris, G. D. Martinez, J. Hosek, Matthew W., J. R. Lu, S. Sakai, G. Witzel, S. Jia, E. E. Becklin, & K. Matthews. 2019, ApJ, 871, 103

Ghez, A. M., S. Salim, S. D. Hornstein, A. Tanner, J. R. Lu, M. Morris, E. E. Becklin, & G. Duchêne. 2005, The Astrophysical Journal, 620, 744

Ghez, A. M., G. Duchêne, K. Matthews, S. D. Hornstein, A. Tanner, J. Larkin, M. Morris, E. E. Becklin, S. Salim, T. Kremenek, D. Thompson, B. T. Soifer, G. Neugebauer, & I. McLean. 2003, The Astrophysical Journal, 586, L127

Ghez, A. M., S. Salim, N. N. Weinberg, J. R. Lu, T. Do, J. K. Dunn, K. Matthews, M. Morris, S. Yelda, E. E. Becklin, T. Kremenek, M. Milosavljevic, & J. Naiman. 2008, ApJ, 1

Gillessen, S., F. Eisenhauer, T. K. Fritz, H. Bartko, K. Dodds-Eden, O. Pfuhl, T. Ott, & R. Genzel. 2009a, The Astrophysical Journal, 707, L114

Gillessen, S., F. Eisenhauer, S. Trippe, T. Alexander, R. Genzel, F. Martins, & T. Ott. 2009b, The Astrophysical Journal, 692, 1075

Gillessen, S., R. Genzel, T. K. Fritz, E. Quataert, C. Alig, A. Burkert, J. Cuadra, F. Eisenhauer, O. Pfuhl, K. Dodds-Eden, C. F. Gammie, & T. Ott. 2012, Nature, 481, 51

Gillessen, S., P. M. Plewa, F. Eisenhauer, R. Sari, I. Waisberg, M. Habibi, O. Pfuhl, E. George, J. Dexter, S. von Fellenberg, T. Ott, & R. Genzel. 2017, The Astrophysical Journal, 837, 30

Gontcharov, G. A. 2006, Astronomy Letters, 32, 759

Gravity Collaboration, R. Abuter, A. Amorim, N. Anugu, M. Bauböck, M. Benisty, J. P. Berger, N. Blind, H. Bonnet, W. Brandner, A. Buron, C. Collin, F. Chapron, Y. Clénet, V. Coudé Du Foresto, P. T. de Zeeuw, C. Deen, F. Delplancke-Ströbele, R. Dembet, J. Dexter, G. Duvert, A. Eckart, F. Eisenhauer, G. Finger, N. M. Förster Schreiber, P. Fédou, P. Garcia, R. Garcia Lopez, F. Gao, E. Gendron, R. Genzel, S. Gillessen, P. Gordo, M. Habibi, X. Haubois, M. Haug, F. Haußmann, T. Henning, S. Hippler, M. Horrobin, Z. Hubert, N. Hubin, A. Jimenez Rosales, L. Jochum, K. Jocou, A. Kaufer, S. Kellner, S. Kendrew, P. Kervella, Y. Kok, M. Kulas, S. Lacour, V. Lapeyrère, B. Lazareff, J. B. Le Bouquin, P. Léna, M. Lippa, R. Lenzen, A. Mérand, E. Müler, U. Neumann, T. Ott, L. Palanca, T. Paumard, L. Pasquini, K. Perraut, G. Perrin, O. Pfuhl, P. M. Plewa, S. Rabien, A. Ramírez, J. Ramos, C. Rau, G. Rodríguez-Coira, R. R. Rohloff, G. Rousset, J. Sanchez-Bermudez, S. Scheithauer, M. Schöller, N. Schuler, J. Spyromilio, O. Straub, C. Straubmeier, E. Sturm, L. J. Tacconi, K. R. W. Tristram, F. Vincent, S. von Fellenberg, I. Wank, I. Waisberg, F. Widmann, E. Wieprecht, M. Wiest, E. Wiezorrek, J. Woillez, S. Yazici, D. Ziegler, & G. Zins. 2018, A&A, 615, L15

Habibi, M., S. Gillessen, F. Martins, F. Eisenhauer, P. M. Plewa, O. Pfuhl, E. George, J. Dexter, I. Waisberg, T. Ott, S. von Fellenberg, M. Bauböck, A. Jimenez-Rosales, & R. Genzel. 2017, ApJ, 847, 120

Hees, A., A. Dehghanfar, T. Do, A. M. Ghez, G. D. Martinez, R. Campbell, & J. R. Lu. 2019, arXiv e-prints, arXiv:1906.03099

Hees, A., T. Do, A. M. Ghez, G. D. Martinez, S. Naoz, E. E. Becklin, A. Boehle, S. Chappell, D. Chu, A. Dehghanfar, K. Kosmo, J. R. Lu, K. Matthews, M. R. Morris, S. Sakai, R. Schödel, & G. Witzel. 2017, Phys. Rev. Lett., 118, 211101

Hees, A., A. M. Ghez, T. Do, J. R. Lu, M. R. Morris, E. E. Becklin, G. Witzel, A. Boehle, S. Chappell, Z. Chen, D. Chu, A. Ciurlo, A. Dehghanfar, E. Gallego-

Cano, A. Gautam, S. Jia, K. Kosmo, G. D. Martinez, K. Matthews, S. Naoz, S. Sakai, & R. Schödel. 2017, ArXiv e-prints, arXiv:1705.10792

Hilditch, R. W. 2001, An Introduction to Close Binary Stars, 392

Hills, J. G. 1988, Nature, 331, 687

Hoang, B.-M., S. Naoz, B. Kocsis, F. A. Rasio, & F. Dosopoulou. 2018, ApJ, 856, 140

Hopman, C. 2009, The Astrophysical Journal, 700, 1933

Hosek, J., M. W., J. R. Lu, C. Y. Lam, A. K. Gautam, K. E. Lockhart, D. Kim, & S. Jia. 2020a, arXiv e-prints, arXiv:2006.06691

—. 2020b, PyPopStar: Single-age, single-metallicity populations generator, ascl:2006.016

Huang, W., D. R. Gies, & M. V. McSwain. 2010, ApJ, 722, 605

Jia, S., J. R. Lu, S. Sakai, A. K. Gautam, T. Do, J. Hosek, M. W., M. Service, A. M. Ghez, E. Gallego-Cano, R. Schödel, A. Hees, M. R. Morris, E. Becklin, & K. Matthews. 2019, ApJ, 873, 9

Johannsen, T. 2016a, Classical and Quantum Gravity, 33, 113001

—. 2016b, Classical and Quantum Gravity, 33, 124001

Kerr, F. J. & D. Lynden-Bell. 1986, MNRAS, 221, 1023

Kerzendorf, W. & T. Do. 2015, starkit: First real release, Zenodo Source Code Library, doi:10.5281/zenodo.28016

Khalack, V. & F. LeBlanc. 2015, AJ, 150, 2

Kharchenko, N. V., R. D. Scholz, A. E. Piskunov, S. Röser, & E. Schilbach. 2007, Astronomische Nachrichten, 328, 889

Larkin, J., M. Barczys, A. Krabbe, S. Adkins, T. Aliado, P. Amico, G. Brims, R. Campbell, J. Canfield, T. Gasaway, A. Honey, C. Iserlohe, C. Johnson, E. Kress, D. LaFreniere, K. Magnone, N. Magnone, M. McElwain, J. Moon, A. Quirrenbach, G. Skulason, I. Song, M. Spencer, J. Weiss, & S. Wright. 2006, , 50, 362

Levin, Y. 2007, Monthly Notices of the Royal Astronomical Society, 374, 515

Li, G., I. Ginsburg, S. Naoz, & A. Loeb. 2017, ArXiv e-prints, arXiv:1708.08466

Lockhart, K. E., T. Do, J. E. Larkin, A. Boehle, R. D. Campbell, S. Chappell, D. Chu, A. Ciurlo, M. Cosens, M. P. Fitzgerald, A. Ghez, J. R. Lu, J. E. Lyke, E. Mieda, A. R. Rudy, A. Vayner, G. Walth, & S. A. Wright. 2019, AJ, 157, 75

Löckmann, U., H. Baumgardt, & P. Kroupa. 2008, The Astrophysical Journal, 683, L151

Lomb, N. R. 1976, , 39, 447

Lu, J. R., A. M. Ghez, S. D. Hornstein, M. R. Morris, E. E. Becklin, & K. Matthews. 2009, The Astrophysical Journal, 690, 1463

Lyke, J., T. Do, A. Boehle, R. Campbell, S. Chappell, M. Fitzgerald, T. Gasawy, C. Iserlohe, A. Krabbe, J. Larkin, K. Lockhard, J. Lu, E. Mieda, M. McElwain, M. Perrin, A. Rudy, B. Sitarski, A. Vayner, G. Walth, J. Weiss, T. Wizanski, & S. Wright. 2017, OSIRIS Toolbox: OH-Suppressing InfraRed Imaging Spectrograph pipeline, ascl:1710.021

Madigan, A.-M., O. Pfuhl, Y. Levin, S. Gillessen, R. Genzel, & H. B. Perets. 2014, The Astrophysical Journal, 784, 23

Martins, F., S. Gillessen, F. Eisenhauer, R. Genzel, T. Ott, & S. Trippe. 2008, The Astrophysical Journal, 672, L119

Martins, F., S. Trippe, T. Paumard, T. Ott, R. Genzel, G. Rauw, F. Eisenhauer, S. Gillessen, H. Maness, & R. Abuter. 2006, ApJ, 649, L103

Matthews, K. & B. T. Soifer. 1994, Experimental Astronomy, 3, 77

Merritt, D., A. Gualandris, & S. Mikkola. 2009, ApJ, 693, L35

Morris, M. 1993, The Astrophysical Journal, 408, 496

Naoz, S. 2016, ARA&A, 54, 441

Naoz, S., A. M. Ghez, A. Hees, T. Do, G. Witzel, & J. R. Lu. 2018, ApJ, 853, L24

Nishiyama, S., H. Saida, Y. Takamori, M. Takahashi, R. Schödel, F. Najarro, S. Hamano, M. Omiya, M. Tamura, M. Takahashi, H. Gorin, S. Nagatomo, & T. Nagata. 2018, PASJ, 70, 74

Ott, T., A. Eckart, & R. Genzel. 1999, The Astrophysical Journal, 523, 248

Paumard, T., R. Genzel, F. Martins, S. Nayakshin, A. M. Beloborodov, Y. Levin, S. Trippe, F. Eisenhauer, T. Ott, S. Gillessen, R. Abuter, J. Cuadra, T. Alexander, & A. Sternberg. 2006, The Astrophysical Journal, 643, 1011

Perets, H. B., A. Gualandris, G. Kupi, D. Merritt, & T. Alexander. 2009, ApJ, 702, 884

Perets, H. B., A. Gualandris, G. Kupi, D. Merritt, & T. Alexander. 2009, The Astrophysical Journal, 702, 884

Perets, H. B., C. Hopman, & T. Alexander. 2007, The Astrophysical Journal, 656, 709

Pfuhl, O., T. Alexander, S. Gillessen, F. Martins, R. Genzel, F. Eisenhauer, T. K. Fritz, & T. Ott. 2014, The Astrophysical Journal, 782, 101

Phifer, K., T. Do, L. Meyer, A. M. Ghez, G. Witzel, S. Yelda, A. Boehle, J. R. Lu, M. R. Morris, E. E. Becklin, & K. Matthews. 2013, The Astrophysical Journal Letters, 773, L13

Psaltis, D., N. Wex, & M. Kramer. 2016, ApJ, 818, 121

Rafelski, M., A. M. Ghez, S. D. Hornstein, J. R. Lu, & M. Morris. 2007, The Astrophysical Journal, 659, 1241

Raghavan, D., H. A. McAlister, T. J. Henry, D. W. Latham, G. W. Marcy, B. D. Mason, D. R. Gies, R. J. White, & T. A. ten Brummelaar. 2010, The Astrophysical Journal Supplement Series, 190, 1

Rubilar, G. F. & A. Eckart. 2001, A&A, 374, 95

Sakai, S., J. R. Lu, A. Ghez, S. Jia, T. Do, G. Witzel, A. K. Gautam, A. Hees, E. Becklin, K. Matthews, & J. Hosek, M. W. 2019, ApJ, 873, 65

Sana, H., S. E. de Mink, A. de Koter, N. Langer, C. J. Evans, M. Gieles, E. Gosset, R. G. Izzard, J.-B. Le Bouquin, & F. R. N. Schneider. 2012, Science, 337, 444

Scargle, J. D. 1982, The Astrophysical Journal, 263, 835

Schödel, R., F. Najarro, K. Muzic, & A. Eckart. 2010, A&A, 511, A18

Stellingwerf, R. F. 1972, A&A, 21, 91

Stephan, A. P., S. Naoz, A. M. Ghez, G. Witzel, B. N. Sitarski, T. Do, & B. Kocsis. 2016, Monthly Notices of the Royal Astronomical Society, 460, 3494

Stephan, A. P., S. Naoz, A. M. Ghez, M. R. Morris, A. Ciurlo, T. Do, K. Breivik, S. Coughlin, & C. L. Rodriguez. 2019, ApJ, 878, 58

van Dam, M. A., A. H. Bouchez, D. Le Mignant, E. M. Johansson, P. L. Wizinowich, R. y. D. Campbell, J. C. Y. Chin, S. K. Hartman, R. E. Lafon, J. Stomski, Paul J., & D. M. Summers. 2006, PASP, 118, 310

Vanderplas, J., B. Naul, A. Willmer, P. Williams, & B. M. Morris. 2016, gatspy: Version 0.3 Feature Release, doi:10.5281/zenodo.47887

VanderPlas, J. T. 2018, ApJS, 236, 16

VanderPlas, J. T. & Ž. Ivezić. 2015, ApJ, 812, 18

Will, C. M. 2008, ApJ, 674, L25

Witzel, G., A. M. Ghez, M. R. Morris, B. N. Sitarski, A. Boehle, S. Naoz, R. Campbell, E. E. Becklin, G. Canalizo, S. Chappell, T. Do, J. R. Lu, K. Matthews, L. Meyer, A. Stockton, P. Wizinowich, & S. Yelda. 2014, ApJ, 796, L8

Witzel, G., B. N. Sitarski, A. M. Ghez, M. R. Morris, A. Hees, T. Do, J. R. Lu, S. Naoz, A. Boehle, G. Martinez, S. Chappell, R. Schödel, L. Meyer, S. Yelda, E. E. Becklin, & K. Matthews. 2017, The Astrophysical Journal, 847, 80

Wizinowich, P. L., D. Le Mignant, A. H. Bouchez, R. D. Campbell, J. C. Y. Chin, A. R. Contos, M. A. van Dam, S. K. Hartman, E. M. Johansson, R. E. Lafon, H. Lewis, P. J. Stomski, D. M. Summers, C. G. Brown, P. M. Danforth, C. E. Max, & D. M. Pennington. 2006, PASP, 118, 297

Yelda, S., A. M. Ghez, J. R. Lu, T. Do, L. Meyer, M. R. Morris, & K. Matthews. 2014, The Astrophysical Journal, 783, 131

Yu, Q. & S. Tremaine. 2003, ApJ, 599, 1129

Zakharov, A. F., P. Jovanović, D. Borka, & V. Borka Jovanović. 2016, , 05, 045

Zucker, S., T. Alexander, S. Gillessen, F. Eisenhauer, & R. Genzel. 2006, ApJ, 639, L21